INFORMATION TO USERS

This manuscript has been reproduced from the microfilm master. UMI films the text directly from the original or copy submitted. Thus, some thesis and dissertation copies are in typewriter face, while others may be from any type of computer printer.

The quality of this reproduction is dependent upon the quality of the copy submitted. Broken or indistinct print, colored or poor quality illustrations and photographs, print bleedthrough, substandard margins, and improper alignment can adversely affect reproduction.

In the unlikely event that the author did not send UMI a complete manuscript and there are missing pages, these will be noted. Also, if unauthorized copyright material had to be removed, a note will indicate the deletion.

Oversize materials (e.g., maps, drawings, charts) are reproduced by sectioning the original, beginning at the upper left-hand corner and continuing from left to right in equal sections with small overlaps. Each original is also photographed in one exposure and is included in reduced form at the back of the book.

Photographs included in the original manuscript have been reproduced xerographically in this copy. Higher quality 6" x 9" black and white photographic prints are available for any photographs or illustrations appearing in this copy for an additional charge. Contact UMI directly to order.

UMI

A Bell & Howell Information Company
300 North Zeeb Road, Ann Arbor MI 48106-1346 USA
313/761-4700 800/521-0600

RESONANT X-RAY REFLECTIVITY STUDIES OF NANOMETRIC SCALE STRUCTURES

by

JIANMING BAI

A dissertation submitted to the Graduate Faculty in Physics in partial fulfillment of the requirements for the degree of Doctor of Philosophy, The City University of New York

1996

This manuscript has been read and accepted for the Graduate Faculty in Physics in satisfaction of the dissertation requirement for the degree of Doctor of Philosophy.

7/30/96
Date

Micha Tomkiewicz
Chair of Examining Committee

8/5/96
Date

Joseph B. Krieger
Executive Officer

Pedro A. Montano

Fred H. Pollak

Herman Z. Cummins

Mark Beno

Supervisory Committee

THE CITY UNIVERSITY OF NEW YORK

Abstract

RESONANT X-RAY REFLECTIVITY STUDIES OF NANOMETRIC SCALE STRUCTURES

by

Jianming Bai

Adviser: Professor Pedro A. Montano

We have developed a new method, the resonant x-ray reflectivity (RXR) as a non-destructive structural probe for the study of nanometric scale structures.

For a Ni/Fe alloy thin film, the RXR method is used for determining the composition profile which is impossible with the regular x-ray reflectivity technique. The RXR method is also used to study the interface structures of two Cr/Fe superlattices deposited on MgO substrates with different crystal orientations. We were able to obtain unique and accurate quantitative results of the embedded interfacial roughness for these superlattices.

Also included in this dissertation is an extensive discussion of the theories and experimentation of x-ray reflectivity with synchrotron radiation. Different interface models and calculation methods are compared and, Particularly, two calculation formalisms, the form factor method and the line-segment approach are used in the development of the resonant reflectivity technique.

Acknowledgments

First of all, I would like to express my deep gratitude to my thesis advisor, Prof. Pedro Montano. This thesis project would be impossible without his constant encouragement and sound advice.

The research project was conducted at National Synchrotron Light Source of Brookhaven National Laboratory with supports of Materials Science Division of Argonne National laboratory. I am indebted to Dr. Peter Lee, Dr. Kegang Huang, Dr. Mohan Ramanathan and Dr. Arun Bommanavar. Their valuable assistant and helpful discussion in the process of my experimental work at beam line X6B and X18B of NSLS are greatly appreciated. Special thanks are extended to Mark Engbretson for his wonderful data acquisition software EXASCAN and his help on various computer related problems.

I am very grateful to Prof. Micha Tomkiewicz for introducing me into the field of experimental physics and for his helpful advice in the early stage of Ni/Fe thin film studies. I would like to acknowledge with my gratitude Dr. Eric Fullerton for providing the Cr/Fe superlattice samples and the helpful discussion about the structure and properties of these samples.

I would like to express my sincerest thanks to Professor Fred Pollak of Brooklyn College, Professor Herman Cummins of City College and Dr. Mark Beno of Argonne National Laboratory for serving the Supervisory Committee and their careful reading of this manuscript and valuable advice.

I also wish to thank Department of Physics of Brooklyn College and Research Foundation of CUNY for providing me with the full financial support.

No words can express my gratitude to my family, my wife Mei, and my daughter Nina. Their love and confidence in me are the driving force for me to go through the course of this thesis project.

TABLE OF CONTENTS

List of Tables

List of Figures

Figure

CHAPTER 1 INTRODUCTION

The development of thin film and multilayer structures in nanometric scale has been very important in recent years due to the improvement of different deposition techniques. In principle, any technique in which the material is produced by means of "atom by atom" construction can be used to produce thin film and multilayers. Such processes include: chemical vapor deposition[1], electrochemical deposition[2] and physical vapor deposition[3]. The physical vapor deposition technologies used in synthesizing layered structures are based on the evaporation or sputtering of a target in a vacuum or in noble gas discharges sustained under low pressures. Evaporation is a process of thermal vaporizing of the target in which the heating is carried out at a low pressure. Sputtering is a process whereby material is ejected from the surface of a target material as a result of momentum and energy transfer in a bombardment of the surface by energetic particles[4]. A breakthrough in sputtering was the invention of the magnetron sputtering source[5]. For conventional diodes, it is very difficult to isolate the deposition surface from plasma generated species other than the depositing species, thus results in ion bombardment mixing of the constituents that can extend several nanometers into the sample. Therefore, it is difficult to synthesize a thin film or multilayer structure with compositionally abrupt interfaces using conventional sputtering sources. Magnetron sources have a magnet structure behind the sputter source plate

produced in the noble gas sputter ionization. These electrons are trapped at the target surface thereby trapping the plasma, and increasing the plasma density at the target surface. It is this trapping mechanism that allows the isolation of the sputtering plasma from the deposition surface, it increases the deposition rates by a factor of ten larger than conventional diodes. These advantages make it possible to make high quality multilayers. Eric E. Fullerton et al [6] have reported achievement of epitaxy in the sputtering of Fe/Cr superlattices onto MgO single-crystalline substrates with a dc magnetron sputtering source.

Nanometric scale structures are studied in numerous fields of science for their optical, magnetic, electrical, or superconducting properties, as well as for a wide range of technological applications .

For example, the permalloy (Ni/Fe) , in an integrated thin film form, is used to make the soft magnet core in the coil of the magnet recording head. The writing of the information in magnetic recording is performed with the help of the recording head's magnetic field. The local magnetization of the media is changed according to the information pattern. The reading process is based on the signal induced by the magnetized bits at the head's coil. For faster memories a high speed recording head is essential. The head should have a high magnetization, low coercivity, high permeability and zero magnetostriction. Permalloy is the traditional soft magnetic material for a recording head because of its unique magnetic properties, although several new material have been proposed lately.[7]

Metallic multilayers have been successfully used as dispersion elements for soft x-ray applications[8] They were used to design normal incidence optics for x-ray microscopes and telescopes with substantially higher resolution than is possible with grazing incidence optics.[9] Multilayers of a sequence of ferromagnetic-nonmagnetic layers are extensively used in neutron scattering technology, as monochromators, polarizers and reflectors.[7] The interest in application of magnetic multilayers increased suddenly in the late 80's when the first reports on the exceptional properties of these artificially structured materials emerged, such as perpendicular anisotropy[10], giant magnetoresistance[11], magneto-optical activity[12] . The interest is motivated by the prospective use of magnetic multilayers as magnetic/magnetooptic recording materials and sensors of magnetic fields. The giant magnetoresistance (GMR) effect is a large percentage change of the electrical resistivity in the presence of a magnetic field. It has been observed in some multilayers composed of ferromagnet (Fe, Co, Ni, permalloy) and nonmagnetic metal (Al, Cu, Ag, Au, Cr, Pd, Ta, Pt) layers. As an example, a GMR value of 150% was reported for the $[Fe(14A)/Cr(8A)]_{50}$ (100) superlattice at 4.2 K. [6] Due to This effect, the magnetic multilayers with GMR become a good candidate for the next generation recording heads. The multilayer head offers a much higher signal-to-noise ratio and better overall performance for high density recording.[13]

A detail structural characterization of thin films and multilayers is essential for further understanding of the physical and chemical processes

such as corrosion, porosity, aging, annealing, crystallinity, strain and interdiffusion, as well as some magnetic (antiferromagnetic (AF) coupling, GMR effect) and mechanical (acoustic surface and film excitations) properties, which are characteristic of nanometric scale structures. Some of the pertinent structural questions to be answered are: Is the substrate smooth or rough ? Is the substrate clean or dirty? Is the top layer contaminated, oxidized or in any other way different from embedded layers? What is the composition and structure of the layers? Is the structure amorphous, polycrystalline or single-crystal? Are the interfaces abrupt or graded ? Abrupt interfaces are defined as interfaces where the compositional change from material A to material B occurs over one atomic distance normal to the surface. Distinguishing between rough abrupt interfaces and graded interface (due to interdiffusion or composition mix during the sputtering processes) might be difficult. Does the deposition of material A onto material B or the substrate differ from the deposition of B onto A or the substrate during synthesis? A technique that provides depth composition profile is the most appropriated to characterize thin film and multilayer structures.

Many techniques are used for the analysis of compositional structures of thin films, such as Rutherford backscattering spectroscopy (RBS), Auger electron spectroscopy (AES), x-ray photoelectron spectroscopy (XPS), x-ray fluorescence (XRF), etc.. RBS is a non-destructive and quantitative method for compositional depth analysis, especially suitable for probing heavy impurities in light background materials. However, the

characterization of multilayers or alloy thin films composed of elements of similar atomic numbers (e.g. Ni/Fe, Cr/Fe) using RBS will be difficult, if not impossible, due to the overlap of the backscattering energies. Because of the limited escape depth of Auger electrons, AES and XPS must be used in conjunction with sputter-etching processes and therefore are destructive methods for depth analysis. XRF energy spectrum analysis is a widely applied technique for determination of elemental composition. In recent years a grazing incidence geometry for XRF (GIXF) has been used by many groups in compositional profiling of layered structures. [14,15,16,17,18] Since the penetration depth of X-ray changes from a few nm to a few μm with changes of the incident angle around the critical angle of total reflection, the GIXF scan gives information about the depth concentration profile of the fluorescent probes. However, since the change in penetration depth takes place in a very narrow angular range, in practice the applicability of this effect for depth profiling is limited. If the Bragg peak intensity of the multilayer sample is comparable to that of incident beam, a standing wave condition can be setup. In that case the shape of the GIXF intensity near a Bragg peak is rather sensitive to a change in composition, thereby providing compositional information of the embedded layers.

There are other techniques used in surface analysis that provide information other than the composition profile. Morphology of thin films is studied by transmission electron microscopy (TEM) and scanning electron microscopy (SEM). Surface x-ray diffraction (XRD) and high-energy electron diffraction (HEED) are used to determine orientations in the plane

of the film and their azimuthal location. Surface extended x-ray absorption fine-structure (EXAFS) measurements, such as obtained from the energy spectrum of the fluorescence excited by the x-ray of grazing incidence, gives local information about the atomic coordination and inter atomic distances.

Among all these analytical techniques, however, the potential of using x-ray reflectivity, or more specifically, resonant reflectivity, as a non-destructive method for composition depth profiling, has not been explored. It is the object of this thesis to develop this new tool in probing the composition depth profile of nanometric scale structures.

It is well known that the refractive index of a material in the x-ray wavelength region is slightly less than one. For sufficiently low angles of incidence, an x-ray beam can be specularly reflected from the surface and embedded interfaces of a thin film. The reflected beams interfere constructively and destructively, and this interference gives rise to a series of intensity fringes. Many important structural information such as sub-layer thickness, effective electron density and interfacial roughness can be obtained from these intensity curves. The x-ray reflectivity measurement have been used to study the nanometric scale structures of many different materials.

Although Compton demonstrated the phenomena of small-angle x-ray specular reflectivity in 1922,[19] the first serious attempt to use the technique to characterize material surface is Parratt's measurements on a copper surface in 1954.[20] However, his work was seriously limited by both the

low brilliance of the x-ray beams that were available at that time as well as by the difficulty in obtaining a sufficiently smooth surface. With the developments of thin film synthesis techniques and using conventional or rotating anode x-ray sources, reflectivity measurements were carried out on a broad range of surfaces. Examples include studies of mercury and liquid-metal surfaces,[21] of both coated and uncoated solid substrates, [22] of surface roughness and oxide layers of sputtered polycrystalline films,[23] and of sputter-deposited spin-valve layered structures.[24] With the fast development of Synchrotron radiation facilities around the world, the x-rays produced by synchrotron radiation are playing a more important role in the studies of material structures. The high intensity and the energy tunability over a broad spectral range of synchrotron radiation greatly enhanced the application of x-ray specular reflectivity as a probe of interface and surface structures. It increases the range of accessible scattering angles and allows the use of a variety of energies. Some recent examples are: studies of silicon coated by organic monolayers (alkylsiloxanes),[25] of $Si_{1-x}Ge_x/Si$ heterostructures, [26] of the surface structure of diblock copolymer films,[27] and of $CoSi_2$ layers in Si produced by ion-beam synthesis. [28]

None of the reflectivity measurements in the above mentioned studies are used in compositional profile determination. Since the reflected x-ray intensity is elastically scattered by the electrons in the sample, the x-ray reflectivity is not directly related to the atomic structures and therefore not an element sensitive technique. It is sensitive only to the electron density and the linear absorption of the materials. The electron density and linear

absorption are proportional to the atomic density and the atomic number. For a multi- elemental structure, if the composition profile is given, the electron density and absorption distribution and thereby the reflectivity can be calculated. Unfortunately, the converse of this statement is not necessarily true. The inverse problem cannot usually be uniquely solved owing to the limited range of scattering data and the nonlinear nature of the inverse transformation, and more importantly, the lack of phase information lost in the reflected intensity measurements (This is the same as the "phase problem" in crystallography). Therefore, even though some other approaches have been suggested,[29] a least-squares refinement analysis is almost the only practical way to determine the structural parameters. For conventional single energy reflectivity measurements, the ambiguity in the interpretation of the data curve is twofold. First, a single reflectivity data curve may correspond to different density profiles.[30] Second, for a structure of more than two components, the composition profile can not be determined uniquely from the given density profile (In principle, the composition profile of a two-component system can be defined if the electron density and the linear absorption are taken as independent parameters in the least squares process. However, sometimes the linear absorption, as a fitting parameter, is not as sensitive as the electron density (e.g. when the x-ray energy is lower than the absorption edges of both elements), therefore the composition profile thereby derived is usually not reliable.). So, generally speaking, the composition profile can not be uniquely determined from a single energy reflectivity measurement.

In this thesis, we will demonstrate that with measurements of x-ray reflectivity at right selected energies (we call it resonant x-ray reflectivity, RXR), one can determine the composition profile of the nanometric scale structures. This non-destructive technique has a spatial resolution of a few angstroms and is specially useful in structural studies of magnetic materials composed of elements with similar atomic number.

It is well known that the effective electron density ρ_e and the linear absorption μ are strong energy dependent variables near the absorption edges of the elements. The dispersion behavior is related to the specific atomic structure. The ρ_e and μ contrast between the chemical components in the layered structures varies as the energy of the incident x-ray changes. The reflectivity measured at selected energies (below and above, close and away from the respective absorption edge of the constitutional elements) then shows different features and gives information about the compositional structure of the samples under study.

It is interesting to compare RXR with the "anomalous scattering" technique used in crystallography. [31] To obtain the phase information from the diffraction pattern of a crystal structure, an isomorphous derivative of the crystal is often introduced. The derivative is prepared by inclusion of an extra atom, preferably a heavy atom such as platinum or mercury, into the native crystal. Comparison of the two diffraction patterns gives the needed phase information. The same information can, however, be obtained by varying the photon energy of the x-ray beam. By tuning the beam across the absorption edge of the heavy atom, an effect similar to making an

isomorphous derivatives can be obtained. Above the edge, the atom absorbs and appears not to be in the structure and below it scatters x-rays into the diffraction pattern instead of absorbing and is thus "in" the structure. This technique is called " anomalous scattering". The similarity between RXR and anomalous scattering is obvious. The difference between the two techniques is: instead of scattered by individual atoms, the specular reflectivity intensity is scattered by the discontinuities at interfaces of the layered structures. The optical contrast between the two sides of the interfaces is the main factor affecting the line shape of the reflectivity curves. Tuning the x-ray energy across the absorption edge of a layer will not make that layer disappear but more visible since the contrast in the linear absorption is enhanced. Further more, by tuning the x-ray energy close and away from the edges will also change (or even inverse) the contrast of the effective electron densities (or the atomic scattering factors) and thus change the reflectivity curves. All these changes are related to the composition profile of the layered structures and consequently, make RXR an elemental sensitive technique.

The plan of the thesis is as follows: In chapter 2, we shall discuss the theoretical background and calculation formalism for x-ray reflectivity analysis. In chapter 3, we present the experimental setup and procedures for the x-ray reflectivity measurements using synchrotron radiation . Chapter 4 and 5 will be devoted to two typical examples of the RXR studies: studies on a Ni/Fe alloy thin film and the Fe/Cr superlattices, respectively. Chapter 6 will be the conclusion of this thesis.

CHAPTER 2 THEORY

2.1 Atomic Scattering Factor

The elastic scattering of x-rays from an atom is described in terms of the atomic scattering factor, defined as the ratio of the radiation amplitude scattered by the atom to that by a free electron, in the form[32]

$$f = f_o + f' + if'' \tag{2.1}$$

Where f_o is the atomic form factor calculated assuming the x-ray energy is large compared to the binding energy of all of the electrons in the atom and in the nonrelativistic approximation is given by:

$$f_o(\mathbf{s}) = \int \psi_f^*(\mathbf{r}) \exp(i\mathbf{s}\cdot\mathbf{r}) \psi_i(\mathbf{r}) dV \tag{2.2}$$

ψ is the total wave function of the atom and i and f refer to the initial and final states. For elastic scattering they are the same. The vector s bisects the angle 180-2θ. 2θ is the angle between the incident and scattered wave vectors. The magnitude of s is $4\pi(\sin\theta)/\lambda$, where λ is the wavelength of the incident radiation and θ the Bragg angle. In general, f_o is a function of θ. In x-ray reflectivity measurements, however, s is usually close to zero and Eq. (2.2) can be simplified approximately:

$$f_o(\mathbf{s}) = \int \psi_f^*(\mathbf{r}) \psi_i(\mathbf{r}) dV \approx Z \tag{2.3}$$

where Z is the atomic number of the atom.

In Eq. (2.1), f' and f'' are the real and imaginary part of the anomalous dispersion terms which account for the absorption of x-ray by electrons bound in an atom. The anomalous scattering effect is of interest

for applications such as absorption and scattering experiments and phase determination of crystal structures, and is very important for RXR measurements. The f' term represents in-phase scattering and the f'' term represents scattering shifted by 90° in phase. As for many types of dispersion phenomena f' and f'' are linked by the Kramer-Kronig relation,

$$f'(\omega) = \sum_i \int_0^\infty \frac{\omega'^2 (dg/d\omega')_i d\omega'}{\omega^2 - \omega'^2}$$
$$f''(\omega) = \tfrac{1}{2}\pi\omega \sum_i (dg/d\omega)_i \qquad (2.4)$$

where $(dg/d\omega)_i$ is the oscillator density for oscillators of type i and the sum runs over all absorption edges. The oscillator density is related to the atomic absorption coefficient for the i-th oscillator $\mu(\omega)_i$ by

$$(dg/d\omega)_i = \frac{mc}{2\pi^2 e^2}\mu(\omega)_i \qquad (2.5)$$

Close to an absorption edge f' and f'' vary rapidly with wavelength. There is a sharp jump in f'' from below to above the edge while f' dips to a large negative value through the edge.

The anomalous scattering factors can be calculated using the Cromer-Liberman method.[33] A FORTRAN program based on this method is used to calculate f' and f'' in this thesis.[34] Fig. 2.1 shows the calculated curves of f' and f'' for Ni and Fe around their K-edges. The anomalous scattering factors can also be obtained experimentally, for example, by measuring a set of Bragg reflections from a crystal of known structure that contains a suitable heavy atom.[35]

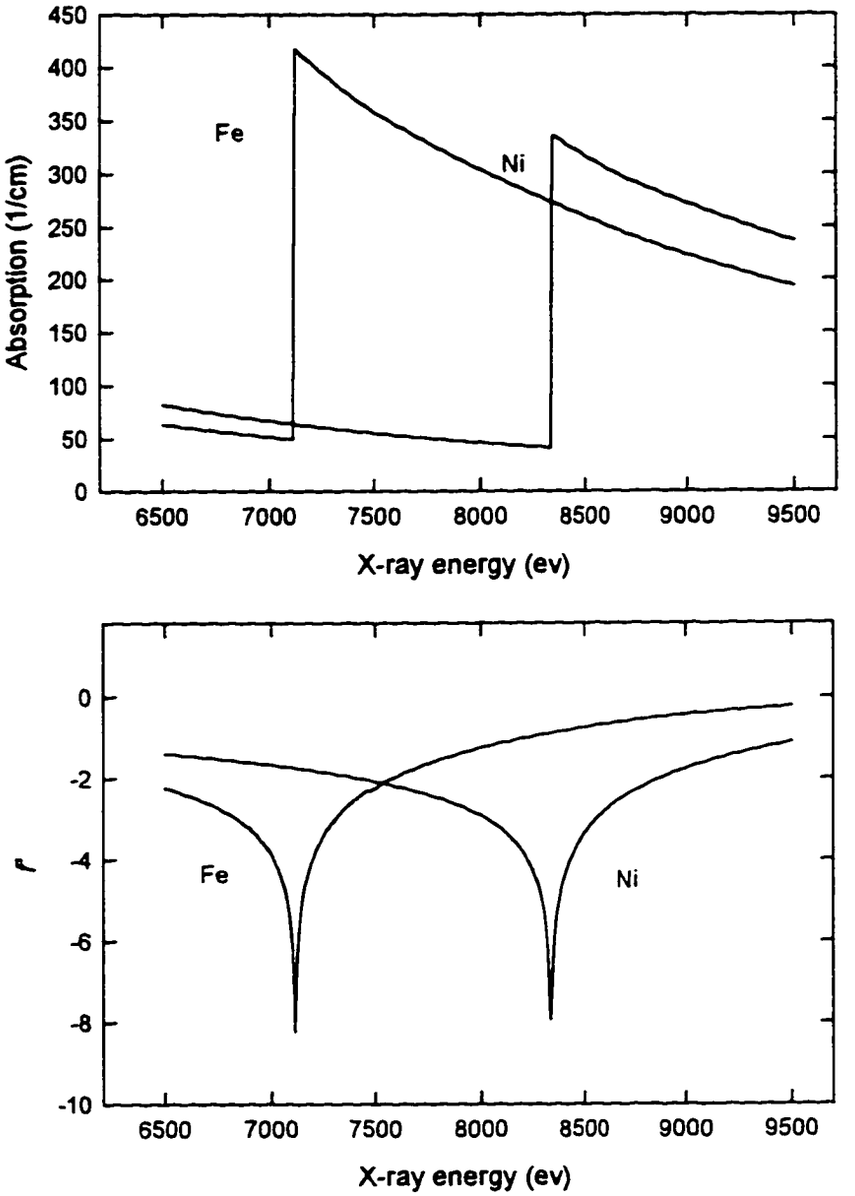

Fig. 2.1 Calculated linear absorption and the anomalous scattering factor for Ni and Fe. The K-edge of Ni is at 8333 eV and Fe is at 7112 eV.

Even though the wave length λ is comparable to atomic dimensions, specular reflectivity of x-ray can be described by the Fresnel theory of classical optics.[20,25] For each material, a complex dielectric constant $\varepsilon_i = \varepsilon_i' + i\varepsilon_i''$ can be defined:[36]

$$\begin{aligned}\varepsilon_i(\omega) &= 1 - \frac{4\pi e^2}{m\omega^2} N_i f_i^* \\ &= 1 - \frac{r_e \lambda^2 N_a}{\pi} \frac{\rho_{Mi}}{A_i} (Z_i + f_i' - i f_i'')\end{aligned} \tag{2.6}$$

Where N_i is the number density of atoms, λ the x-ray wavelength, r_e the classical electron radius, N_a the Avogadro constant, ρ_{Mi} the mass density of the material and A_i the atomic mass. f_i^* is complex conjugate of f_i, which is defined by Eq. (2.1) with the subscript referring to element i. Note that in this convention both f_i and ε_i have positive imaginary parts and the incident wave should be in the form of $E_0 e^{i(\mathbf{k}\cdot\mathbf{r}-\omega t)}$.[37] Substituting in (2.6) the numerical values for the constants, we will obtain:

$$\begin{aligned}\varepsilon_i' &= 1 - 5.402 \times 10^{-6} \lambda^2 \frac{\rho_{Mi}}{A_i} (Z_i + f_i') \\ \varepsilon_i'' &= \frac{\lambda}{2\pi} \mu_i = 5.402 \times 10^{-6} \lambda^2 \frac{\rho_{Mi}}{A_i} f_i''\end{aligned} \tag{2.7}$$

In (2.7) the λ is in unit of Å, ρ_{Mi} in unit of g/cm^3, and A_i in unit of g/mol. $\rho_i(Z_i + f_i')/A_i$ is the effective electron density. From (2.7) we can see that for an x-ray beam with wave length of about 1 Å, $(\varepsilon_i'-1)$ and ε_i'' are

of the order of 10^{-5} to 10^{-6} . Sometimes it is convenient to defined the refractive index in the medium by:

$$
\begin{aligned}
n_i &= 1 - \delta_i + i\beta_i = \sqrt{\varepsilon_i} \\
\delta_i &= 2.701 \times 10^{-6} \lambda^2 \frac{\rho_{Mi}}{A_i}(Z_i + f_i') \\
\beta_i &= \frac{\lambda}{4\pi}\mu_i = 2.701 \times 10^{-6} \lambda^2 \frac{\rho_{Mi}}{A_i} f_i''
\end{aligned}
\tag{2.8}
$$

For a medium composed of N uniformly mixed elements, each with a mass fraction P_i, ε is given by:

$$
\begin{aligned}
\varepsilon &= 1 - \frac{4\pi e^2}{m\omega^2}\sum_i^M N_i f_i^* \\
&= 1 - \frac{r_e \lambda^2 N_a}{\pi}\rho_M \sum_i^M \frac{P_i}{A_i}(Z_i + f_i' - if_i'') \\
&= 1 - \frac{r_e \lambda^2 N_a}{\pi}\rho
\end{aligned}
\tag{2.9}
$$

Where ρ_M is the density of the medium. The last line of (2.9) defines the complex effective electron density ρ. Fig. 2.2 shows how the real part of the effective electron density and the linear absorption changes with the mass fraction of a two elements medium at different x-ray energies.

2.2 Dynamic Theory of X-ray Reflectivity

In this thesis, the concept of dynamic theory refers to the methods of solving the reflectivity problem for a layered structure in an exact way, such as the matrix formalism by Vidal and Vincent,[38] and the recursion scheme by Parratt.[20] Kinematical theory, on the other hand, is an approximation that neglect the multiple scattering and is valid only for the reflectivity at an incident angle larger than about twice the critical angle of total reflection. The Born approximation [39] and the so called " single-scattering dynamical theory " [40] are examples of kinematical theory. In solving the reflectivity problem for multilayer structures, the dynamical diffraction theory for perfect crystal developed by Darwin and Ewald [41] are used by some authors.[42] This method can be employed to calculate the reflected intensity about the Bragg peaks only and will not be discussed here.

Let's consider a layered structure with two rough interfaces at z_1 and z_2 (see Fig. 2.3). The real position of the interfaces can be described by a two dimensional surface function $Z_i(x,y)$ which satisfies:

$$h_i(x,y) = Z_i(x,y) - z_i$$
$$\langle h_i(x,y)\rangle_{x,y} = 0, \quad \langle h_i^2(x,y)\rangle_{x,y} = \sigma_i^2 \tag{2.10}$$

Where the σ_i is called the rms roughness of the interface. ε_1, ε_2 and ε_3

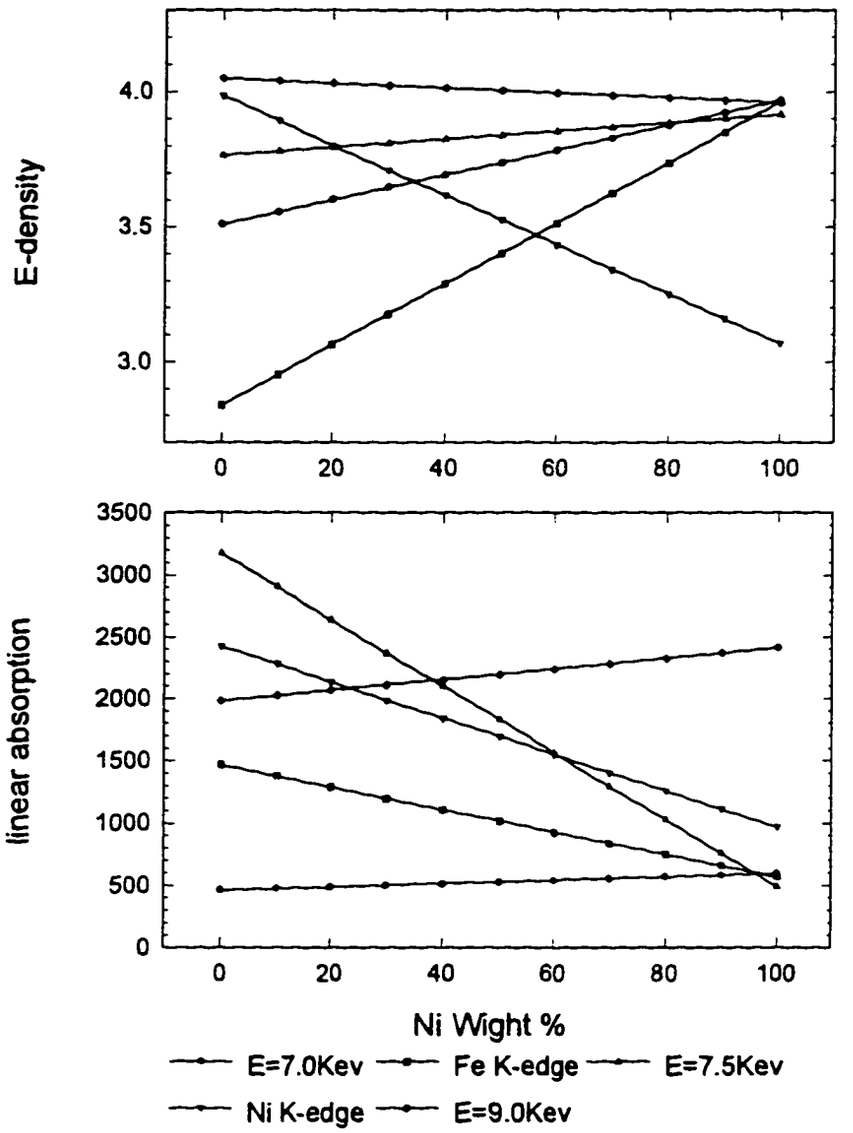

Fig. 2.2 Composition dependence of the electron density and linear absorption at different x-ray energies.

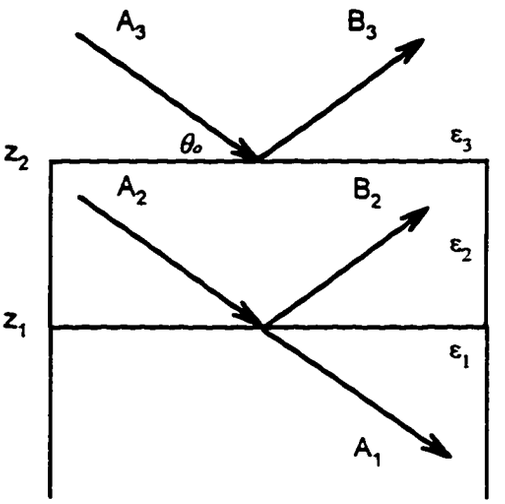

Fig. 2.3 Schematic representation of x-ray reflectivity from a two-interface structure.

are the dielectric constants of the three homogeneous media divided by the two interfaces.

The specular components of the x-ray waves in the three media ε_1, ε_2 and ε_3 can be represented by:

$$\begin{aligned} E_3 &= A_3 e^{-ik_{3z}(z-z_2)} + B_3 e^{ik_{3z}(z-z_2)} \\ E_2 &= A_2 e^{-ik_{2z}(z-z_1)} + B_2 e^{ik_{2z}(z-z_1)} \\ E_1 &= A_1 e^{-ik_{1z}(z-z_1)} \end{aligned} \tag{2.11}$$

where $k_{jz} = k_0\sqrt{\varepsilon_j - \cos^2\theta_0}$ is the z-component of the wave vector in medium j, k_0 the x-ray wave vector in vacuum and θ_0 the glancing angle of incidence.

For ideal interfaces ($\sigma = 0$), the continuity of the electric field and its first derivative across the interface gives for σ polarization (**E** perpendicular to the incident plane),

$$\begin{pmatrix} A_3 \\ B_3 \end{pmatrix} = \begin{pmatrix} a_{23}^{+} e^{-ik_{2z}d} & a_{23}^{-} e^{ik_{2z}d} \\ a_{23}^{-} e^{-ik_{2z}d} & a_{23}^{+} e^{ik_{2z}d} \end{pmatrix} \begin{pmatrix} A_2 \\ B_2 \end{pmatrix} \tag{2.12}$$

where $d = z_2 - z_1$ and

$$a_{23}^{\pm} = \frac{1}{2}\left(1 \pm \frac{k_{2z}}{k_{3z}}\right) \tag{2.13}$$

A_2 and B_2 are given similarly by:

$$A_2 = \frac{1}{2}(1+\frac{k_{1z}}{k_{2z}})A_1$$
$$B_2 = \frac{1}{2}(1-\frac{k_{1z}}{k_{2z}})A_1 \qquad (2.14)$$

The reflectivity of the whole structure is given by B_3/A_3 . A_1 in (2.14) is a constant and will not appear in the final result. The extension of above procedure to multilayers with n interfaces is straight forward,

$$\begin{pmatrix} A_{n+1} \\ B_{n+1} \end{pmatrix} = \mathbf{M}_{n+1,n}\mathbf{M}_{n,n-1}\cdots\mathbf{M}_{2,1}\begin{pmatrix} A_1 \\ 0 \end{pmatrix} \qquad (2.15)$$

where the **M**'s are matrices defined in a similar way as in (2.12).

For a rough interface, when the roughness σ is less than the thickness of the layer, a matrix form including the nonideal interface effects can be given by applying Green's theorem to the interface:[38]

$$\begin{pmatrix} A_3 \\ B_3 \end{pmatrix} = \begin{pmatrix} a_{23}^{+}g_{23}^{-}e^{-ik_{2z}d} & a_{23}^{-}g_{23}^{+*}e^{ik_{2z}d} \\ a_{23}^{-}g_{23}^{+}e^{-ik_{2z}d} & a_{23}^{+}g_{23}^{-*}e^{ik_{2z}d} \end{pmatrix}\begin{pmatrix} A_2 \\ B_2 \end{pmatrix} \qquad (2.16)$$

where

$$g_{23}^{\pm} = \left\langle e^{-i(k_{2z}\pm k_{1z})h_2(x,y)} \right\rangle_{x,y} \qquad (2.17)$$

The symbol $\langle\ \rangle_{x,y}$ means in-plane average. Assuming the ergodicuty of the profile function *h(x,y)*, (2.17) can be written as:

$$g_{23}^{\pm} = \int_{-\infty}^{\infty} e^{-i(k_{2z}\pm k_{1z})z}\omega(z)dz \qquad (2.18)$$

Where z is relative to the average position of the interface and $\omega(z)$ is the height distribution function (probability density) at the interface. If, for

example, the probability density of the roughness perturbation at the interface is assumed to be Gaussian:

$$\omega(z) = (2\pi\sigma)^{-\frac{1}{2}} \exp\left[-z^2/(2\sigma^2)\right] \tag{2.19}$$

Then the characteristic function $g_{23}^{\pm}$ is real and given by,

$$g_{23}^{\pm} = g_{23}^{\pm *} = \exp[-(k_{2z} \pm k_{3z})^2 \frac{\sigma_2^2}{2}] \tag{2.20}$$

To calculate the reflectivity from a single interface, set B_2 in (2.16) to zero, then,

$$r = \frac{B_3}{A_3} = \frac{a_{23}^- g_{23}^+}{a_{23}^+ g_{23}^-} = \frac{k_{3z} - k_{2z}}{k_{3z} + k_{2z}} e^{-2k_{2z}k_{3z}\sigma_2^2} \tag{2.21}$$

It is the well known Fresnel reflectivity equation for an ideal interface multiplied by a Gaussian form factor. In general, the reflectivity from a rough or graded interface can always be written in the form of a Fresnel equation times a form factor, which is determined by it's probability density $\omega(z)$. We will come back to this point later.

For a two interface structure, from (2.16), one can get:

$$\begin{aligned} r_3 = \frac{B_3}{A_3} &= \frac{A_2 a_{23}^- g_{23}^+ e^{-ik_{2z}d} + B_2 a_{23}^+ g_{23}^{-*} e^{ik_{2z}d}}{A_2 a_{23}^+ g_{23}^- e^{-ik_{2z}d} + B_2 a_{23}^- g_{23}^{+*} e^{ik_{2z}d}} \\ &= \frac{r_{23} + r_2 e^{2ik_{2z}d}}{1 + r_{23} r_2 e^{2ik_{2z}d}} \end{aligned} \tag{2.22}$$

where

$$r_{23} = \frac{k_{3z} - k_{2z}}{k_{3z} + k_{2z}} F_{23} = \frac{k_{3z} - k_{2z}}{k_{3z} + k_{2z}} \frac{g_{23}^+}{g_{23}^-} \tag{2.23}$$

is the reflectivity from an individual interface. In (2.22) and (2.23) we have assumed that the probability densities are symmetric functions, i. e. $\omega(z) = \omega(-z)$, so the characteristic functions $g_{ij}^{\pm}$ are real functions. The last expression in (2.22) is actually the recursion formula used by Parrat[20] if we replace the subscript 2 and 3 with N-1 and N, except that now the reflectivity for an individual interface is given by (2.23) instead of the simple Fresnel equation. The matrix formalism and the recursion scheme are equivalent in the case of a symmetric probability density.

From the recursion scheme we can derive a formula which is especially useful in calculating the reflectivity from a very thick multilayer with a constant repetition period. By "very thick " we mean the total thickness of the multilayer exceeds the sensitive depth of x-ray reflectivity measurements, which is mainly limited by the angular resolution of the experiment setup. For example, if the angular resolution is 0.01°, the sensitive depth estimated by the Bragg law is about 3000 Å. In this case, the r_N and r_{N-2} defined in (2.22) are equal and the substrate information is not relevant, by using the recursion twice and set $r_N = r_{N-2}$, we will have:

$$r_N = \frac{-b + \sqrt{b^2 - 4ac}}{2a} \tag{2.24}$$

with

$$\begin{aligned} a &= (r_{12} + r_{21} e^{2ik_{1z}d_1}) e^{2ik_{2z}d_2} \\ b &= 1 + r_{12} r_{21} (e^{2ik_{1z}d_1} - e^{2ik_{2z}d_2}) - e^{2ik_{1z}d_1} e^{2ik_{2z}d_2} \\ c &= -r_{12} - r_{21} e^{2ik_{1z}d_1} \end{aligned} \tag{2.25}$$

where d_1 and d_2 are the thickness of the two component layers in each repetition period, r_{12} and r_{21} are the reflectivities of individual interfaces, defined in a similar way as (2.23), assuming medium 2 is the top layer.

2.3 Kinematic Theory of X-ray Reflectivity

In the standard kinematic theory of x-ray reflectivity, Born Approximation,[43] the reflected intensity is given by:

$$R = |r(Q_z)|^2 = \frac{(4\pi r_e N_a)^2}{Q_z^4}\left|\int \frac{d\rho}{dz} e^{iQ_z z} dz\right|^2 \tag{2.26}$$

where $Q_z = 2k_{0z}$ is the momentum transfer. This expression neglects both the multiple scattering of x-rays and the refraction effects. Therefore it is not valid for reflectivity at small angles and also not suitable for multilayers, as it will give a wrong Bragg peak position. (See Fig. 2.4)

The importance of the Born approximation is that it relates the measured intensity to the Fourier transform of the density profile derivative. From (2.26) the autocorrelation function (ACF) , or Patterson function can be derived by merely taking a Fourier transform:

$$\begin{aligned} ACF\left(\frac{d\rho}{dz}\right) &= \int_{-\infty}^{\infty} \frac{d\rho(s)}{ds}\frac{d\rho(z+s)}{ds} ds \\ &= \text{const} \int_{-\infty}^{\infty} Q_z^4 R(Q_z) e^{-iQ_z z} dQ_z \end{aligned} \tag{2.27}$$

(2.27) is useful in the qualitative interpretation of the experiment data,[25,30] it also becomes the starting point of some Fourier-Synthesis

methods trying to calculate the density profile directly from the reflectivity data.[29,44]

There are several forms of pseudokinematical theories that make corrections over the standard Born approximation.[45] These corrections usually involve two steps. First the prefactor in (2.26) is replaced with the Fresnel reflectivity of the substrate, thus avoid the divergence at small angles. The next step is to replace the vacuum path length $Q_z z$ in the phase factor of (2.26) with a refraction-corrected path length. The most straight forward and effective approach in doing this is given by the "single-scattering dynamical theory",[45]

$$r = r_{01} + r_{12}e^{2ik_{1z}d_1} + r_{23}e^{2i(k_{1z}d_1+k_{2z}d_2)} + \cdots + r_{n,n+1}e^{2i\sum_{l=1}^{n}k_{lz}d_l} \tag{2.28}$$

for a multilayer with n sections. (2.28) can be obtained from (2.22) by simply dropping the r^2 term, that is, the double scattering term. For a two-component periodical multilayer with n periods, (2.28) is reduced to:

$$\begin{aligned} r = r_{01} &+ r_{12}e^{2ik_{1z}d_1}\left(\frac{1-e^{2in(k_{1z}d_1+k_{2z}d_2)}}{1-e^{2i(k_{1z}d_1+k_{2z}d_2)}}\right) \\ &+ r_{21}e^{2i(k_{1z}d_1+k_{2z}d_2)}\left(\frac{1-e^{2i(n-1)(k_{1z}d_1+k_{2z}d_2)}}{1-e^{2i(k_{1z}d_1+k_{2z}d_2)}}\right) + r_{2n,2n+1}e^{2in(k_{1z}d_1+k_{2z}d_2)} \end{aligned} \tag{2.29}$$

For an arbitrary graded interface, the density profile can be approximated by n-steps (or boxes) function, applying (2.28) and let n tend to infinite, we will have:

$$r = \sum_{l=0}^{n} r_{l,l+1}e^{2i\sum_{j=0}^{l}k_{jz}d_j} \xrightarrow{n\to\infty} \frac{k_0^2}{4}\int_0^D \frac{1}{k_z^2}\frac{d\varepsilon}{dz}e^{2i\int_0^z k_z ds}dz \tag{2.30}$$

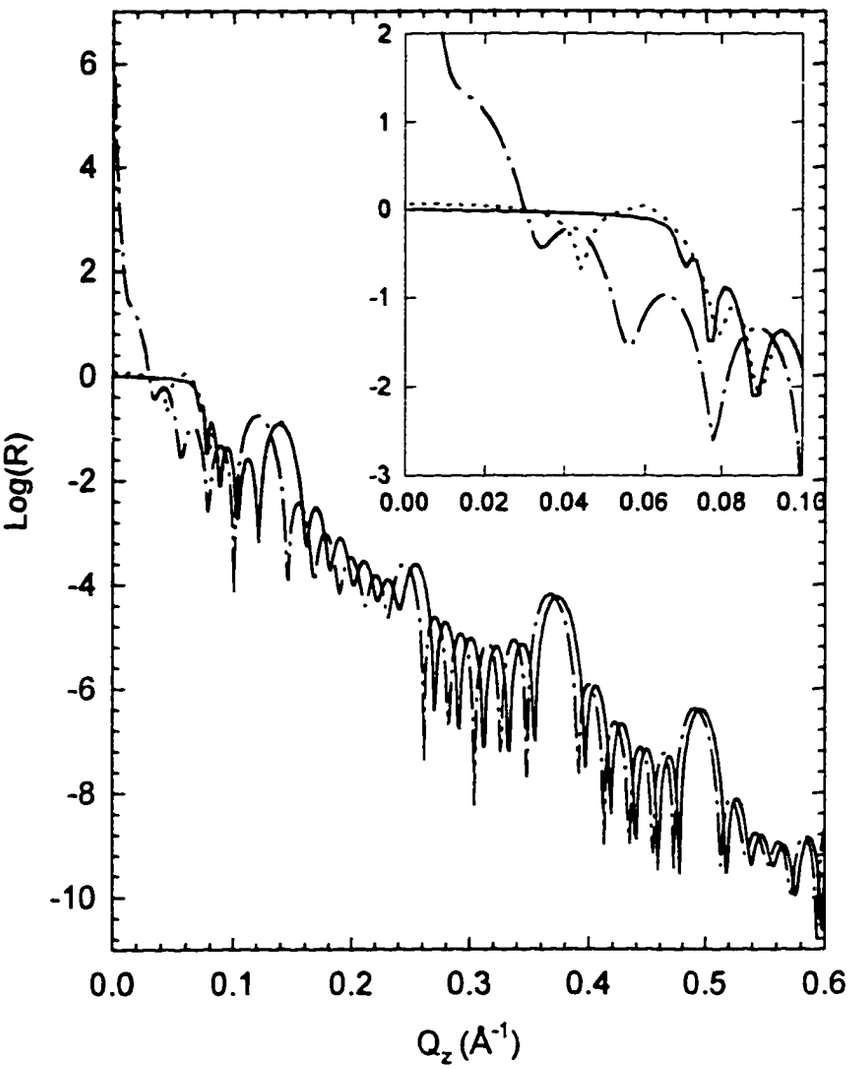

Fig. 2.4 Calculated reflectivity curves from a multilayer with six bi-layer periods. The solid line is for the dynamical calculation (Matrix formalism), the dot line for the single-scattering theory and the dash-dot line for Born approximation.

where $k_z(z) = k_0(\varepsilon(z) - \cos^2\theta)^{1/2}$, and the [0, D] is defined as the region where the derivative of the density profile is not zero. Fig. 2.5 shows the reflectivity from a linear density profile calculated with (2.30), compared with those with other methods discussed in the next section. Note that for a linear density profile, the phase factor in (2.30) can be written explicitly as:

$$\int_0^z k_z(s)ds = k_0\int_0^z (\varepsilon(s) - \cos^2(\theta))^{1/2} ds = \frac{2}{3a}(k_z^3(z) - k_z^3(0)) \qquad (2.31)$$

where a is the derivative of k_z^2, a constant for a linear density profile.

2.4 Interface Model

In this section we will discuss different interface models and methods for calculating the reflectivity from these model interfaces.

Consider a single interface, the reflectivity coefficient r will be given by (2.23):

$$r_{12} = \frac{k_{2z} - k_{1z}}{k_{2z} + k_{1z}} F_{12} = \frac{k_{2z} - k_{1z}}{k_{2z} + k_{1z}} \frac{\left\langle e^{-i(k_{1z}+k_{2z})h(x,y)} \right\rangle_{x,y}}{\left\langle e^{-i(k_{1z}-k_{2z})h(x,y)} \right\rangle_{x,y}} \qquad (2.32)$$

F_{12} is the form factor added to the Fresnel's reflectivity equation of an ideal interface. It can be calculated with (2.18) if the probability density $\omega(z)$ is known. The probability density $\omega(z)$, on the other hand, can be related to the derivative of the in-plane average of the effective electron density profile by:

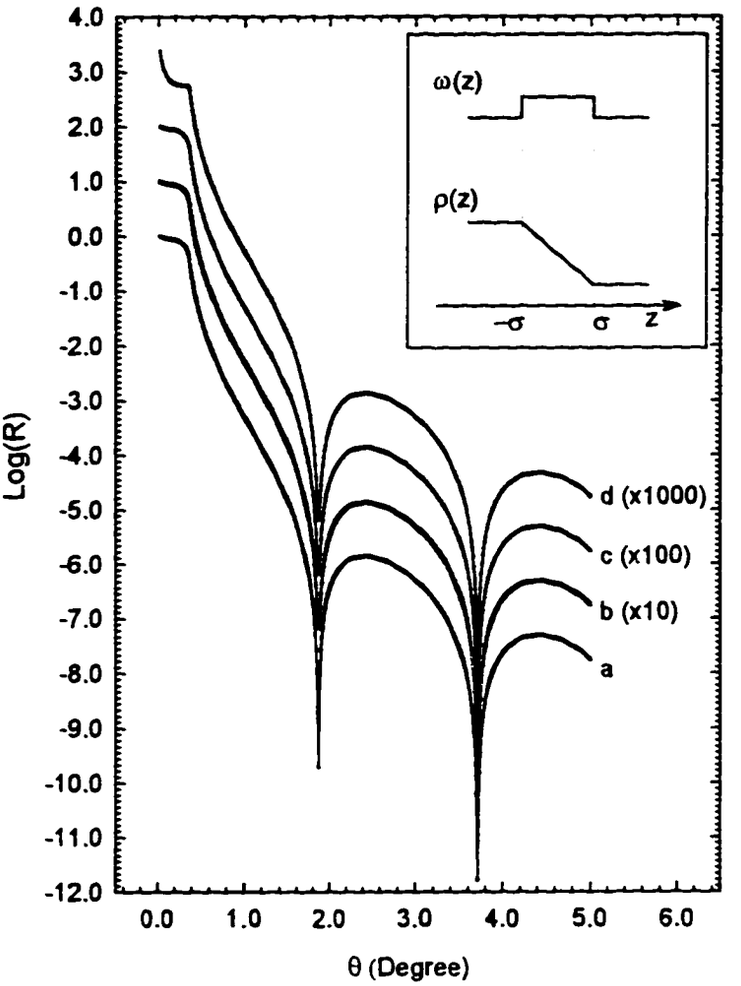

Fig. 2.5 Reflectivity simulated from a linear density profile. (a) Form factor method (2.32), (b) Multi-step function (thin density box method), (c) exact solution, use Hankel functions as wave functions and (d) single scattering approximation (2.30). The interface model is shown in the inlet. The half width σ is 12 angstrom.

$$\omega(z) = \frac{1}{\rho_2 - \rho_1} \frac{d\rho}{dz} \tag{2.33}$$

Where ρ_1 and ρ_2 are the electron densities of the homogeneous media on the two sides of the interface. (2.33) implies a physical observation: the specular reflectivity measurements can not distinguish between the two kinds of interface broadening, namely, a rough interface with sharp local boundary and an overall smooth interface with graded density profile. In fact, the x-ray optics in this two cases is different. For a smooth interface, the radiation energy of the incident beam propagates in two directions only, that is, in the directions of reflection and refraction. The broadening of the interface decreases the reflected intensity while increase the refracted intensity. In the case of a rough interface, part of the incident energy flux will be scattered in to off-specular directions. This is called diffused scattering and can be observed by transverse scans. Fig. 2.6 shows an example of transverse diffuse scattering measurements.

To calculate the x-ray specular reflectivity from a rough interface, one has to assume a probability density function for the interface position in the direction of the surface normal. this often leads to a Gaussian distribution (2.19). For the reflectivity in the low Q_z region, or in the case of a small interfacial roughness, the Gaussian distribution can reasonably account for almost any interface form since the higher cumulant terms are negligible. However, in the region of relatively higher Q_z, and/or for an interface with large roughness or width, the Gaussian distribution is not necessarily the right choice. Eq. (2.18) and (2.32) can be used with other forms of

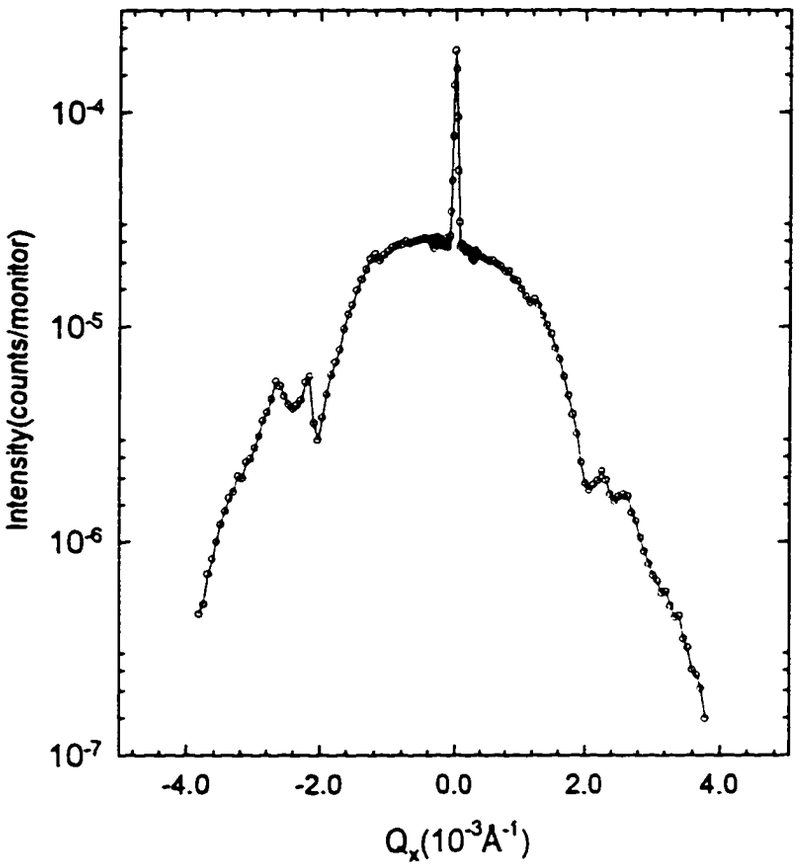

Fig. 2.6 Transverse scan of diffuse and specular x-ray scattering for a Ni/W multi-layer across a superlattice Bragg peak. The narrow central potion represents the true specular folded with instrumental resolution.

probability density functions. Some examples are given in following paragraphs.

Constant distribution

$$\begin{aligned} \omega(z) &= \frac{1}{2\sigma} && |z| < \sigma \\ &= 0 && |z| > \sigma \end{aligned} \tag{2.34}$$

$$F_{12} = \frac{k_{2z} - k_{1z}}{k_{2z} + k_{1z}} \frac{\sin[\sigma(k_{2z} + k_{1z})]}{\sin[\sigma(k_{2z} - k_{1z})]} \tag{2.35}$$

A constant distribution corresponds to a linear density profile. the problem of x-ray propagation in a linear density medium can be solved exactly (cf. next section). Fig. 2.5 shows the calculated reflectivity curves from a linear medium with (2.32) (rough boundary model), (2.30) (graded interface model, single scattering approximation) and the exact solution (also graded interface model). The consistency between the three curves gives a numerical proof of the equivalence between a rough and a graded interface under specular reflectivity condition.

Lorentz distribution

$$\omega(z) = \frac{1}{2\sigma} e^{-\frac{|z|}{\sigma}} \tag{2.36}$$

$$F_{12} = \frac{1 + (k_{1z} - k_{2z})^2 \sigma^2}{1 + (k_{1z} + k_{2z})^2 \sigma^2} \tag{2.37}$$

The reflectivity from an interface with a Lorentz distribution calculated with (2.37) is shown in Fig. 2.7. For comparison, a step function

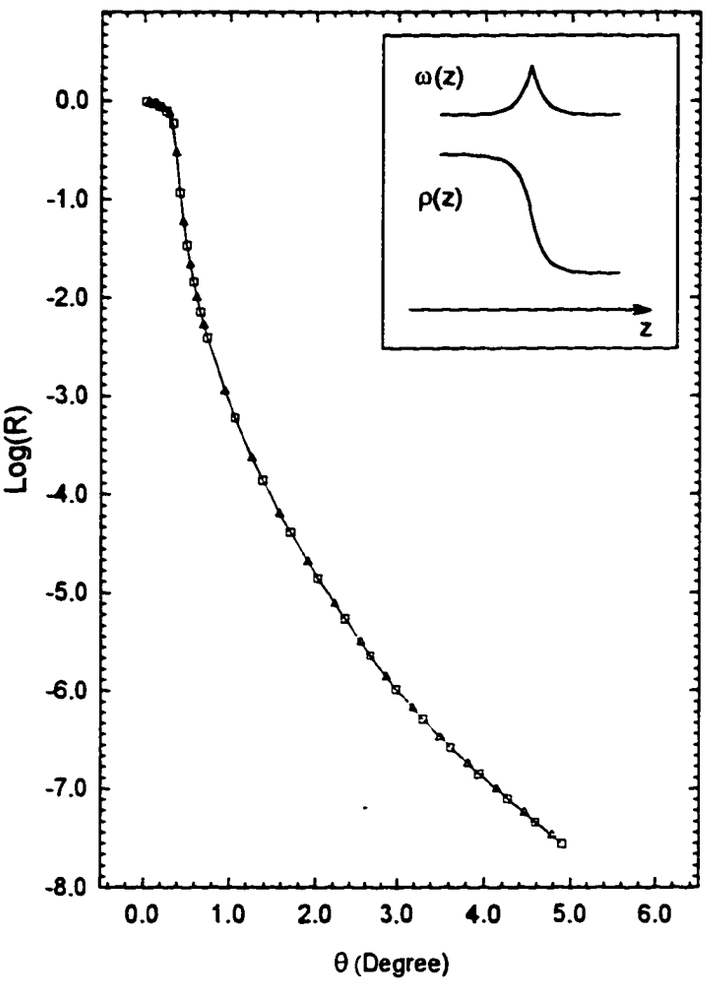

Fig. 2.7 Calculated reflectivity from a Lorentz distribution (2.36) with σ = 4.0 Angstrom. The squares are for the Form factor method and the triangles for thin density box method. The interface model is shown in the inlet.

(thin density boxes) calculation of the graded density profile is also shown in Fig. 2.7. The two calculations give consistent reflectivity curves.

Cosine distribution

$$\omega(z) = \frac{\pi}{2d}\cos\frac{\pi z}{d} \qquad |z| < \frac{d}{2}$$
$$= 0 \qquad |z| > \frac{d}{2} \tag{2.38}$$

$$F_{12} = \frac{\cos[d(k_{1z}+k_{2z})/2]}{\cos[d(k_{1z}-k_{2z})/2]}\frac{1-d(k_{1z}-k_{2z})/\pi}{1-d(k_{1z}+k_{2z})/\pi} \tag{2.39}$$

Fig. 2.8 shows the reflectivity calculated with (2.37) and the graded density model (step function approximation).

The above examples demonstrated the flexibility of the form factor methods. They are also numerical proofs of the equivalence between the rough interface model and the graded density model in specular reflectivity calculation. In the analysis of x-ray reflectivity data, one can also assume other forms of distribution functions, and calculated the corresponding form factor. The effects of different interface models usually show up only at high Q_z values of the reflectivity curves. (Fig. 2.9)

The form factor method is based on a perturbation to the plane wave solution. The reflectivity calculated with this method is questionable when the thickness of the layer is less than or equal to the surface roughness of the interface.[38] When there is a large in depth spatial variation region across

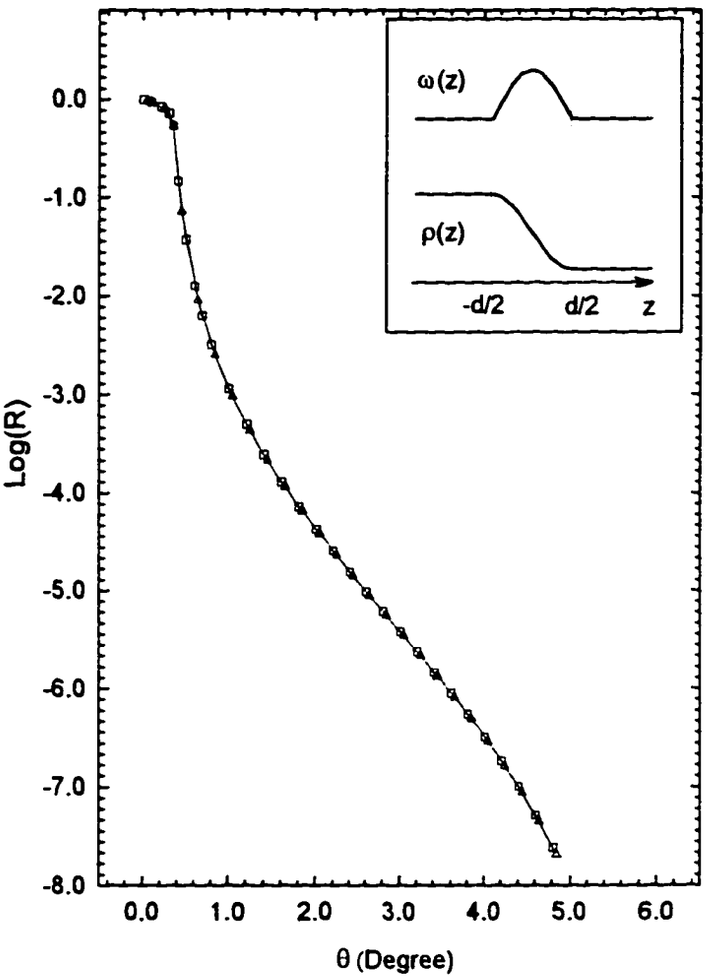

Fig. 2.8 Calculated reflectivity from a Cosine distribution (2.38) with d = 8.0 Angstrom. The squares are for the Form factor method and the triangles for the thin density box method. The interface model is shown in the inlet.

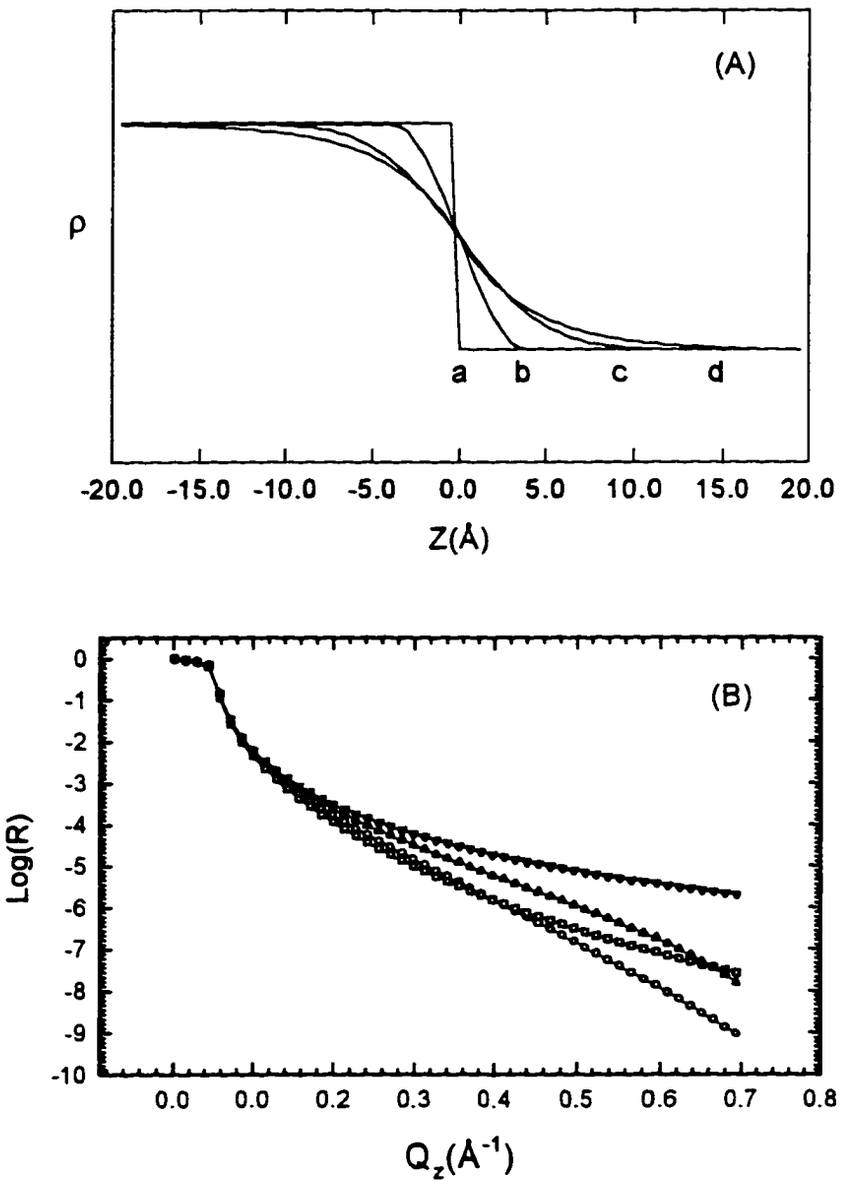

Fig. 2.9 Comparison of reflectivity curves calculated with different nterface model. (A) shows the density profiles of the ideal sharp interface (a), Cosine distribution (b), Gaussian distribution (c) and the Lorentz distribution (d). (B) shows the reflectivity curves for a (∇), b (Δ), c (O) and d (□).

the interface, one has to assume a stratified medium and solve the one dimensional Helmholtz equation for the electromagnetic fields.[28]

$$\frac{\partial^2 u}{\partial z^2} + k_0^2(\varepsilon(z) - 1 + \sin^2\theta_0)u(z) = 0 \tag{2.40}$$

Where *u(z)* represents the electric field in the medium.

One way to solve (2.40) is to use a multi-step function (thin density boxes) to approach the real (in plane averaged) electron density. In each thin box, the plane wave solution is assumed and then (2.22) can be used to calculated the reflectivity. On the other hand, it is well known that (2.40) can be solved analytically for a linear density profile. In next section we will give a formalism for solving (2.40) by approaching the density profile with a series of straight line segments. This method has been used to analyze the reflectivity data from the Ni/Fe alloy thin film sample, which will be discussed in detail in Chapter 4.

2.5 The solution of the X-ray Reflectivity Problem for a Linear Stratified Media

Define: (see Fig. 2.10)

$$\Delta(z) = 1 - \varepsilon(z) \tag{2.41}$$

$$\Delta(z)=\begin{cases}\Delta_1 & z<z_1\\ b_1(z-z_2)+\Delta_2 & z_1<z<z_2\\ b_2(z-z_3)+\Delta_3 & z_2<z<z_3\\ \Delta_3 & z>z_3\end{cases} \tag{2.42}$$

The equation satisfied by the E field in the media is:

$$u''+k_0^2\sin^2\theta_0 u-k_0^2\Delta(z)u=0 \tag{2.43}$$

Where $k_0=\frac{2\pi}{\lambda}$ and θ_0 is the angle of incidence of the X-ray beam.

For $z > z_3$:

$$\begin{aligned}u_3 &= A_3e^{-ik_{3z}(z-z_3)}+B_3e^{ik_{3z}(z-z_3)}\\ u_3' &= -ik_{3z}(A_3e^{-ik_{3z}(z-z_3)}-B_3e^{ik_{3z}(z-z_3)})\end{aligned} \tag{2.44}$$

For $z_2 < z < z_3$:

$$\begin{aligned}u_2 &= A_2f_2(z)+B_2g_2(z)\\ u_2' &= A_2f_2'(z)+B_2g_2'(z)\end{aligned} \tag{2.45}$$

where:

$$\begin{aligned}f_2(z) &= \xi_2^{1/2}(z)H_{1/3}^{(2)}(\tfrac{2}{3}\xi_2^{3/2}(z))\\ g_2(z) &= \xi_2^{1/2}(z)H_{1/3}^{(1)}(\tfrac{2}{3}\xi_2^{3/2}(z))\end{aligned} \tag{2.46}$$

and

$$\begin{aligned}\xi_2 &= l_2^2k_0^2(\sin^2\theta_0-\Delta(z))\\ &= l_2^2k_0^2(\sin^2\theta_0-\Delta_3-b_2(z-z_3))\\ l_2^3 &= -1/(b_2k_0^2)\end{aligned} \tag{2.47}$$

$H_{1/3}^{(i)}(x)$ is the 1/3 order Henkel function.

At $z = z_3$, we apply the boundary conditions:

$$\begin{aligned} u_3(z_3) &= u_2(z_3) \\ u_3'(z_3) &= u_2'(z_3) \end{aligned} \tag{2.48}$$

That is:

$$\begin{aligned} A_3 + B_3 &= A_2 f_2(z_3) + B_2 g_2(z_3) \\ -i\beta_3(A_3 - B_3) &= A_2 f_2'(z_3) + B_2 g_2'(z_3) \end{aligned} \tag{2.49}$$

So:

$$\begin{aligned} \begin{pmatrix} A_3 \\ B_3 \end{pmatrix} &= \frac{1}{2ik_{3z}} \begin{pmatrix} ik_{3z}f_2 - f_2' & ik_{3z}g_2 - g_2' \\ ik_{3z}f_2 + f_2' & ik_{3z}g_2 + g_2' \end{pmatrix} \begin{pmatrix} A_2 \\ B_2 \end{pmatrix} \\ &= M_{32} \begin{pmatrix} A_2 \\ B_2 \end{pmatrix} \end{aligned} \tag{2.50}$$

For $z_1 < z < z_2$

$$\begin{aligned} u_1(z) &= A_1 f_1(z) + B_1 g_1(z) \\ u_1'(z) &= A_1 f_1'(z) + B_1 g_1'(z) \end{aligned} \tag{2.51}$$

The definition of f_1, g_1 is similar to that of f_2, g_2.

Applying the boundary conditions at $z = z_2$, we have:

$$\begin{aligned} \begin{pmatrix} A_2 \\ B_2 \end{pmatrix} &= \frac{\pi l_2}{6i} \begin{pmatrix} f_1 g_2' - f_1' g_2 & g_1 g_2' - g_1' g_2 \\ f_2 f_1' - f_2' f_1 & f_2 g_1' - f_2' g_1 \end{pmatrix} \begin{pmatrix} A_1 \\ B_1 \end{pmatrix} \\ &= M_{21} \begin{pmatrix} A_1 \\ B_1 \end{pmatrix} \end{aligned} \tag{2.52}$$

For $z < z_1$

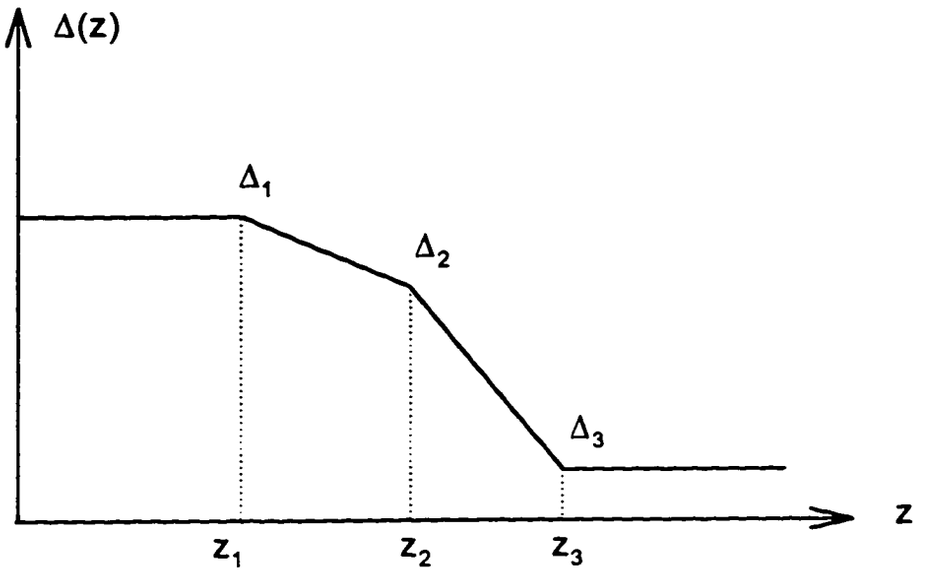

Fig. 2.10 Linear segments description of a model interface.

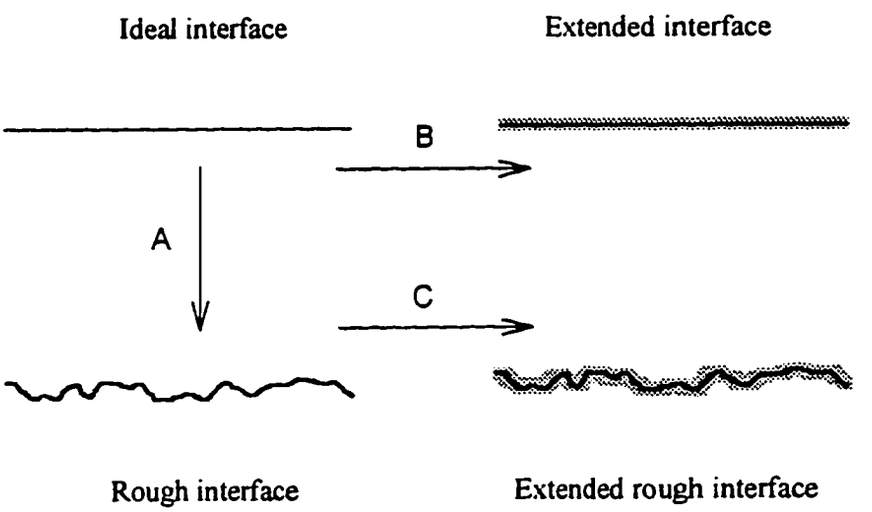

Fig. 2.11 Characterization of interfaces.

$$u_0 = A_0 e^{-ik_{1z}(z-z_1)} + B_0 e^{ik_{1z}(z-z_1)}$$
$$u_0' = -ik_{1z}(A_0 e^{-ik_{1z}(z-z_1)} - B_0 e^{ik_{1z}(z-z_1)}) \tag{2.53}$$

Boundary conditions at $z = z_1$:

$$\begin{pmatrix} A_1 \\ B_1 \end{pmatrix} = \frac{\pi d_1}{6i}\begin{pmatrix} ik_{1z}g_1 + g_1' & -ik_{1z}g_1 + g_1' \\ -ik_{1z}f_1 - f_1' & ik_{1z}f_1 - f_1' \end{pmatrix}\begin{pmatrix} A_0 \\ B_0 \end{pmatrix}$$
$$= M_{10}\begin{pmatrix} A_0 \\ B_0 \end{pmatrix} \tag{2.54}$$

Combining (2.50), (2.52) and (2.54), we have:

$$\begin{pmatrix} A_3 \\ B_3 \end{pmatrix} = M_{32}M_{21}M_{10}\begin{pmatrix} A_0 \\ B_0 \end{pmatrix} = M_{30}\begin{pmatrix} A_0 \\ B_0 \end{pmatrix} \tag{2.55}$$

The reflectivity coefficient r will be given by:

$$r = \frac{(M_{30})_{21}}{(M_{30})_{11}} \tag{2.56}$$

For a extended rough interface, by assuming that the line shape and the width of the extended interface are the same for all x, one can prove that the reflectivity is given by:

$$r = \frac{(M_{30})_{21}}{(M_{30})_{11}} e^{-2k_{1z}k_{3z}\sigma^2} \tag{2.57}$$

In following text we will derive (2.57) by applying the Green theorem onto an extended rough interface.

There are two ways of characterizing an interface. One way is to assume a zigzag but sharp boundary between two media (see Fig. 2.11A). The reflectivity from this kind of interface is given by (2.21) provided that

$q\sigma<1$.[46] The other way is to assume a smooth but extended boundary and solve the Helmholtz equation (2.40). (see Fig. 2.11B) .It is well accepted that the Gaussian probability density function of the boundary position which leads to the Gaussian factor in (2.21) can be used to derive an effective refraction index profile. If this index function (or dielectric constant function) is inserted into (2.40), one get the same reflectivity by solving the differential equation. So it seems that the two way of characterizing the interfaces are equivalent and one can not tell the difference just from the specular reflectivity. However, these two kinds of interfaces are not completely equivalent because: (1) in case A , there is a limit $q\sigma<1$ while in case B there is no limitation in the width of the interface. When there is a large in depth spatial variation region across the interface, it can not be described by a simple Gaussian factor. (2) In case A part of the energy flux goes into diffused scattering while in case B all the energy flux goes either into specular reflection or refracted beam.

We will try to demonstrate that the two ways (A and B) can be combined together to give a more complete description of an interface. (see Fig. 2.11C). We will prove that for a rough extended interface, the matrix is given by adding the same factor to the matrix elements of the smooth extended interface. The refraction index profile along z can be of any form. However, we assume that the interface has the same local, gradual surface profile, but that its boundary varies in the x-y plane as some function $h(x,y)$.

For an ideal interface at $z = z_0$, the electric field on the two sides can be written as:

$$\begin{aligned}\hat{E}_2 &= (\hat{A}e^{-ik_{2z}(z-z_0)} + \hat{B}e^{ik_{2z}(z-z_0)})e^{i\alpha x} \quad z < z_0 \\ \hat{E}_1 &= (\hat{C}e^{-ik_{1z}(z-z_0)} + \hat{D}e^{ik_{1z}(z-z_0)})e^{i\alpha x} \quad z > z_0\end{aligned} \tag{2.58}$$

Where $\alpha = k_0 \cos\theta_0$.

For a smooth extended interface with z1-z2=d, we have:

$$\begin{aligned}E_2' &= (A'e^{-ik_{2z}(z-z_2)} + B'e^{ik_{2z}(z-z_2)})e^{i\alpha x} \quad z < z_2 \\ E_0' &= (A_0'f(z) + B_0'g(z))e^{i\alpha x} \quad z_2 < z < z_1 \\ E_1' &= (C'e^{-ik_{1z}(z-z_1)} + D'e^{ik_{1z}(z-z_1)})e^{i\alpha x} \quad z > z_1\end{aligned} \tag{2.59}$$

where $f(z)$, $g(z)$ are two independent solutions of the Helmholtz equation (2.40) in the region of $[z_2, z_1]$ (see Fig. 2.12). The relation between A', B' and etc. are:

$$\begin{aligned}\begin{pmatrix} A' \\ B' \end{pmatrix} &= M_2(z_2)\begin{pmatrix} A_0' \\ B_0' \end{pmatrix} = M_2(z_2)M_1(z_1)\begin{pmatrix} C' \\ D' \end{pmatrix} \\ &= M(d)\begin{pmatrix} C' \\ D' \end{pmatrix}\end{aligned} \tag{2.60}$$

Note that $M(d) = M_2(z_2)M_1(z_1)$ depends on d only. Applying Green's theorem to the contour MNOP in Fig. 2.12,

$$\iint (\hat{E}\Delta E' - E'\Delta\hat{E})dxdz = \int_{MNOP} (\hat{E}\frac{dE'}{dn} - E'\frac{d\hat{E}}{dn})dl \tag{2.61}$$

Where $\hat{E}$ and E' are defined in (2.58) and (2.59) respectively, with the subscripts ignored.

We then get:

$$2ik_{2z}(A\hat{B} - \hat{A}B) - 2ik_{1z}(C\hat{D} - \hat{C}D) = \left\langle \int_{z2}^{z1} (k^2 - \hat{k}^2)E_0'\hat{E}dz \right\rangle_x \tag{2.62}$$

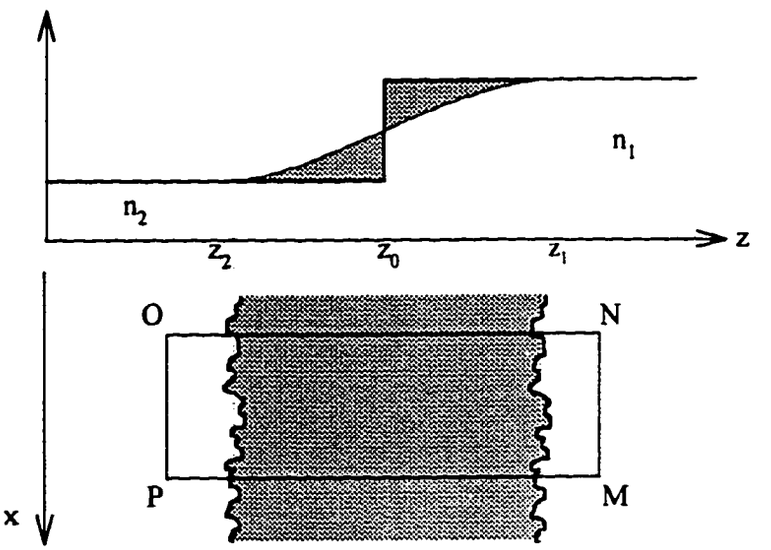

Fig. 2.12 Schematic representation of the extended rough interface and the contour for Green's function.

Where $k^2(z) = k_0^2 \varepsilon^2(z)$ is a gradual function of z between [z_2, z_1] and $\hat{k}^2 = k_0^2 \varepsilon_2^2$ for $z < z_0$ and $\hat{k}^2 = k_0^2 \varepsilon_1^2$ for $z > z_0$. And:

$$\begin{aligned} A &= A' e^{-ik_{2z}(z_2 - z_0)} \\ B &= B' e^{ik_{2z}(z_2 - z_0)} \\ C &= C' e^{-ik_{1z}(z_1 - z_0)} \\ D &= D' e^{ik_{1z}(z_1 - z_0)} \end{aligned} \tag{2.63}$$

Now let

$$\hat{A} = 0,\ \hat{D} = 1 \text{ then } \hat{B} = \frac{2k_{1z}}{k_{1z} + k_{2z}} \text{ and } \hat{C} = -\frac{k_{2z} - k_{1z}}{k_{2z} + k_{1z}} \tag{2.64}$$

This will lead to:

$$\begin{aligned} & 2ik_{2z}(2k_{1z}/(k_{1z} + k_{2z}))A' e^{-ik_{2z}(z_2 - z_0)} \\ & -2ik_{1z}(C' e^{-ik_{1z}(z_1 - z_0)} + (k_{2z} - k_{1z})/(k_{2z} + k_{1z})D' e^{-ik_{1z}(z_1 - z_0)}) \\ & = A_0' \int_{z_2}^{z_1} (k^2 - \hat{k}^2)\hat{E}f(z)dz + B_0' \int_{z_2}^{z_1} (k^2 - \hat{k}^2)\hat{E}g(z)dz \\ & = A_0' F(z_1, z_2) + B_0' G(z_1, z_2) \end{aligned} \tag{2.65}$$

And then,

$$
\begin{aligned}
&\frac{4ik_{1z}k_{2z}}{k_{1z}+k_{2z}}e^{-ik_{2z}(z_2-z_1)}A' \\
&= C'((M_1)_{11}F(z_1,z_2)+(M_1)_{21}G(z_1,z_2)+2ik_{1z}e^{-ik_{1z}(z_1-z_0)}) \\
&\quad + D'((M_1)_{12}F(z_1,z_2)+(M_1)_{22}G(z_1,z_2) \\
&\quad + 2ik_{1z}(k_{2z}-k_{1z})/(k_{2z}+k_{1z})e^{ik_{1z}(z_1-z_0)})
\end{aligned}
\tag{2.66}
$$

Compare to (2.60), we have:

$$
\begin{aligned}
&(M_1)_{11}F(z_1,z_2)+(M_1)_{21}G(z_1,z_2)+2ik_{1z}e^{-ik_{1z}(z_1-z_0)} \\
&= M_{11}(d)\frac{4ik_{1z}k_{2z}}{k_{1z}+k_{2z}}e^{-ik_{2z}(z_2-z_0)} \\
&(M_1)_{12}F(z_1,z_2)+(M_1)_{22}G(z_1,z_2) \\
&+2ik_{1z}(k_{2z}-k_{1z})/(k_{2z}+k_{1z})e^{ik_{1z}(z_1-z_0)} \\
&= M_{12}(d)\frac{4ik_{1z}k_{2z}}{k_{1z}+k_{2z}}e^{-ik_{2z}(z_2-z_0)}
\end{aligned}
\tag{2.67}
$$

Now consider an extended rough interface. The specular component of the electric field is similar to (2.59):

$$
\begin{aligned}
&\overline{E}_2 = (\overline{A}\,e^{-ik_{2z}(z-z_0)}+\overline{B}e^{ik_{2z}(z-z_0)})e^{i\alpha x} && z<z_2 \\
&\overline{E}_0 = (\overline{A}_0\bar{f}(z)+\overline{B}_0\bar{g}(z))e^{i\alpha x} && z_2<z<z_1 \\
&\overline{E}_1 = (\overline{C}e^{-ik_{1z}(z-z_0)}+\overline{D}e^{ik_{1z}(z-z_0)})e^{i\alpha x} && z>z_1
\end{aligned}
\tag{2.68}
$$

Note that $\overline{E}_0$ is the Fourier component of $e^{i\alpha x}$ in the electric field solution within region [z_2, z_1] and now z_2, z_1 are functions of x. Assume $\overline{A}_0, \overline{B}_0$ are related to $\overline{C}, \overline{D}$ by:

$$\begin{pmatrix} \overline{A}_0 \\ \overline{B}_0 \end{pmatrix} = \overline{M}_1(z_1)\begin{pmatrix} \overline{C}' \\ \overline{D}' \end{pmatrix} = \overline{M}_1(z_1)\begin{pmatrix} \overline{C}e^{ik_{1z}(z_1-z_0)} \\ \overline{D}e^{-ik_{1z}(z_1-z_0)} \end{pmatrix} \tag{2.69}$$

Applying Green's theorem to MNOP , we can get an equation in a form similar to (2.66):

$$\begin{aligned} &\frac{4ik_{1z}k_{2z}}{k_{1z}+k_{2z}}\overline{A} = \left\langle \overline{C}'((\overline{M}_1)_{11}\overline{F}(z_1,z_2)+(\overline{M}_1)_{21}\overline{G}(z_1,z_2))\right\rangle_x \\ &+2ik_{1z}\left\langle \overline{C}'e^{-ik_{1z}(z_1-z_0)}\right\rangle_x + \left\langle \overline{D}'((\overline{M}_1)_{12}\overline{F}(z_1,z_2)+(\overline{M}_1)_{22}\overline{G}(z_1,z_2))\right\rangle_x \\ &+2ik_{1z}(k_{2z}-k_{1z})/(k_{2z}+k_{1z})\left\langle \overline{D}'e^{ik_{1z}(z_1-z_0)}\right\rangle_x \end{aligned} \tag{2.70}$$

Because we take the roughness as a perturbation, the function form in the inner parentheses should not deviate much from its zero order form, Eq.(2.67). Without a detail examination on the approximation error, we simply insert the right hand of Eq. (2.67) into (2.70) and end up with:

$$\begin{aligned} \overline{A} &= \left\langle \overline{C}'M_{11}(z_1-z_2)e^{-ik_{2z}(z_2-z_0)}\right\rangle_x \\ &\quad + \left\langle \overline{D}'M_{12}(z_1-z_2)e^{ik_{2z}(z_2-z_0)})\right\rangle_x \\ &= \overline{C}\left\langle e^{ik_{1z}(z_1-z_0)}M_{11}(z_1-z_2)e^{-ik_{2z}(z_2-z_0)}\right\rangle_x \\ &\quad + \overline{D}\left\langle e^{-ik_{1z}(z_1-z_0)}M_{12}(z_1-z_2)e^{ik_{2z}(z_2-z_0)})\right\rangle_x \end{aligned} \tag{2.71}$$

With the assumption that the interface has the same local, gradual refraction index profile, we have $z_1(x)-z_1(x)=d$ independent of x, so the M matrix element can be factor out from the x average parentheses. Assuming a Gaussian probability density ,we will have:

$$\begin{aligned}&\left\langle e^{ik_{1z}(z_1-z_0)}M_{11}(z_1-z_2)e^{-ik_{2z}(z_2-z_0)}\right\rangle_x \\ &\quad = M_{11}(d)e^{i(k_{2z}-k_{1z})z0+ik_{2z}d}\left\langle e^{i(k_{1z}-k_{2z})z_1}\right\rangle_x \\ &\quad = M_{11}(d)e^{i(k_{2z}-k_{1z})z_0+ik_{2z}d}e^{i(k_{1z}-k_{2z})\bar{z}_1}e^{-(k_{1z}-k_{2z})^2\frac{\sigma^2}{2}}\end{aligned} \tag{2.72}$$

So:

$$\overline{A'}=\overline{C'}M_{11}(d)e^{-(k_{1z}-k_{2z})^2\frac{\sigma^2}{2}}+\overline{D'}M_{12}(d)e^{-(k_{1z}+k_{2z})^2\frac{\sigma^2}{2}} \tag{2.73}$$

Where: $\overline{A'}=e^{ik_{2z}(\bar{z}_2-z_0)}\overline{A}$ *etc.*

In a similar way we can get:

$$\overline{B'}=\overline{C'}M_{21}(d)e^{-(k_{1z}+k_{2z})^2\frac{\sigma^2}{2}}+\overline{D'}M_{22}(d)e^{-(k_{1z}-k_{2z})^2\frac{\sigma^2}{2}} \tag{2.74}$$

So at $z=\overline{z_2}$, the reflectivity coefficient r is given by:

$$r=\frac{M_{21}(d)e^{-(k_{1z}+k_{2z})^2\frac{\sigma^2}{2}}}{M_{11}(d)e^{-(k_{1z}-k_{2z})^2\frac{\sigma^2}{2}}}=\frac{M_{21}}{M_{11}}e^{-2k_{1z}k_{2z}\sigma^2} \tag{2.75}$$

(2.57) is thus proved.

CHAPTER 3 EXPERIMENTATION

3.1 Synchrotron Radiation and Beamline Facilities

The resonant reflectivity measurements for this thesis work were conducted at beamline X6B,[47] National Synchrotron Light Source (NSLS) at Brookhaven National Laboratory.

When electrons are accelerated they lose energy by emission of electromagnetic radiation. In a synchrotron or storage ring the electrons are magnetically constrained to travel round a closed path and the consequent centripetal acceleration results in the emission of the so-called synchrotron radiation. This radiation, once the unwanted by-product of high-energy physics researches, is now a highly developed probe of matter at photon energies from a few electron volts to higher energies (100 keV and more).

The continuum x-radiation provided by synchrotron is up to five orders of magnitude more intensive than conventional sources such as x-ray tubes. [48] This intense synchrotron radiation continuum make it possible for a research worker to select the wavelengths most appropriate for the experiment (i.e. resonant reflectivity measurement) and also to scan the wavelength over a large range, as needed for EXAFS experiments. The synchrotron radiation spectrum can be characterized in terms of a critical energy, which is usually defined as:

$$E_c = \frac{3\hbar c\gamma^3}{\rho} \qquad (3.1)$$

Where ρ is the machine radius and γ is defined as E/mc^2, that is, the ratio of the electron's kinetic energy to its rest energy. [49] At NSLS, electrons are accelerated to 2.5 GeV, so $\gamma \approx 5000$. The radius of the x-ray ring is 6.83 meters and the critical energy of the radiation is 5.071 keV. [50] Fig. 3.1 shows the spectral distribution of synchrotron radiation from NSLS. It is calculated with the formula for the universal synchrotron radiation spectrum given in ref. 49. The unit used in Fig. 3.1 for the photon flux is photon per second per mrad (horizontal acceptance angle) per mA (synchrotron current) and per 0.1 percent spectrum bandwidth. The location of the peak of the spectrum and the cut-off are governed by the critical energy. As seen from Fig. 3.1, the peak is at about one half of E_C given by (3.1).

The synchrotron x-ray beam is highly collimated. For nonrelativistic energies the radiation emitted by an accelerated electron gives a dipole pattern. For relativistic velocities the dipole pattern is compressed along the direction of motion. Let φ be the angle between the observation direction and the electron velocity v in the rest frame and φ' in the laboratory frame, the transformation of angle is [51]

$$\tan\varphi' = \frac{\sin\varphi}{\gamma(\beta+\cos\varphi)} \tag{3.2}$$

where $\beta=v/c$.

At $\varphi= 90°$, $\tan\varphi' \approx \varphi' \approx 1/\gamma$. Thus the radiation is emitted in a narrow cone about the tangential direction with a half angular spread of approximately $1/\gamma$ radians, (cf. Fig. 3.2) or roughly 0.25 mrad (0.014°) for

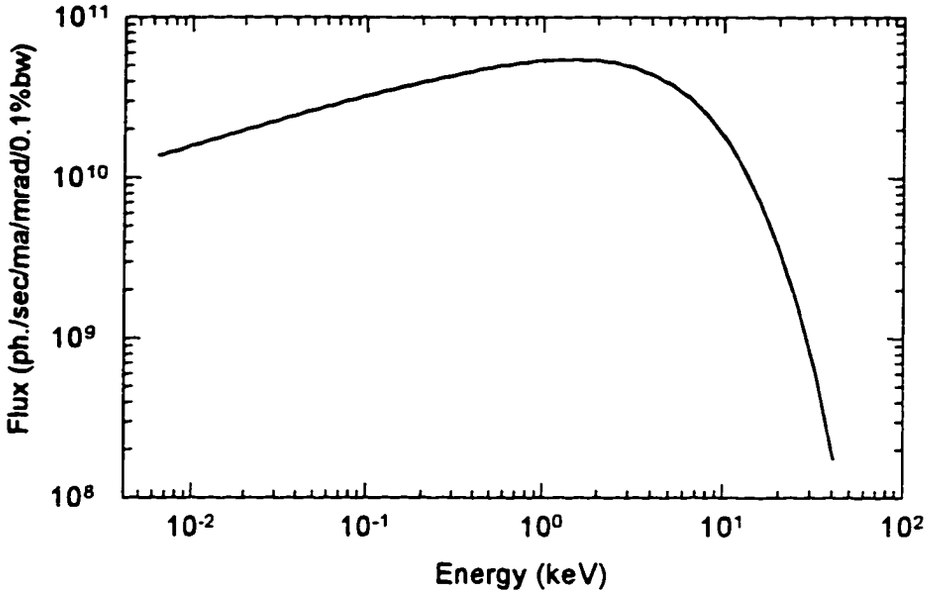

Fig. 3.1 Spectral distribution of synchrotron radiation from NSLS.

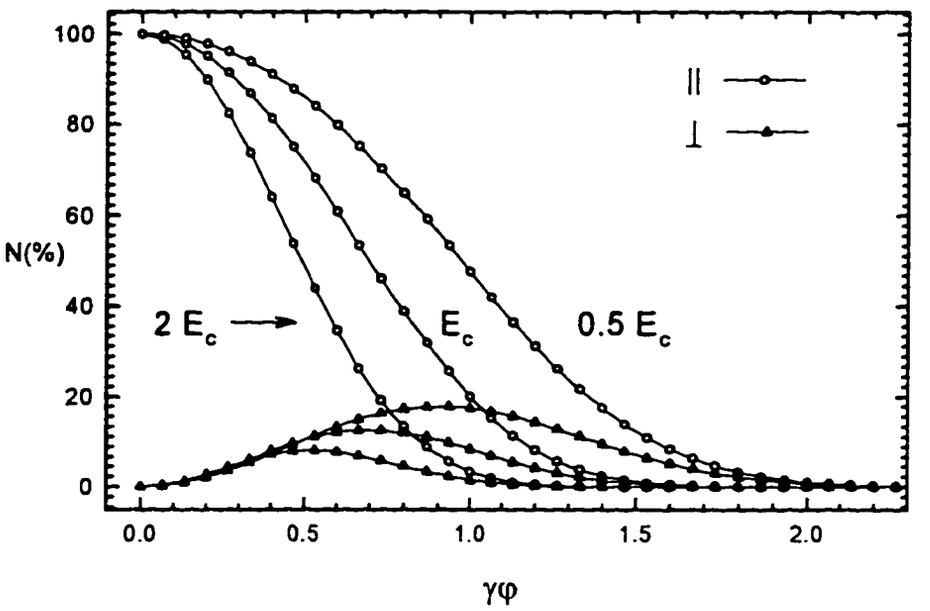

Fig. 3.2 Vertical angular distribution of parallel and perpendicular polarization components.

NSLS. The photon flux given in Fig. 3.1 is integrated over the whole of the vertical distribution. In the plane of the orbiting electrons the observed angular distribution is independent of wavelength due to the time-averaging effect of motion.[49]

Fig. 3.2 shows the two polarization components, the **E** vector parallel and perpendicular to the orbital plane. Because the electron is confined to a single orbital plane the radiation is strongly polarized, and is, as shown in Fig. 3.2, close to 100% polarized in the orbital plane. For reflectivity measurements, generally a narrow beam-defining slit is set at the center of the beam, thus the incident x-ray is considered to be 100% σ-polarization. As the observation angle moves out of the orbital plane the radiation becomes elliptically polarized. When integrated over all angles and energies the parallel component is found to have seven times the power of the perpendicular component.[52]

In summary, synchrotron radiation provides an intense, highly collimated and highly polarized continuous spectrum of x-rays for materials studies. However, more laboratory facilities are needed for utilizing the radiation in different experiments, such as monochromator , x-ray mirror and other beamline components.

The X6B beamline has been constructed at a bending magnet port at the NSLS and became a versatile facility for a variety of x-ray experiments.[53] Main components of the X6B beamline include a pair of premonochromator beam slits, a double-crystal fixed-exit monochromator, a double focusing mirror, and a diffractometer, positioned 8.8, 9.8, 12, 24 m away from the

source, respectively. Fig. 3.3 shows schematically the arrangement of beamline components.

All beamline components outside the experimental hutch are connected by stainless steel beam pipes, which are maintained in a vacuum of low 10^{-8} to high 10^{-9} Torr. The vacuum pass is separated and end-closed by two Be windows. The vertical and horizontal beam slits, upstream the monochromator, were used to control the beam size and energy resolution. The slits are water cooled to dissipate the heat load from the white beam.

In the case of hard x-rays the monochromator design usually takes advantage of the Bragg diffraction planes from single crystals like silicon and germanium. At X6B Si(111) planes are used for energies ranging from 2.34-22.3 keV and Si(220) planes are used for the 3.82-36.0 keV energy range. The energy range is primarily determined by the angle of incidence which varies usually from 57.5° to 5.1°. To make the exit beam travel in the same direction as the incident beam, two pieces of identical single crystals are used for the monochromator. The first crystal acts as a monochromator while the second acts as a reflector.[54] The monochromator is controlled by a single stepping motor with step resolution of 0.09 arcsec, and has a fixed offset of 1 inch between the incident white beam and the exit monochromatic beam. A piezoelectric transducer is used to scan the second crystal with respect to the first crystal. The heat load on the first Si crystal is dissipated through a water-cooled copper block. With Si(111) crystals and a 0.3 mm vertical slits (a vertical acceptance of 0.035 mrad), the energy resolution is 1.4×10^{-4} at 8.0 keV.

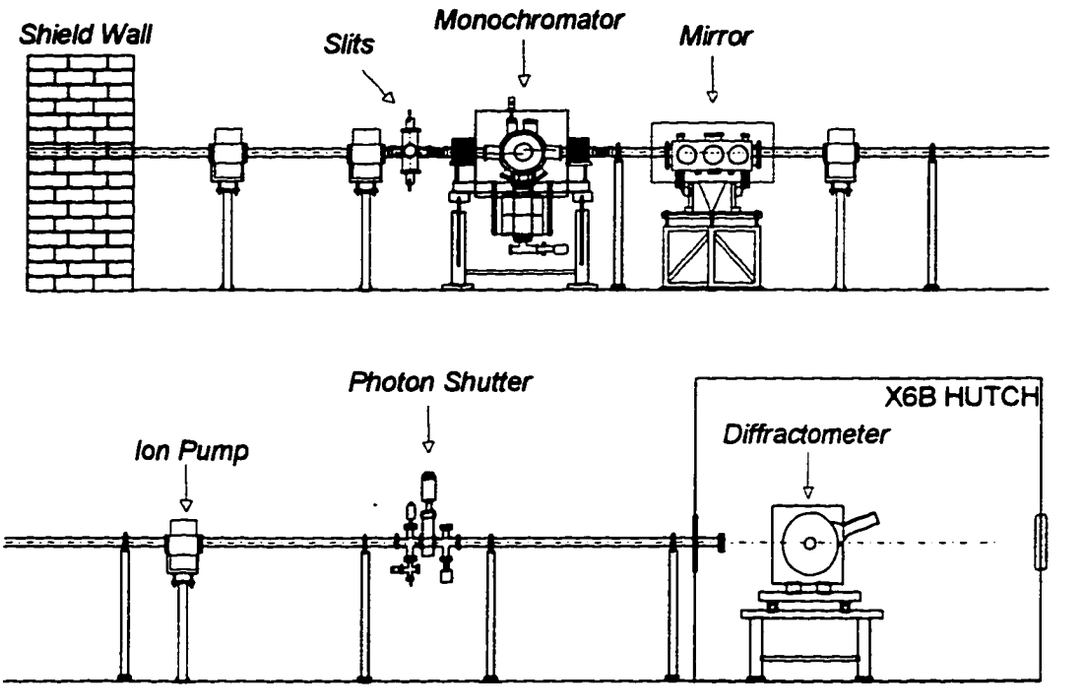

Fig. 3.3 Schematic representation of X6B beamline components.

The second optical element is a cylindrical Rh-coated fuse-silica mirror that is bent to a toroid to focus x-rays both vertically and horizontally. The mirror has a fixed sagittal radius of 8.0 cm and an adjustable meridional radius, nominally set to 2500 m for an incidence angle of 6.6 mrad. The 60-cm-long mirror subtends approximately 4.5 mrad horizontally and 0.33 mrad vertically with open premonochromator slits. The root-mean-square roughness of the mirror surface was measured to be 3-5 Å before and after coating with a Rh layer of 800 Å thickness. For a 6.6 mrad angle of incidence, the beam spot at the focal point has a diameter of 0.65 mm (FWHM). The intensity of 8 keV x-rays per mm^2 is about 10^{12} photon/s, three orders of magnitude higher than that of an unfocused beam.[52] The mirror also act as a filter to eject the high harmonic components of the monochromatized beam.

The hutch enclosing the experiments has personnel interlock to allow access to the equipment and samples and yet prevent exposure to the synchrotron radiation. The photon shutter prevents the x-ray beam from entering the experimental hutch unless the hutch is locked. For reflectivity and grazing angle EXAFS experiments, the sample is mounted on a high precision goniometer attached to a dedicated six-circle Huber 5020 diffractometer. The goniometer can be manually adjusted or motor controlled to translate the sample relative to the center of the diffractometer. The diffractometer is placed on a kinematic table which can be used to translate and rotate the diffractometer relative to the x-ray beam. The Huber

diffractometer allows the sample rotating about axis vertical to the diffraction plane (θ scan), inside the diffraction plane (χ scan) and normal to the sample surface (φ scan). The detector arm (at an angle 2θ to the direct beam) can be moved independently or coupled to the sample movement (θ-2θ scan). The angular movement is controlled by microstep motors with 0.0005°/step precision. A DOS based data acquisition software, EXASCAN,[55] is used to control the monochromator and the diffractometer through CAMAC interface. The system can also be operated with the SPEC/CPLOT[56], a commercially available software under UNIX.

Three types of x-ray detectors are used for reflectivity and fluorescence EXAFS experiment. They are ionization chamber, NaI scintillation counter and semiconductor detector. Ionization chambers are the oldest and most widely used. These detectors rely on the ability of gas (N_2, Ar) to produce ion pairs in response to the ionization radiation. Then, positive and negative ions can be separated in a electrostatic field and form the signal current through electrodes.[57] The detection efficiency of an ion chamber is determined by the active volume, the gas pressure and gas mixing. The ion chambers have the best performance when the signal rate is 10^5 to 10^{10} per second. For signal rates below 5×10^4 , the amplifier noise dominates, and pulse counting techniques are therefore preferred.[58] Ion chamber has no energy resolution. In x-ray reflectivity experiments, ion chambers are often used as beam monitors.

The scintillation counters and semiconductor detectors are based on pulse counting techniques. Detectors for which the fluorescence optical

radiation resulting from the x-ray absorption process is detected are called scintillation counters. The most widely used scintillating materials are alkali halide crystals such as sodium iodide. The scintillation layer is attached to the front end of the photomultiplier. The photomultiplier converts the fluorescence radiation to electrons and magnifies signals to a detectable level. NaI scintillation detectors have an energy resolution about 3000 eV at 10 keV, barely enough to resolve the harmonic frequencies from the fundamental of the synchrotron radiation. The scintillation lifetime is 270 ns, which limits the pulse pair resolution to about 700 ns. Therefore, scintillation counters lose their linearity when the signal rate is over 5×10^4 and get saturated for higher rates. Scintillation counters are used as scattering signal detectors due to their high sensitivity and compact size.

The semiconductor detector is the solid state analog of the ionization counter. The charge carriers are now electrons and holes rather than electrons and ions, and the ionization potential is the energy required to produce electron-hole pairs, which is 2.97 eV for germanium and 3.73 for silicon at 78 K. Semiconductor detectors have shorter dead times (typically 10 ns) and better energy resolution (typically 200 eV at 10 keV) than scintillation counters.[56] The semiconductor detector must be maintained at low temperature: 78 K for germanium detectors, and is very sensitive to the environmental noises. An intrinsic germanium detector is used to measure the x-ray fluorescence in surface EXAFS experiments.

3.2 X-ray reflectivity experiment

The experiment setup and procedures discussed in this section are based on our research practices and studies of the experimental methodology. Some similar or somewhat different procedures of doing the reflectivity measurements can be found in the literature.[59]

Experimental setup

Fig.3.4 shows the optical setup for x-ray reflectivity measurements. The monochromatized and focused x-ray beam entering the experimental hutch is first monitored by an ion chamber. The ion chamber count (I_{oo}) is an indicator of the fine tuning state of the monochromator. It is also used as the feed back signal in the monochromator stabilizing system. The beam is then defined by a motorized slit (Slit 1) both vertically and horizontally. The incident beam size (horizontal size w and vertical size d) is very important in the reflectivity measurements. We will show later how the beam size and the detector slit aperture are related to the angular resolution. A NaI scintillation detector (NaI det. 1) is placed perpendicularly to the beam to monitor the incident beam intensity. The air scattering signal collected by the NaI det. 1 in this configuration is proportional to the beam intensity. The reduction factor is about 10^{-6} for 8 keV beam. The beam then hits the sample and is reflected. Slit 2, slit 3 and the NaI det. 2 are mounted on the 2θ arm and moved in the reflection plane to the direction of the reflected beam. The purpose of slit 2 is to cut down any scattering not

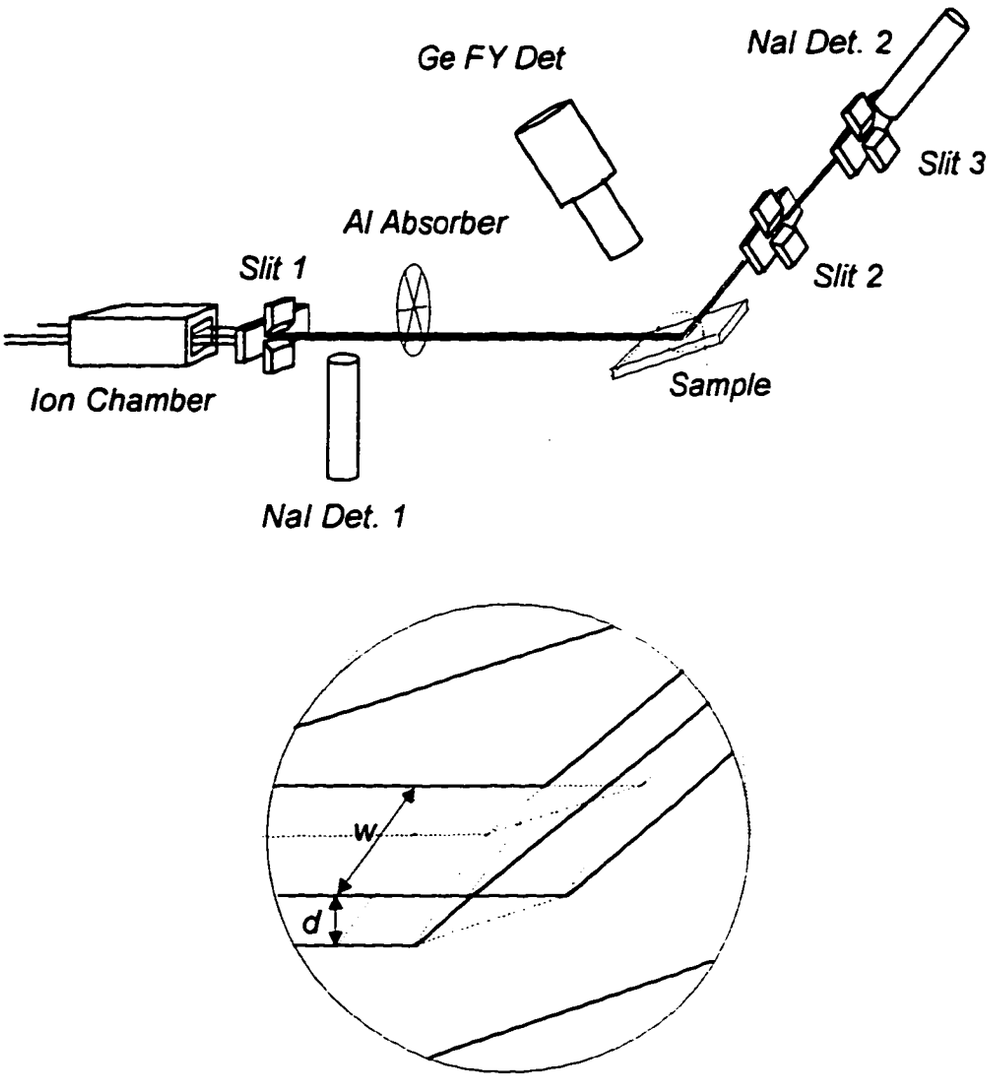

Fig. 3.4 The optical setup for the reflectivity and fluorescence measurements.

originating in the sample. Slit 3 is placed before NaI det. 2 and is set wide enough to accept all the specularly reflected scattering. To ensure the best resolution possible and accurate alignment, the aperture of slit 3 has to be close to that of slit 1 but a lit bit wider. The actual size of the slit 3 aperture depends on the beam condition (e.g. focused or partially focused) and the sample property (e.g. Thick, thin or multilayer). Usually trial and error procedure is need to achieve the best resolution. The NaI Det. 2 can be placed perpendicularly or parallel to the beam, depending on the intensity of the reflected beam. A typical reflectivity spectrum can be measured with synchrotron x-ray down to $\sim 10^{-8}$ while the up limit of the NaI detector count rate is 5×10^{4}. For this reason, a set of calibrated aluminum absorbers is used to reduce the beam intensity reaching the detector. For fluorescence and grazing angle EXAFS measurements, a semiconductor Ge detector can be placed above the sample or side wise. To reduce the intensity lose due to air scattering , vacuum pipes are used to enclose the x-ray beam pass (not shown in the figure). Fig. 3.5 shows the electronic setup for reflectivity and fluorescence EXAFS measurements. The photon signals collected by the two scintillation counters are transferred to the data acquisition program running on the PC through single channel amplifiers. The energy spectrum of the fluorescence yield detected by the Ge detector can be displayed on a multi-channel analyzer and the fluorescence intensity of specific photo emission lines can be selected by setting the energy window of the single channel amplifier.

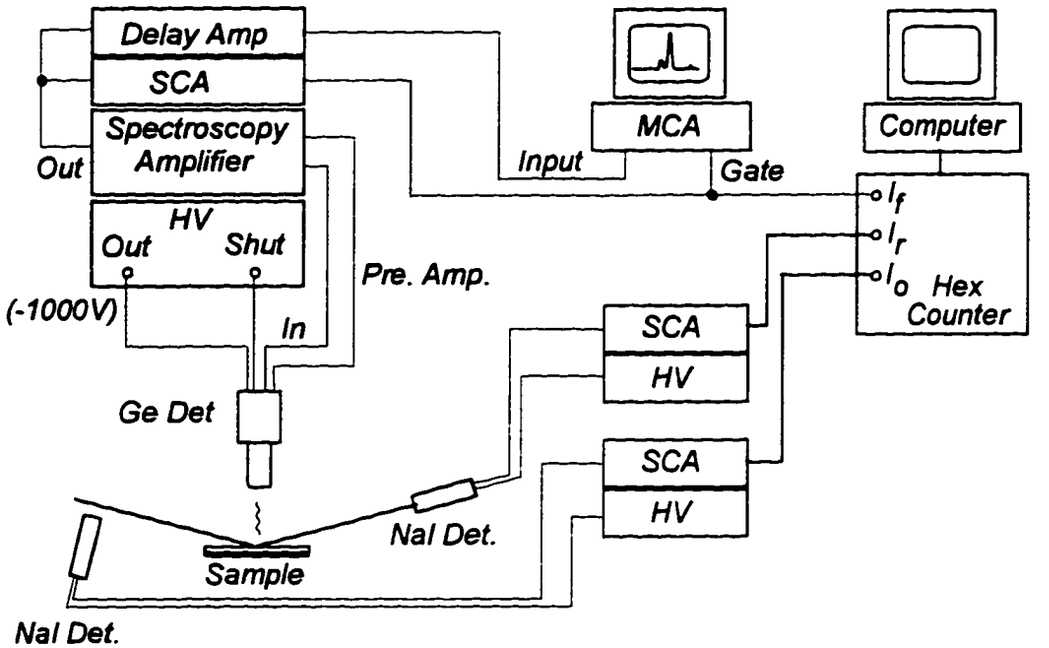

Fig. 3.5 Electronic setup for the reflectivity and fluorescence EXAFS experiments.

The choice of slits

The resolution function of the spectrometer for the reflectivity measurement is defined as the curve obtained by 2θ scan of the detector crossing the direct beam. If the beam after slit 1 has an uniformly distributed step function form, the resolution function will assume a shape as shown in Fig.3.6(a). It can be written as:

$$I(2\theta) = I_0 B(\alpha_b, 2\theta) \otimes D(\alpha_d, 2\theta) \tag{3.3}$$

where B and D are step functions with vertical angular width α_b and α_d for the direct beam and the detector slit (slit 3), respectively. ⊗ denotes the convolution. I_0 is the direct-beam intensity. The α_b and α_d are related to the vertical size of the slits, d_1 and d_3, by:

$$\begin{aligned} \alpha_b &= \delta\theta_0 + d_1 / L \\ \alpha_d &= d_3 / L \end{aligned} \tag{3.4}$$

where L is the length of the 2θ arm (from the center of 2θ rotation to slit 3), $\delta\theta_0$ is the angular spread of the synchrotron beam. A similar function can be defined in the horizontal direction. However, the horizontal resolution function is not as critical as the vertical one since the out-of-plane scattering is small in the reflectivity geometry. The best resolution will be achieved if $\alpha_b = \alpha_d$. In this case, the resolution function will be a triangular function instead of a trapezoid as shown in Fig.3.6(a). However, this ideal condition is in general impractical due to the non perfect sample

condition and alignment error. Usually α_d is set to be about twice of α_b. In practice, especially for a focused beam, the direct beam is often not uniformly distributed and is then better described by a Gaussian function than a step function. As a result, a 2θ scan of the detector crossing the direct beam usually deviates from a trapezoid function and has tails that decrease relatively smoothly to zero. In these case, α_b can be defined as the full width at half-maximum (FWHM) of the beam profile. Fig. 3.6(b) shows a typical resolution function in our reflectivity measurements. It is worth to note that the derivative of the resolution function will give the direct beam profile function (as shown in Fig. 3.6 (c)) since,

$$\begin{aligned}\frac{dI(\omega)}{d\omega} &= I_0 \int_{-\infty}^{\infty} B(\omega') \frac{dD(\omega-\omega')}{d\omega} d\omega' \\ &= I_0 \int_{-\infty}^{\infty} B(\omega')(\delta(\omega-\omega'-\alpha_d/2)-\delta(\omega-\omega'+\alpha_d/2))d\omega' \\ &= I_0(B(\omega-\alpha_d/2)-B(\omega+\alpha_d/2))\end{aligned} \qquad (3.5)$$

where $\omega=2\theta$.

For further discussion, we define the angular acceptance of the detector, $\delta\theta$, as the FWHM of the resolution function. Note that $\delta\theta$ depends on both the beam profile and the vertical angular width α_d of the detector slit.

It is illuminating to explain the relation between the resolution of the spectrometer and the angular acceptance $\delta\theta$ of the detector as well as the angular spread of the incident beam $\delta\theta_0$ in terms of the resolution volume

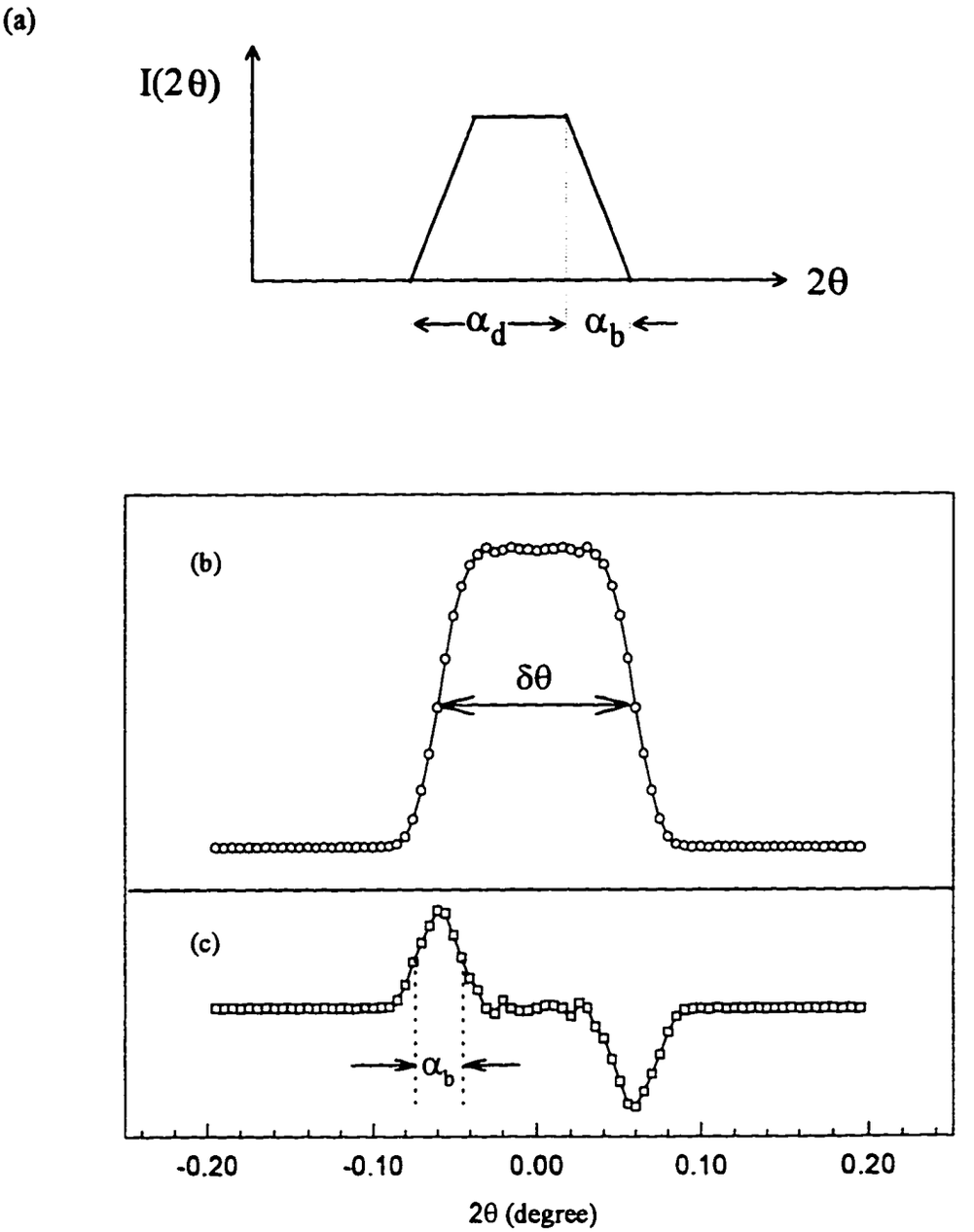

Fig. 3.6 Resolution function of the spectrometer, (a) for step function beam profile, (b) a real case, (c) derivative of (b). The derivative of the resolution function gives the beam profile (cf. Eq. 3.5).

in reciprocal space. Fig.3.7(a) defines the momentum transfer **Q**. It's components in the Y-Z plane (the scattering plane) can be written as:

$$\begin{aligned} Q_z &= k_0(\sin\theta + \sin\theta_0) \\ Q_y &= k_0(\cos\theta - \cos\theta_0) \end{aligned} \tag{3.6}$$

The θ and θ_0 are glancing angle of incident and scattered beam respectively. Note that $2\theta = \theta + \theta_0$.

The uncertainties in Q_z and Q_y are given by:

$$\begin{aligned} \Delta Q_z &= k_0(\delta\theta + \delta\theta_0) \\ \Delta Q_y &= k_0(-\theta\delta\theta + \theta_0\delta\theta_0) \end{aligned} \tag{3.8}$$

at small angles. From (3.8) the resolution volume can be defined by the two inequalities:

$$\begin{aligned} \left|\theta_0\Delta Q_z - \Delta Q_y\right| &< \frac{1}{2}k_0(\theta + \theta_0)|\delta\theta| \\ \left|\theta\Delta Q_z + \Delta Q_y\right| &< \frac{1}{2}k_0(\theta + \theta_0)|\delta\theta_0| \end{aligned} \tag{3.9}$$

The area enclosed by the two inequalities is the resolution volume of a two-slit spectrometer. The scattered x-radiation accepted by the detector is actually the integrated intensity over the resolution volume. Fig. 3.7 (b) shows the resolution volume in the reciprocal space. As can be seen from Fig 3.7 (b), the resolution on Q_z axis is mainly determined by $\delta\theta_0$ and the resolution on Q_y axis by $\delta\theta$. For a perfectly smooth sample with no diffused scattering, all the reflected intensity is distributed on the Q_z axis, and the only limit to the resolution is $\delta\theta_0$. In this case, only the beam width d_1 is important since it determines $\delta\theta_0$ (cf. Fig. 3.2). In practice, there are always diffused scattering in reflectivity measurements, and the resolution on Q_y

(a)

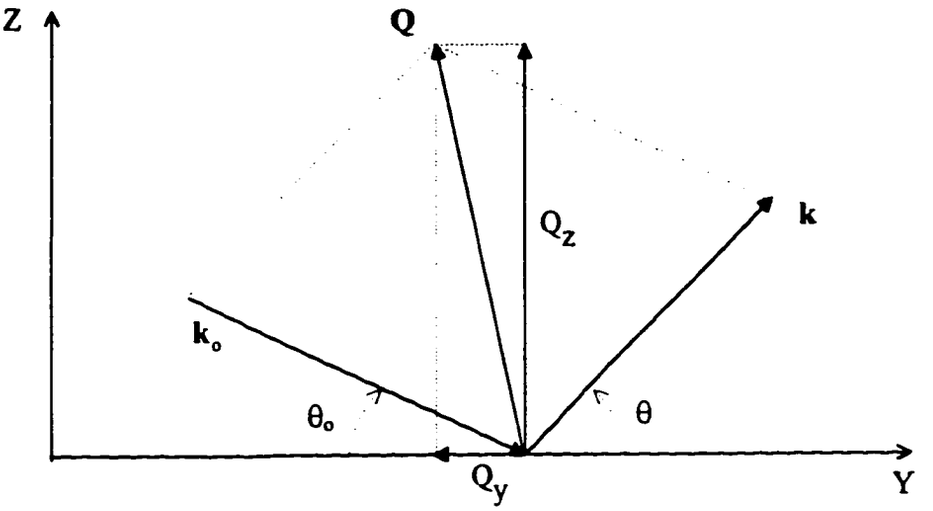

(b)

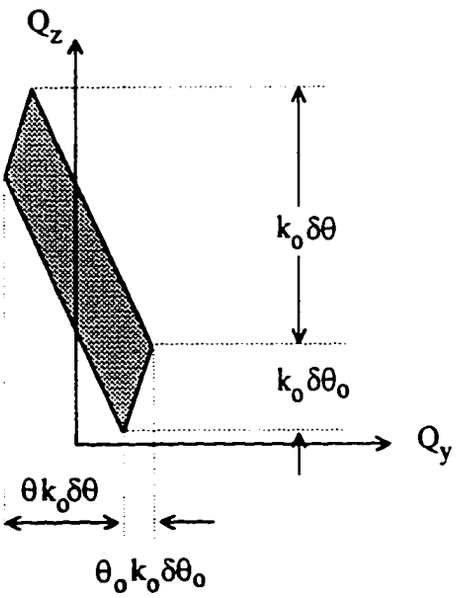

Fig.3.7 Scattering kinematics of reflectivity experiments. (a) Definition of scattering vectors, (b) resulution volume in reciprocal space.

axis is important. The diffused scattering intensity is not uniformly distributed in Q-space. It is more widely spread around the maximum of specular intensity (e.g. Bragg peaks). Because of the tilted orientation of the resolution volume, it might pick up the diffused intensity from a range of Q_z values and thus smear the reflectivity curves if the $\delta\theta$ is not correctly set. Fig.3.8 shows how a too wide detector slit opening can cause bad resolution. Fig. 3.9 compares two reflectivity curves measured with different resolution functions.

In principle, the smaller the resolution volume the better the angular resolution. The vertical width of the beam defining slit (d_1) is the most critical parameter since it controls both $\delta\theta_0$ and $\delta\theta$ (remember d_3 must be greater than d_1). However, a too small d_1 will cause difficulties in sample alignment and reduce the incident beam intensity. In our experiments, we found that a 0.1 to 0.3 mm beam defining slit is adequate for most samples. The detector slit is set accordingly to have α_d about twice of α_b. This will result in an angular acceptance ($\delta\theta$) of about 0.1°(cf. Fig.3.6(b)). The horizontal opening of the beam defining slit is usually set to 1 to 5 mm, according to the sample and beam conditions.

Sample Alignment

After correctly setting of the slits, the next step is to align the sample. The object of sample alignment is to align the center of the 2θ arm rotation, the sample surface and the beam center to one point. The alignment

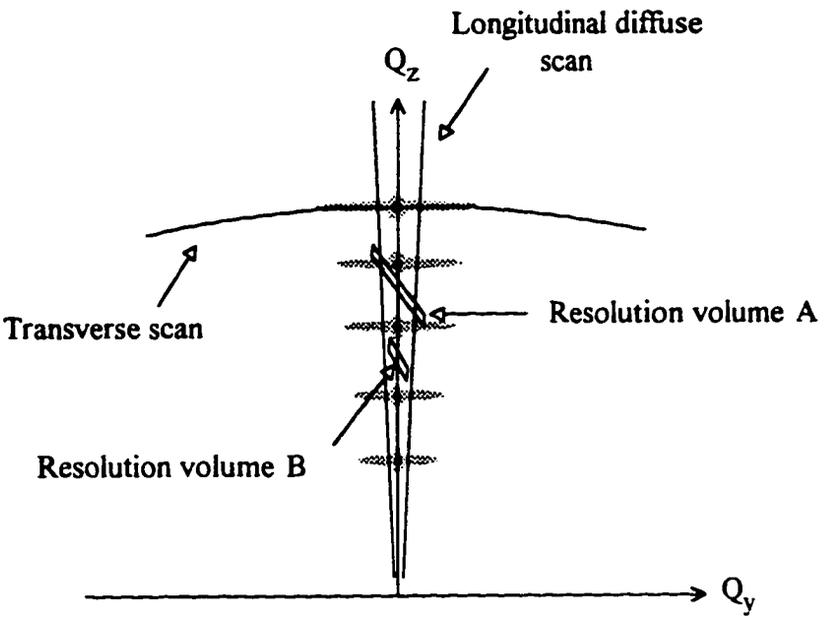

Fig. 3.8 Schematic representation of different resolution volumes in the eciprocal space. Resolution volume A will collect too much diffuse scattering in a specular θ-2θ scan (along Q_Z axis). Resolution volume B is dequate for this intensity pattern. Also shown in this figure are the representations of transverse diffuse scan (θ scan with the detector fixed at a certain angle (2θ) and the longitudinal diffused scan (θ-2θ scan with a fixed offset). The longitudinal diffused scan gives the background diffuse scattering contribution.

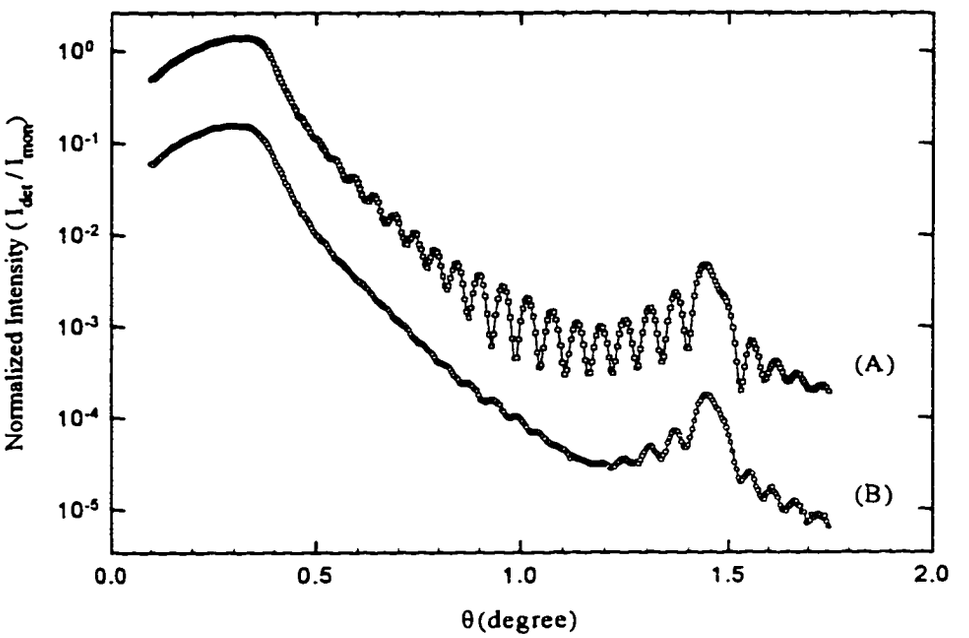

Fig. 3.9 Reflectivity curves measured with different resolution functions. (A) $\alpha_d = 0.03°$, $\alpha_b = 0.02°$, (B) $\alpha_d = 0.1°$, $\alpha_b = 0.02°$. I_{det} represents the detector counts and I_{mon} the monitor counts. Note that these are raw data curves without geometrical correction.

between the 2θ arm center and the beam center is accomplished by translating the diffractometer table in the two directions perpendicular to the beam. Then with both the beam monitor (I_{mon}) and scattering detector (I_{det}) perpendicular to the beam, a 2θ scan crossing the direct beam can be done. The data collected from this scan, I_{det}/I_{mon} vs. 2θ angles, is the resolution function of the normalized beam (cf. fig.3.6). In the following text, by the beam intensity or scattered intensity, we always refer to the normalized intensity as:

$$I(\theta) = I_{det}(\theta) / I_{mon} \tag{3.10}$$

This is to compensate the time fluctuation of the synchrotron radiation during the scans. The middle point of the flat top of the resolution function is then designated as zero point of 2θ. The value of I_{det}/I_{mon} at $2\theta = 0$ is recorded as direct beam intensity and will be used later to calculate the absolute reflectivity.

With the detector sitting at zero point of 2θ, the sample is then translated into the beam by adjusting the goniometer until half of the direct beam intensity is blocked. The parallelism of the sample surface with the direct beam is ensured by rotating the sample about θ scan axis. This scan, named as zero point θ scan, will result in a curve with triangular line shape. The apex of the triangle is then designated as zero point of θ. If the maximum value of the scan is not half of the direct beam intensity, the goniometer has to be adjusted again to raise or lower the sample until half-intensity blocking is reached. Fig. 3.10 shows an example of the zero point θ scan curve. The triangle line shape should be symmetric about the zero

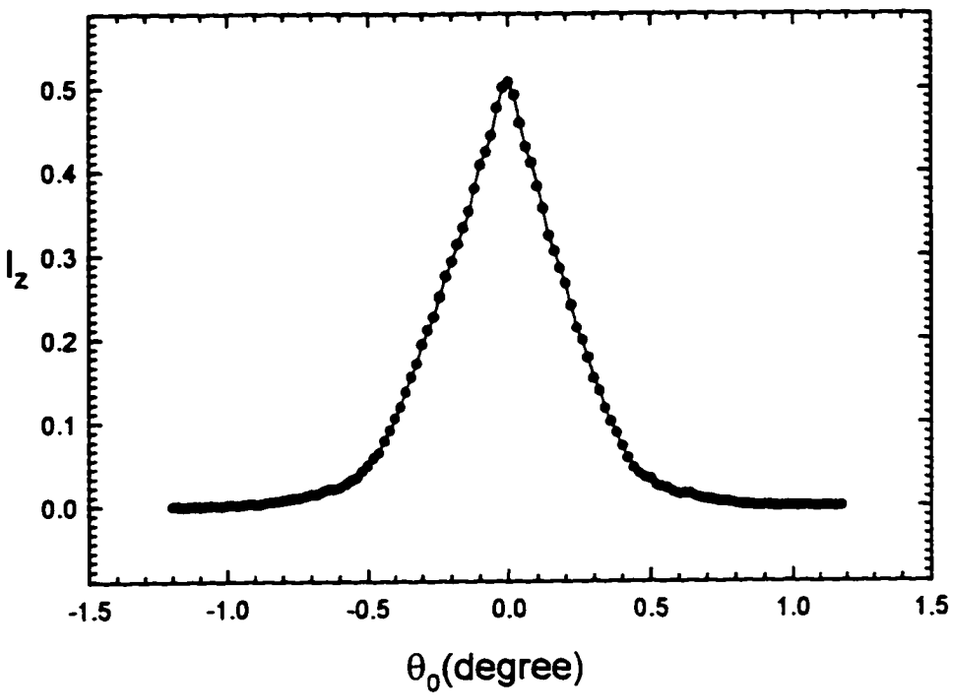

Fig. 3.10 An example of the zero point θ-scan curve. I_Z is normalized intensity.

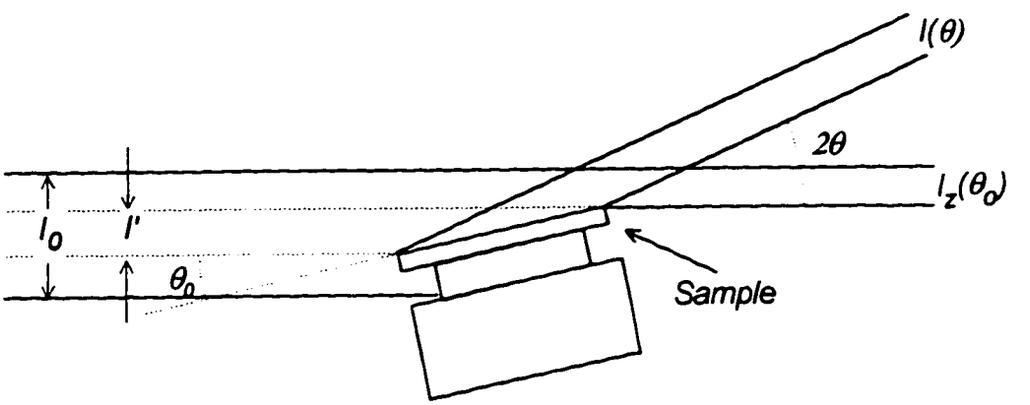

Fig. 3.11 Diagram of the beam split for incident angles less than the full interception angle.

point of θ. A non symmetric triangle means that the beam does not hit on the center of the sample in the direction parallel to the beam. In this case the goniometer has to be adjusted to translate the sample in the beam direction, and above procedure must be repeated to ensure best θ alignment. The final zero point θ scan curve will be used in determination of the geometrical factor for correction on small angle reflectivity data. We will discuss this point later.

Once this procedure has been carefully followed, the sample is in principle ready for reflectivity measurements. However, it is worth checking the alignment by θ scan with higher 2θ angles, for example at the critical angle of total reflection or/and Bragg peaks of multilayers. Any missetting of the sample is then easily discovered if the sharp specular peak does not sit at the θ angle of exactly half of the fixed 2θ angle (cf. fig. 3.13). Usually the missetting , if any, is very small (e.g. 0.005°) and can be corrected by recalibrating the θ angle.

Data collection, correction and analysis

The specular reflectivity is measured by θ-2θ coupled scans. In a θ-2θ scan the detector and the sample rotate simultaneously and the moving step of the detector is kept to be twice of the sample. Since the incident angle θ_0 and scattering angle θ are equal, the Q_y in (3.6) is zero and the scan viewed in Q-space is along the Q_z axis. To avoid saturation of the detector,

different aluminum absorbers are inserted in the beam to attenuate the intensity at different angular regions. A completed continuous reflectivity curve can be obtained by connecting the segments of the curve measured with different absorbers. The shifting constants needed for doing this can be obtained from the overlapped parts of the segments. The absolute reflectivity is obtained, if all the beam is intercepted by the sample, by dividing by the direct beam intensity.

For small angles, the beam is not fully intercepted by the sample (cf. Fig. 3.11). In this case, only part of the incident beam hits on the sample and a geometrical correction is needed to get the absolute reflectivity. The part of the beam intensity intercepted by the sample, $I_0'(\theta_0)$ can be derived from the zero point θ-scan function $I_z(\theta_0)$:

$$I_0'(\theta_0) = I_0 - 2I_z(\theta_0) \tag{3.11}$$

For $\theta_0 > 0$. See Fig. 3.11. We assume here that the beam profile is symmetric about it's center and the sample is symmetric about it's axis. The corrected absolute reflectivity is given by:

$$R = I(\theta_0) / I_0'(\theta_0) \tag{3.12}$$

For θ_0 greater than the full interception angle, $I_0'(\theta_0) \rightarrow I_0$, so (3.12) is valid for all angles except $\theta_0 = 0$ since the $I_0'(\theta_0) = 0$ there. Actually, for incident angles less than $\delta\theta/2$, part of the direct beam intensity will be collected by the detector during the specular reflectivity scan. This part of

the curve is not important in the analysis of the data and is simply discarded. Fig. 3.12 shows an example of the geometric correction for small angle data.

Another applicable correction is the subtraction of the diffuse background scattering from the raw data curves. Because of the finite resolution of the spectrometer, part of the diffuse scattering background may be included into the detected specular intensity. When the diffuse scattering contribution is comparable to the specular component, it has to be subtracted from the raw data to get the true specular reflectivity. For doing this, two kinds of scan related to diffuse scattering are needed: the transverse scan and the longitudinal diffuse scan. Fig.3.8 shows the loci of these scans in Q-space. Transverse scans are carried out by rotating the sample (θ-scan) while keeping the detector fixed at a certain angle (2θ). The intensity curve from a transverse scan is composed of a sharp specular peak and a slow varying diffuse scattering background. The amount of diffuse scattering to be subtracted is determined by the longitudinal diffuse scans. In a longitudinal diffuse scan the sample is offset from the specular condition by a small and fixed angle δ. The offset δ can be set to both sides of the specular peak (see fig. 3.13). To get the best estimate of the diffuse scattering contribution, the offset angle should be as small as possible but without collecting any specular intensity. The true specular reflectivity is then given by:

$$R(\theta) = (I(\theta) - I_s(\theta)) / I_0 \qquad (3.13)$$

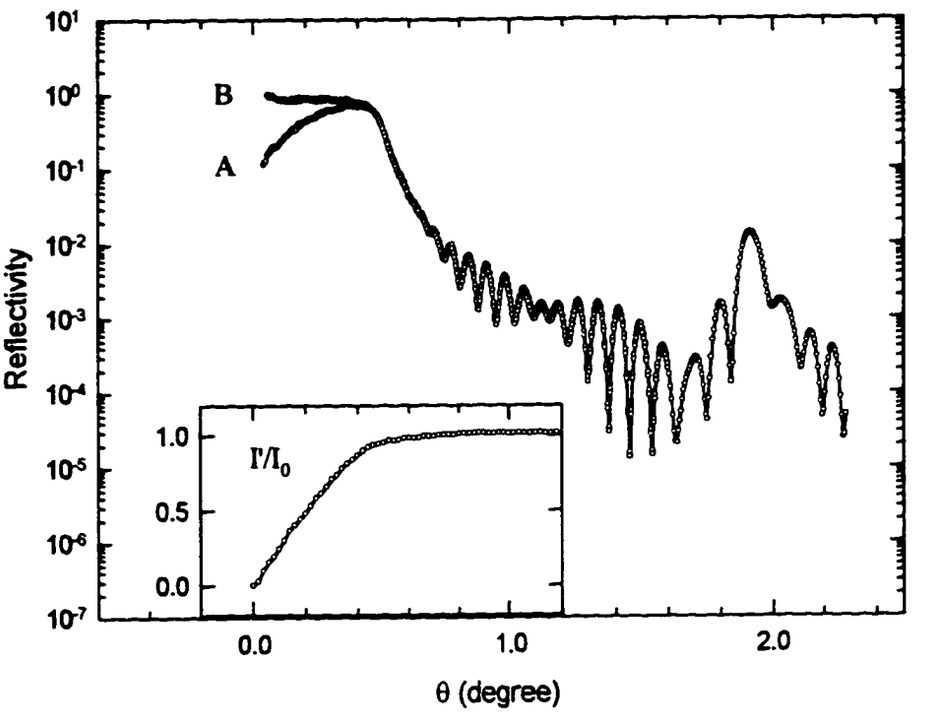

Fig. 3.12 The geometrical correction for small angle data. Curve A is the data before the correction, B the data after the correction. The insert shows the ratio between the intercepted intensity I' and the direct beam intensity I_0.

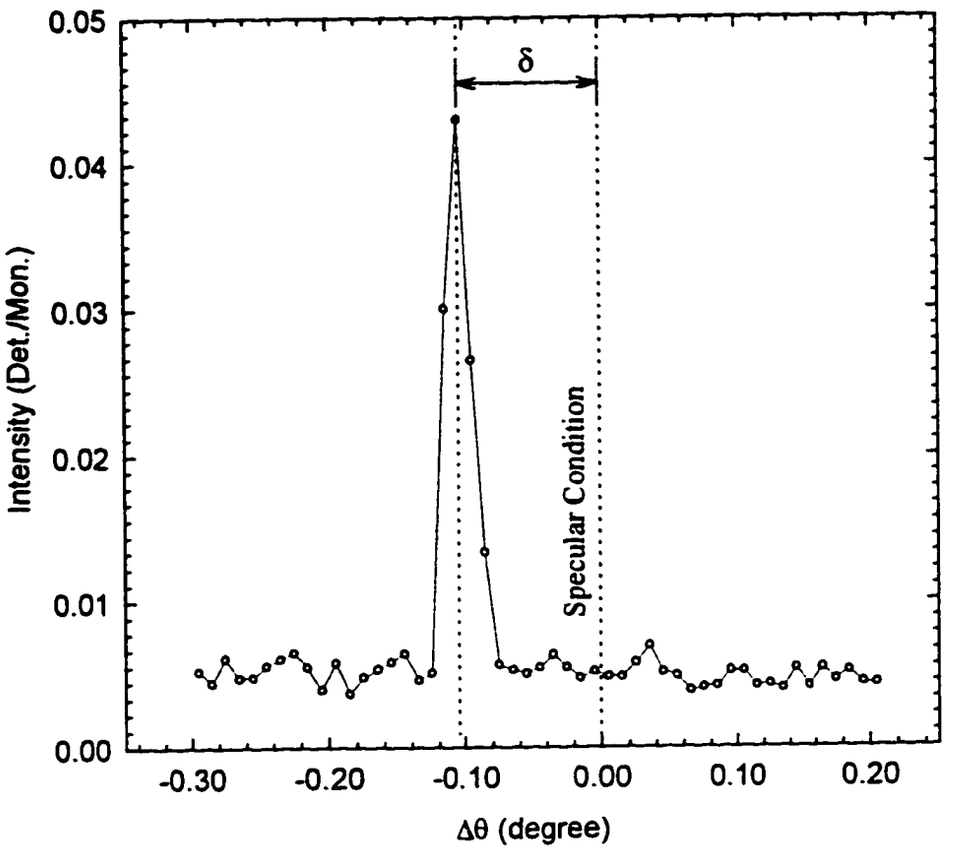

Fig. 3.13 A transverse scan with 2θ fixed at 10.39°. Δθ is relative to the specular condition. In this scan the sample is offset to the specular condition by an δ about 0.1°.

Where $I_\delta(\theta)$ is the longitudinal diffuse scattering intensity collected with an offset δ from the specular ridge. The diffuse scattering level relative to the specular peak is a test of the adequacy of the spectrometer resolution. If the diffuse scattering level is too high, one should first try resetting the slits to reduce the resolution volume. For the reflectivity data used in this thesis, the diffuse scattering level is at most less than 10% of the total intensity. Fig. 3.14 shows an example of diffuse scattering correction.

The object of the reflectivity measurement is to derive the structural parameters from the measured reflectivity curves. Reflectivity data analysis is actually a process of nonlinear least-squares curve-fitting of the model calculation to the experimental data. That is, to find out the parameters that minimize the least-squares sum:

$$\chi^2 = \sum_i \left(\frac{\log_{10}(R_i^{observed}) - \log_{10}(R_i^{calculated})}{\Delta R_i} \right)^2 \qquad (3.14)$$

Where ΔR_i is the standard deviation of the experimental data at θ-angle of step i. It is proportional to the inverse square-root of the count number at that angle. In the next two chapters the analysis of the reflectivity data will be given.

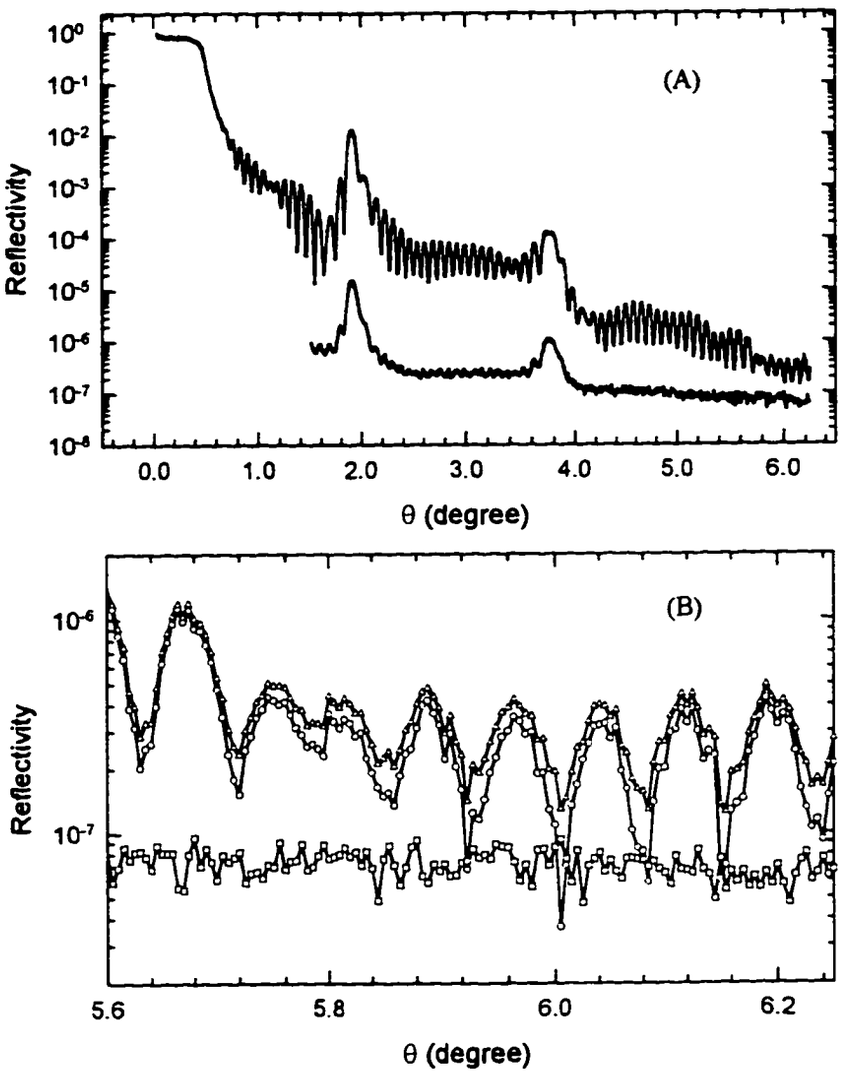

Fig. 3.14 Diffuse scattering subtraction. (A) shows the diffuse scattering level in comparison to the reflectivity data before correction. The offset for the diffuse scattering scan is 0.1°. (B) shows in details the reflectivity data before correction (triangles), after correction (circles) and the diffuse scattering intensity (squares). The data is taken from a Cr/Fe multilayer with an x-ray beam of 6.1 keV.

CHAPTER 4 RESONANT X-RAY REFLECTIVITY STUDY OF A NI/FE ALLOY THIN FILM [60]

4.1 Introduction

Permalloy thin films ($Fe_{0.2}$ $Ni_{0.8}$) have been used extensively as high-density magnetic recording material. Because of its many desirable properties, permalloy is an excellent choice of material for recording head devices and composite anisotropy recording medium.[61] These properties include low coercivity, low crystalline anisotropy, high magnetization, high permeability, small magnetostriction and relatively large magnetoresistive coefficient. The corrosion resistance of a permalloy thin film is of prime technological interest. The formation of passive thin films on pure metals has been the subject of extensive studies.[62,63,64,65,66,67,68] In recent years only a relatively small number of investigations have dealt with the passivation and corrosion of Ni/Fe alloys.[69,70,71] In the present work we report resonant x-ray reflectivity measurements on a thin film permalloy ($Fe_{0.2}$ $Ni_{0.8}$).

The sample were prepared at IBM, Almaden (P. Melz and H. Lee, San Jose, CA, USA). The Ni/Fe sample was sputtered in a Perkin-Elmer 2400 sputtering system. The Argon pressure was 12 milli-torr, and the system power was 500 W. The target was 8 inches in diameter with the composition close to 80% Ni (balance iron). The Ni/Fe alloy ($Fe_{0.2}$ $Ni_{0.8}$) was sputtered on 5 cm by 5 cm float glass substrate. The reflectivity measurements were conducted on beam line X6B at the National

Synchrotron Light Source at BNL. The x-ray energies used in the measurements were (cf. Fig. 2.1) 7.0 keV (below the Fe and Ni K-edges), 7.112 keV (Fe K-edge), 7.5 keV (above the Fe K-edge but below the Ni K-edge), 8.333 keV (Ni K-edge) and 9.0 keV (above the Ni K-edge). The experimental setup and the alignment procedure have been described in Chapter 3. In complement to the reflectivity measurements, we also measured x-ray absorption fine structure (XAFS) of the sample by scanning fluorescence yield at grazing incidence. The XAFS results will be listed as appendix A of this thesis.

In our composition analysis we use a series of straight line segments to approach the in depth electron density profile. In our model, the electron density is a continuous function everywhere in the medium. Within each segment, the differential equation (2.40) can be solved analytically. The wave functions are related to Hankel functions $H_{1/3}^{(1)}$ and $H_{1/3}^{(2)}$. We then apply the boundary conditions at the joint points of the line segments and derive the amplitude coefficients of $H_{1/3}^{(1)}$ and $H_{1/3}^{(2)}$. From these coefficients the reflectivity is calculated. A Gaussian factor is added to our final result to account for the reduction in specular reflected intensity due to nonspecular (diffuse) scattering. The separation between the rms roughness that appears in the Gaussian factor and the intrinsic width of the interface is only nominal. As we indicated in chapter 2, a rough and a graded interface are indistinguishable under specular reflectivity conditions. A detail description of the matrix formalism has been given in chapter 2.

In following paragraphs we will present the results of our measurements and discuss in detail the specific analysis model for this thin film sample and the information derived from the fitting parameters.

4.2 Results and Discussion

Fig. 4.1 shows the resonant reflectivity measurements. The diffuse off-specular contribution is subtracted before fitting the data. In the measured Q_z region the diffuse scattering background is significantly smaller than the specular reflectivity (less than 1/100). Fig. 4.2 to Fig. 4.6 show the normalized reflectivity spectrum R/R_0 and the model fits plotted in linear scale. R_0 is Fresnel reflectivity from a semi-infinite uniform Ni/Fe alloy (c.f. Eq. 2.21, with $\sigma = 0$). The linear scale plotting displays the dispersion behaviors of the reflectivity curves more clearly. The purpose of the R_0 normalization is to emphasize the interference fringes at higher photon wave vector transfer Q_z. The data curves at different x-ray energies exhibit strong energy dependent effects. This can be seen from the curve variation near the critical angle and the changes in the shape of the oscillations envelope. This differences are due to the energy dependence of the effective electron densities and linear absorption coefficients, or f' and f''. Each element in the sample responds differently to the x-ray energy variations while the total energy dependent effective electron densities and linear absorption coefficients are simply the sum of those of the alloy components, weighted by their atomic weight percentages. In other words,

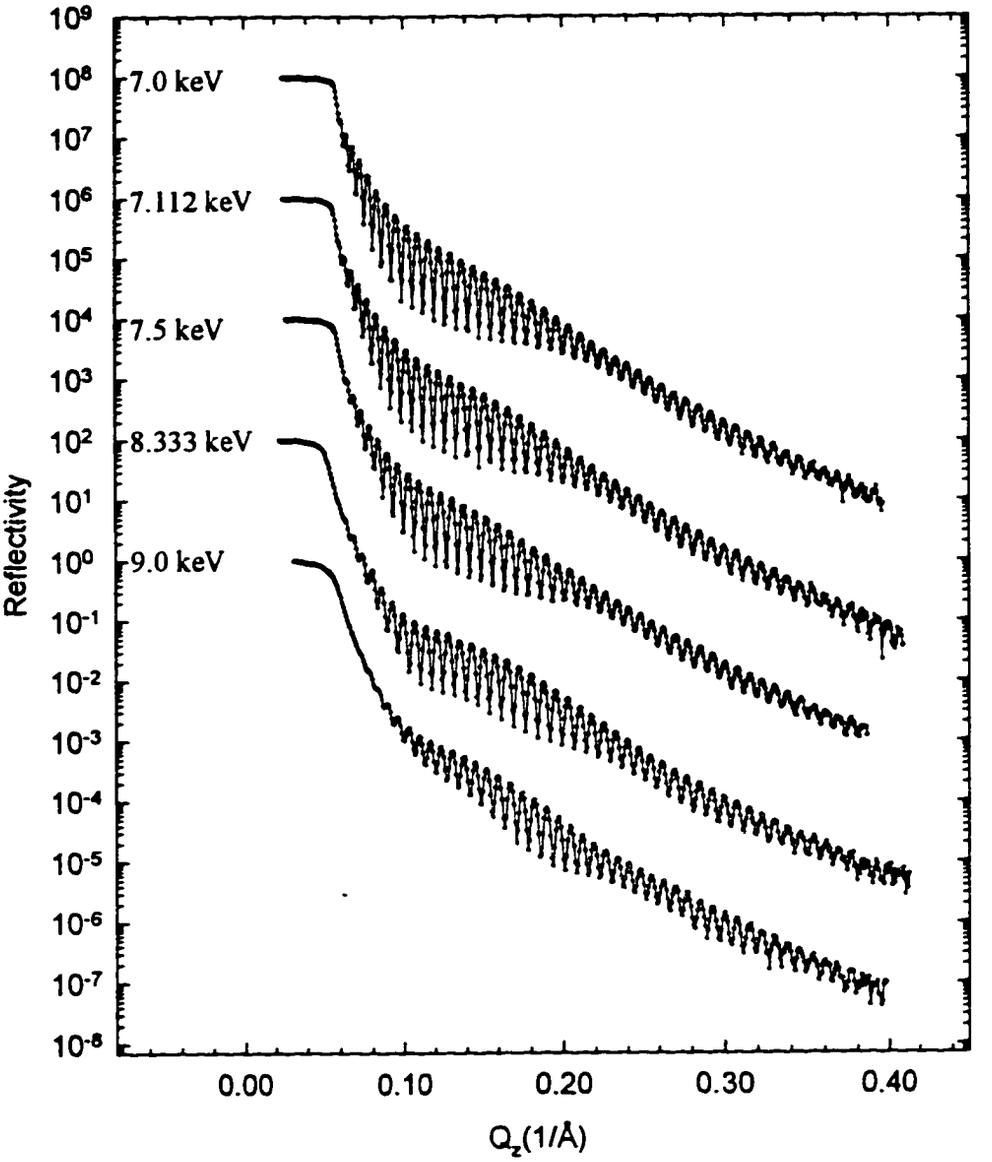

Fig. 4.1 Resonant reflectivity measurements on Ni/Fe the thin film sample. The lines are eye guides only. The x-ray energies used for the reflectivity measurements are marked on the left of the curves.

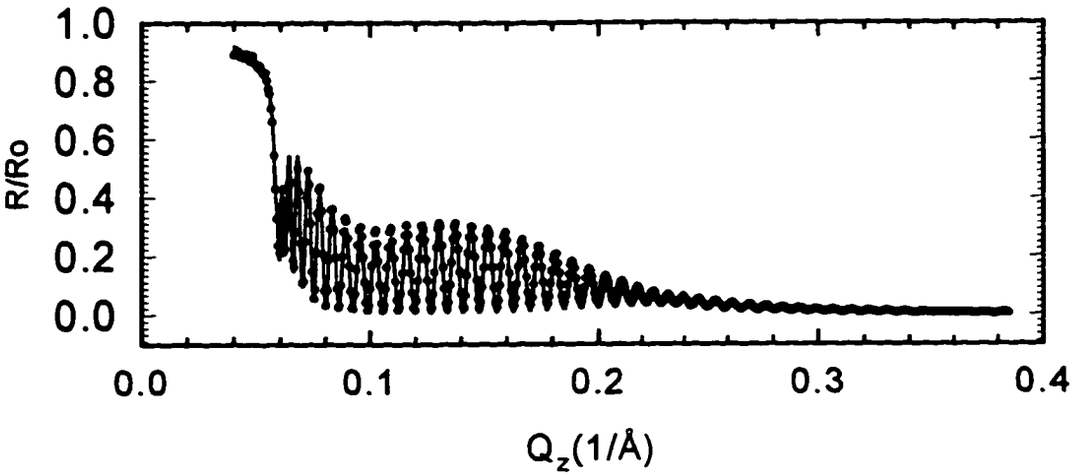

Fig. 4.2 Normalized reflectivity data (circles) and the model fits (line) for the Ni/Fe thin film at E = 7.0 keV.

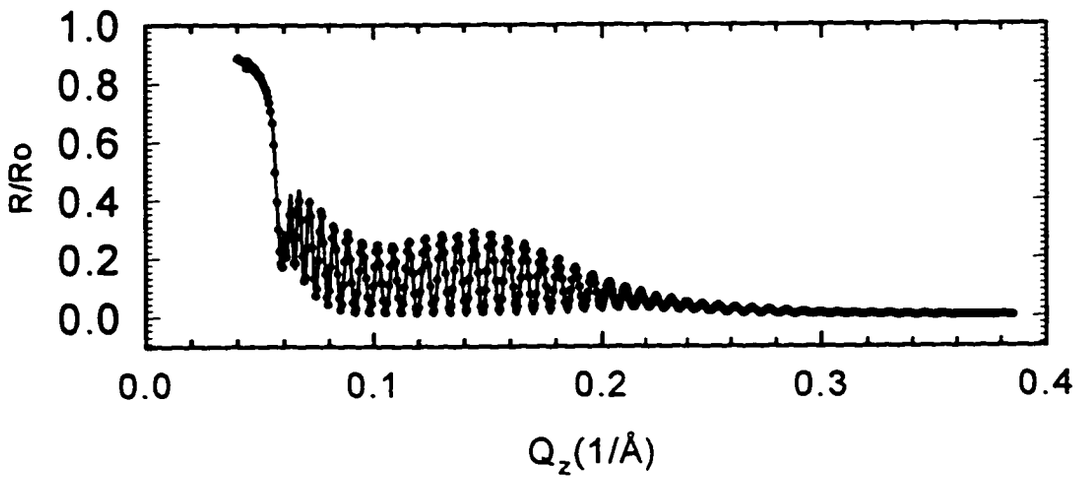

Fig. 4.3 Normalized reflectivity data (circles) and the model fits (line) for the Ni/Fe thin film at E = 7.112 keV.

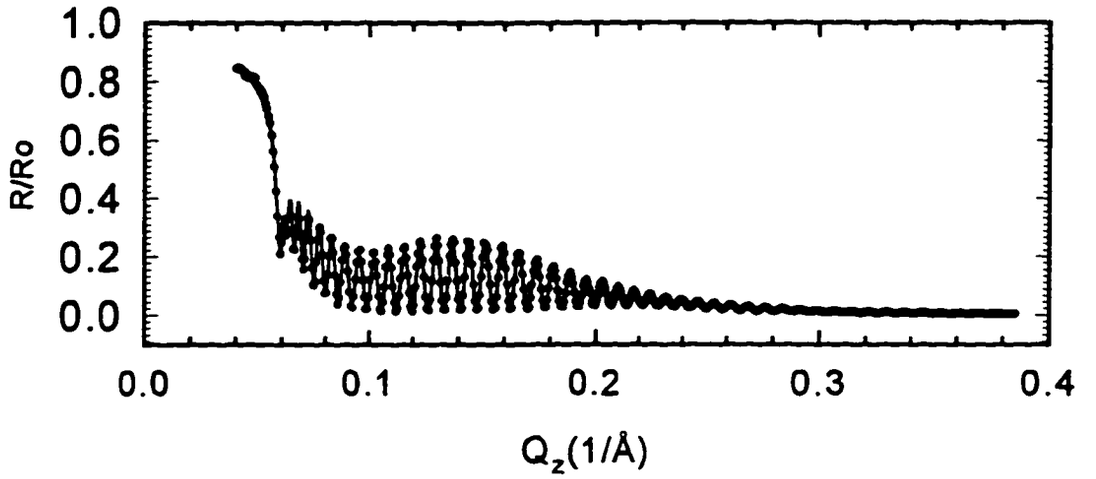

Fig. 4.4 Normalized reflectivity data (circles) and the model fits (line) for the Ni/Fe thin film at E = 7.5 keV.

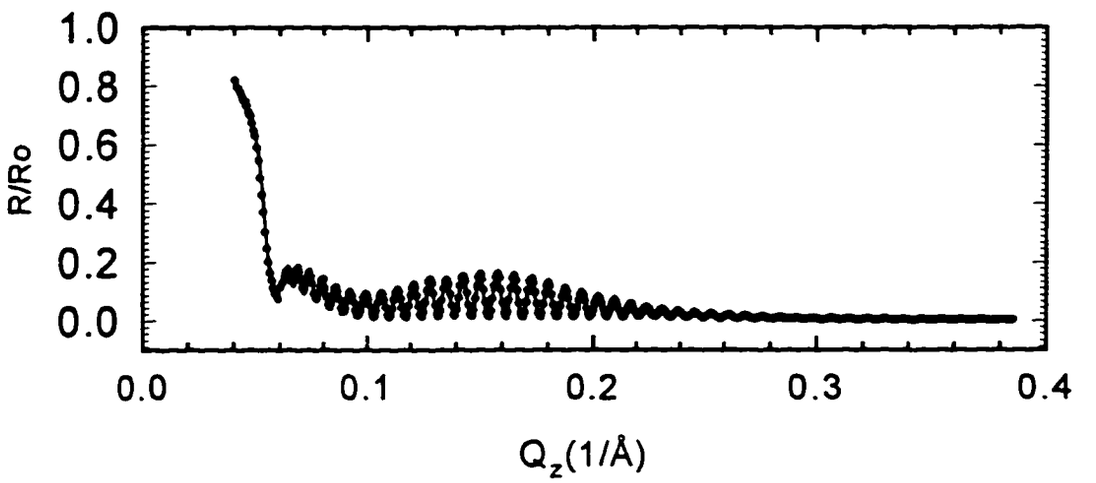

Fig. 4.5 Normalized reflectivity data (circles) and the model fits (line) for the Ni/Fe thin film at E = 8.333 keV.

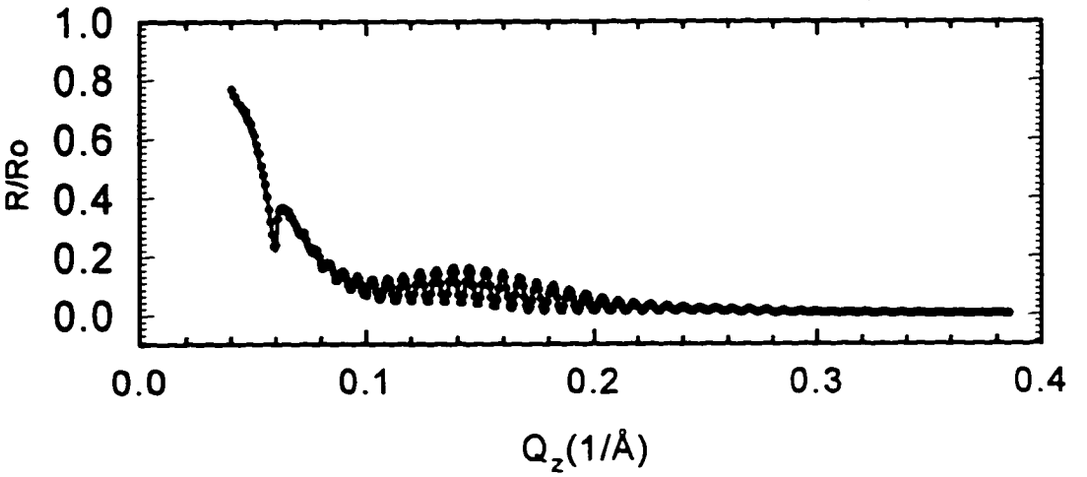

Fig. 4.6 Normalized reflectivity data (circles) and the model fits (line) for the Ni/Fe thin film at E = 8.0 keV.

given weight percentage of each element in the alloy, we can calculate the effective electron densities and linear absorption coefficients at the various energies. So with a single group of composition and geometry parameters (discussed later), we calculated the reflectivity and fit it to the experimental data curves at all five different energies, thus deriving the composition profile of the alloy thin film. The resonant effect near the K-edge of Fe and Ni gives a strong element sensitivity. This allows a more unequivocal analysis of the reflectivity measurement.

Fig. 4.7 is the schematic diagram of our fitting model. The geometry parameters are defined in table 4.1. While the composition parameters are closely related to the shape of the oscillations envelope, the geometry parameters are linked to the periods of the oscillations. It is well known that the period of the interference fringes in the small angle reflectivity is not a constant.[72] For a simple thin layer with ideal interfaces, the variation is given by a modified Bragg equation:

$$\Delta\theta_m = \theta_{m+1} - \theta_m \approx \frac{\lambda}{2d}\sqrt{1-\frac{2\delta}{\theta_m^2}} \qquad (4.1)$$

With θ_m the mth maximum of the interference fringes and d the thickness of the thin layer. δ is defined in (2.8). (4.1) is derived under the condition that $\lambda << 2d$. However, in a real layered structure with non-ideal interfaces, the situation is more complicated. We have plotted the periods as a function of the angle of incidence in Fig. 4.8 since it is hard to see this variation just from the reflectivity curves. The period variation is due to

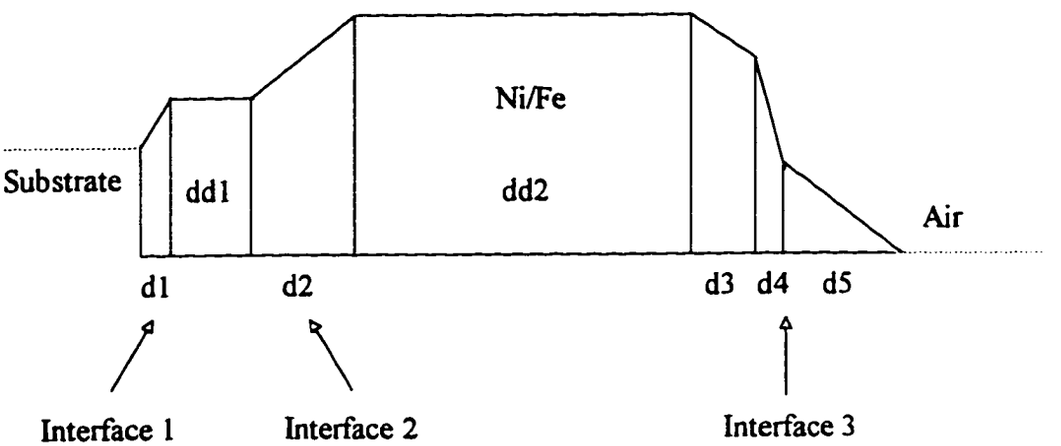

Fig. 4.7 Model and the definition of parameters for the reflectivity analysis of Ni/Fe thin film sample.

Table 4.1 Geometry parameters

Width of the interface 1[a]	d1	see footnote
Width of the interface 2	d2	21.0 (2.2) Å
First linear segment of interface 3 (top)	d3	36.0 (1.1) Å
Second linear segment of interface 3 (top)[a]	d4	see footnote
Third linear segment of interface 3 (top)	d5	50.4 (0.6) Å
Intermediate layer thickness	dd1	28.7 (1.2) Å
Bulk Ni/Fe layer thickness	dd2	734.3 (1.6) Å
Roughness of interface 1	σ1	5.7 (0.6) Å
Roughness of interface 2	σ2	7.3 (0.6) Å
Roughness of interface 3	σ3	5.3 (0.6) Å

[a] These two linear segments are very short and can be treated as step function.

Table 4.2 Weight percentage composition of Ni/Fe thin film

Wt%	dd1	dd2	below d4	above d4
Ni	0.77	0.80	0.72	0.27
Fe	0.12	0.20	0.26	0.23
O	0.11	0.00	<0.02	0.50
Total density (g/cm^3)	4.13	8.86	7.74	3.59

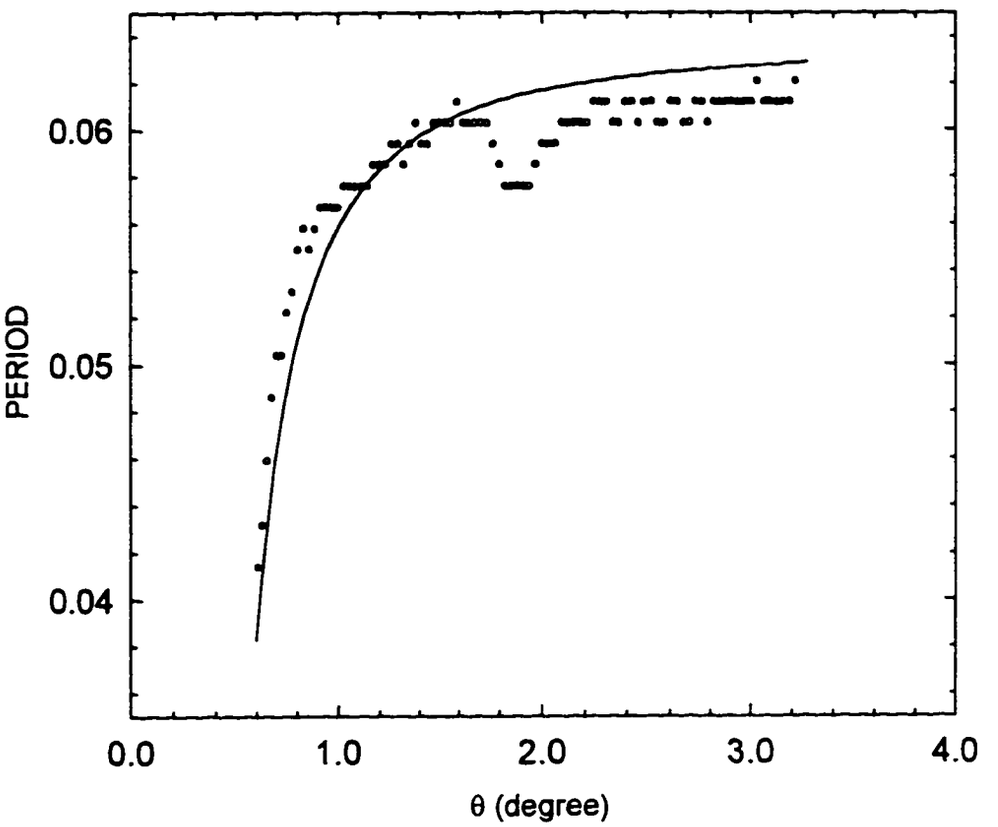

Fig. 4.8 Oscillation period as function of the angle of incidence. Line: the modified Bragg law, Circle: data (interpolated with fit).

changes in the phase difference of the reflected waves and related to the sublayer structures. We found out that to get a good fit to all orders of interference fringes, we must introduce an intermediate layer dd1 between the substrate and the alloy thin film in our model calculation. Therefore, there are three interfaces in our model structure. In Fig. 4.7, the interface 1 is between the intermediate layer and the substrate. The interface 2 is between the Ni/Fe alloy layer and the intermediate layer. The interface 3 is the top surface of the thin film. For interface 1 and 2, one linear segment is used to represent the spatial variation in the electron density. For interface 3, three are used. Our best fits shows that the width of interface 1 is very small and can be treated as a simple step function. However, there is a rms roughness of about 5.7 angstroms in the boundary position. Interface 2 has a width of about 21 angstroms, indicating that the electron density changes gradually from the intermediate layer to the Ni/Fe alloy layer. For interface 3, we used three linear segments to approach the real electron density. The total width is about 86 angstrom, which obviously can not be represented by a simple Gaussian factor only. We have tried to fit the data with a Gaussian factor for the top interface, what we got is an unrealistic large rms roughness and the output parameters are inconsistent for the different curves. There is a steep drop in electron density in the top surface model profile, sandwiched by two slowly decreasing region. This is an indication of the formation of an oxide barrier. The small amount of alloy components outside the steep drop is due to the metal ion transportation in further oxidation after the formation of the initial oxide layer. The slow decrease

in electron density below the oxide barrier has two reasons. First, the alloy film may be more loosely packed in the region closer to the top surface, due to the sputtering process. Second, transportation of vacancies during the oxidation also contributes to the reduction in the electron density.

Fig. 4.9a and Fig. 4.9b show the composition profile near the substrate and at the top surface. The Gaussian smeared profile was obtained by taking the in plane average of the local composition profiles using the rms roughness parameters assigned to each interface. The composition parameters are given in Table 4.2. We must point out the ambiguity in the oxygen composition determination. Because the x-ray energy is far away from the characteristic absorption edges of oxygen, one can not tell if it is oxygen or other light elements just from the reflectivity measurements. The dispersion behaviors are practically all the same for those elements with absorption edges far away from the x-ray energy. For example, the intermediate layer, which we believe is formed during the initial stage of the sputtering process, has about ten percent of oxygen or something other than nickel or iron in it. It is possible that an amorphous metal silicide layer be formed due to Ni/Fe sputtering. In that case there would be some silicon instead of oxygen in the intermediate layer.

At the top interface, especially above the oxide barrier, the iron/nickel ratio is higher than that of alloy thin film. This should be a result of competition between the oxidation rates and diffusion coefficients of the two elements. We carried out surface XAFS measurements on this sample and found that both Ni and Fe are in fcc environment. From the near edge

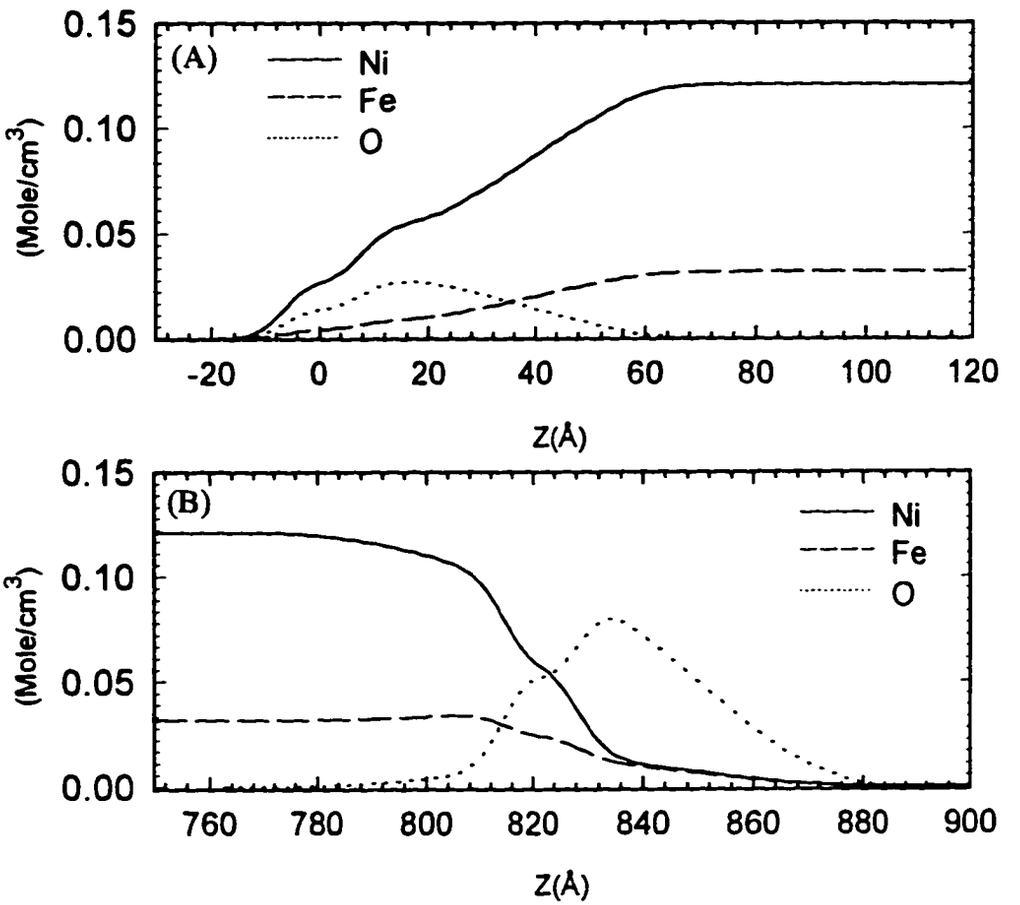

Fig. 4.9 (A) Composition profile of the Ni/Fe thin film at the alloy/substrate interface, (B) at the top surface.

XAFS the presence of metal-oxygen bonds was detected for both elements. Details of the XAFS work will be presented in appendix A.

The resonant reflectivity measurements for the Ni/Fe thin film can also be compared with an independent neutron reflectivity measurement for the same sample.[73] Fig. 4.10 shows the polarized neutron reflectivity measurements and the theoretical fits. The total thickness of the alloy thin layer derived from a two layer model analysis for the neutron measurements is 808 Å. This result is comparable with the thickness of the bulk Ni/Fe layer plus the top interface in table 4.1, which is dd2+d3+d4+d5 = 821 Å. Note that the neutron momentum transfer in Fig. 4.10 is only up to 0.04 $Å^{-1}$, which is typical in neutron measurements, and is about only one tenth of the momentum transfer in the x-ray measurements shown in Fig. 4.1. Therefore the neutron measurements can not give as accurate and detailed structural information as x-ray measurements. This is the reason why the intermediate layer (dd1, cf. Table 4.1) is not detected in neutron measurements. Moreover, not like the resonant x-ray reflectivity measurements, the neutron measurements can not discriminate between the Ni and Fe element in the alloy thin film. Nevertheless, the neutron analysis does show a different composition for the top surface layer. It also gives a smaller magnetic moment for the surface oxide layer, 0.328 μ_b vs. 2.24 μ_b for the bulk film. The top surface roughness from the neutron scattering was 1Å. We must point out that the resonant x-ray reflectivity measurements are more accurate both in counting statistic and momentum resolution.

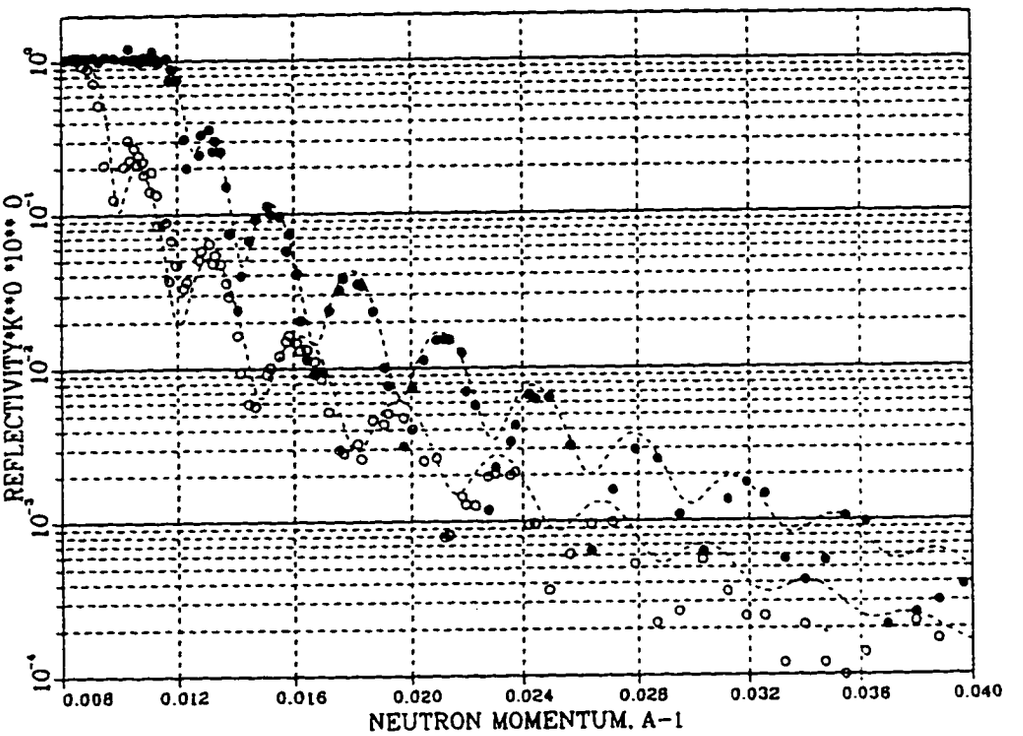

Fig. 4.10 The polarized neutron reflectivity measurements and the model fits. The solid circles are data points for the neutrons of spin up and the open circles are for the neutrons of spin down. The dash lines are model fits.

The errors in the geometry parameters are given in table 4.1. To some extent, there is correlation between the width and the rms roughness of each interface in the fitting of the individual reflectivity curve. Once again, the multi-energy curve fitting helps in eliminating the ambiguity because a linear segment in our calculation and a Gaussian factor acts differently as the energy changes. A detailed discussion about the correlation between fitted parameters is given in appendix B. The errors in the composition percentage are estimated to be less than 10%. This was tested by shifting the composition parameter off the best fits and monitoring the change of the least-squares sum of the fitting error.

In conclusion, the resonant x-ray reflectivity is a promising non-destructive method to measure the composition profile of thin films. With this method, we measured the composition profile of a Ni/Fe alloy thin film which gives important information in the study of passivation and corrosion of Ni/Fe alloy.

CHAPTER 5 RESONANT X-RAY REFLECTIVITY STUDIES OF CR/FE SUPERLATTICES [74]

5.1 Introduction

Cr/Fe superlattice is the first and most widely studied structure of the class of magnetic multilayers that is comprised of alternating layers of a ferromagnetic metal and a nonferromagnetic (or antiferromagnetic) spacer. The interest in this structure was provoked by the discovery of antiferromagnetic (AF) coupling of the Fe layers[75] as well as the giant magnetoresistance (GMR) effect.[76] There is great potential for technological applications, and curiosity to explore new materials from a fundamental point of view.

Magnetic coupling between the Fe layers was found to oscillate from AF to ferromagnetic (FM) with a period of about 18 Å or 12 monolayers (ML) in the Cr spacer thickness for sputtered Fe/Cr(110)-textured multilayers. [77] In addition to the long-period coupling of 12 ML, a short period of approximately two ML was found in epitaxially grown Fe/Cr/Fe(100) trilayers.[78] The two ML period oscillation are thought to be related to the nested Fermi surface of Cr.[79] The origin of the 12 ML long-period oscillation remains an open question even though some authors have suggested that it might be due to the short spanning vectors or equivalently the aliasing effect.[80]

The GMR effect is related to the AF interlayer coupling. The resistance of ferromagnetically coupled multilayers is lower than that of the same system coupled antiferromagnetically. The resistance of AF coupled multilayer is decreased to its FM value upon applying a strong enough magnetic field to overcome the antiferromagnetic coupling interaction and flip over the magnetization of the layers with opposite orientation, thus achieving the low resistivity FM state. The GMR value oscillates as the spacer thickness is increased, mimicking the oscillations of the AF interlayer coupling. A simple and illustrative theory can be used to explain the origin of GMR.[81] In FM state, the magnetic moments of all the layers are parallel and the scattering is weak for electrons whose spin is parallel to the magnetization direction. A majority spin electron can move through the system without spin flip and results in the low resistivity. In contrast, for the AF coupled state, the scattering is alternating between weak and strong for both spin-up and spin-down channels, and the resultant resistivity is higher.

The roughness and atomic-scale nature of the interfaces is considered crucial to the magnetic behaviors of magnetic multilayers.[82,83] Interfacial features can be controlled by various deposition conditions as well as post-deposition processing. T. Pierce et al[84] investigated the coupling of epitaxially grown Fe/Cr/Fe(100) trilayers, in which the Cr was deposited in a "wedge-shaped" layer of linearly increasing thickness at Fe substrate temperature of 30, 200 and 350°C. The roughness of the Cr growth front was measured with scanning tunneling microscopy (STM) and found to be

larger at lower temperature. The dependence of the oscillations of the exchange coupling on the Cr growth front roughness was then measured by using scanning electron microscopy with polarization analysis (SEMPA). They found that for higher temperature (lower roughness), the two ML period oscillation is dominant while for lower temperature, the short period is washed out due to the Cr spacer thickness fluctuations caused by the interface roughness. It should be noted that STM can only be used to measure the growth front roughness but not the embedded interface roughness. How the interface structure, such as topological roughness and atomic mixing , change the GMR is a question that need clarification. It has been observed that in the Fe/Cr system interfacial roughness increases the GMR effect.[85] By contrast, the increased GMR effect is attributed to the smoother interface in case of Co/Cu multilayers.[86] A. Kamijo and H. Igarashi[87] made a [Fe(30Å)/Cr(10Å)]$_{50}$ superlattice with "extremely " flat interface. They observed that while the absolute values of resistivity for both AF and FM state is lower than samples with rougher interface, the percent change of GMR is almost the same.

Given the importance of the interface roughness in the AF interlayer coupling and the GMR effect of Cr/Fe multilayers, scant information is available on such roughnesses. Equally obscure is the correlation between crystallinity and roughness. W. Hahn et al[88] examined the spin structure of Fe/Cr multilayers by polarized neutron diffraction. They observed the spin dependent neutron reflectivity of multilayers annealed at different temperatures and gave an estimation of the interfacial roughness of their

sample as about 6 Å. However, these parameters were not individually refined and given only as a guide to the work done. D. L. Williamson et al[89] investigated the structure of Cr/Fe multilayers using conversion electron Mossbauer spectroscopy (CEMS). The samples were prepared under different Ar sputtering pressures. They found that the quality of the interfaces between Cr and Fe is clearly degraded with increasing sputter pressure. By fitting the magnetic subspectra they estimated the interfacial roughness for the lower Ar pressures (1.3 mT) sample as 1 ML and for the higher Ar pressure (10 mT) sample as 2 to 3 ML. They also observed an isomer shift component for the 10 mT sample, which is an indication of a small fraction of Fe located in Cr layer. X-ray reflectivity measurements were also conducted for Cr/Fe multilayers [6,89], but used only for qualitative estimation of the interface quality. A problem hampers the using of the regular x-ray reflectivity technique for Cr/Fe multilayer is the poor optical contrast between the components. In this chapter, However, we will show that by properly selecting x-ray energy around the absorption edges of the components, various optical contrasts can be obtained and by analyzing the resonant reflectivity measurements at different energies, one can derive the interface information with improved accuracy.

Eric E. Fullerton et al [6] grew Fe/Cr superlattices by dc magnetron sputtering onto epitaxially polished single-crystal MgO(110) and MgO(100) substrates. The crystal orientation of the samples thus obtained is Fe/Cr(211) and Fe/Cr(100) respectively. They measured the AF interlayer coupling strength for a series of Fe/Cr(211) and Fe/Cr(100) superlattices

with different Cr layer thickness and found that the phase and period of the AF oscillations for both orientations are identical. This suggests that the long-period oscillation in Cr is independent of the crystallographic orientation of the spacer layer, challenging the existing theory which expect the crystallographic orientation dependence of the AF coupling strength. A second interesting result of their study concerns the large GMR values observed and, in particular, the 150% GMR value observed for the (100)-oriented sample. For the first two oscillations, the GMR values of the Fe/Cr(100) samples are considerably higher than those of the corresponding (211) samples. An interesting issue is whether this difference is intrinsic to the Cr orientations or results from extrinsic factors such as interfacial roughness and/or crystalline quality.[90] Detailed characterizations of the sublayer and interface structures are useful to address this question.

In this chapter we will present our results of the resonant reflectivity measurements on the $[Fe(20Å)/Cr(11Å)]_{20}$ superlattices of the both epitaxial orientations. We will show how the samples of the two orientations differ from each other in the degree of interfacial roughness and crystalline quality and discuss the possible correlation between the GMR effect and the sublayer and interface structures.

5.2 Experimentation

Sample Preparation

The Fe/Cr superlattices [91] were grown by dc magnetron sputtering onto epitaxially polished single-crystal MgO(100) and MgO(110) substrates. The sputtering chamber had a base pressure of $< 5\times10^{-8}$ Torr. The 2" planar magnetron sputtering guns were operated in an Ar pressure of 3 mTorr and a target-substrate distance of 9 cm. The (100) and (110) substrates were mounted side by side onto the sample holder and codeposited. A 100 Å Cr buffer layer was initially deposited at a substrate temperature of 600°C to establish the epitaxial orientation with the substrate and provide a template for the growth of the superlattice. The substrate was then cooled to 250°C and the superlattice is grown by sequential deposition of the Fe and Cr layers. The total number of bilayers is 20 and the nominal thickness of Fe and Cr layers are 20Å and 11Å respectively .

The MgO(100) surface (a_o=4.213Å) has an $a_o/\sqrt{2}$=2.98Å square surface net which is only 3.8% lattice mismatched with the Cr(100) surface upon a 45° rotation about the surface normal (i.e. Fe/Cr[001]/MgO[011], cf. Fig. 5.1(A)). The monolayer thickness (ML) of Fe/Cr(100) crystal is 1.435Å for Fe and 1.44Å for Cr. The MgO(110) surface has a rectangle surface net of 4.213Å × 2.98Å. The Fe/Cr[$\bar{1}$11]/ MgO[$\bar{1}$10] correspond to 16.7% lattice mismatch (cf. Fig. 5.1 (B)). The ML thickness in Fe/Cr(211) orientation is 1.172 Å for Fe and 1.176 Å for Cr. The ML thickness values given here are bulk crystal values. High-angle x-ray diffraction measurements on the Cr/Fe samples deposited with similar condition indicated that the values of ML thickness in multilayers agree with those of bulk crystals.[6]

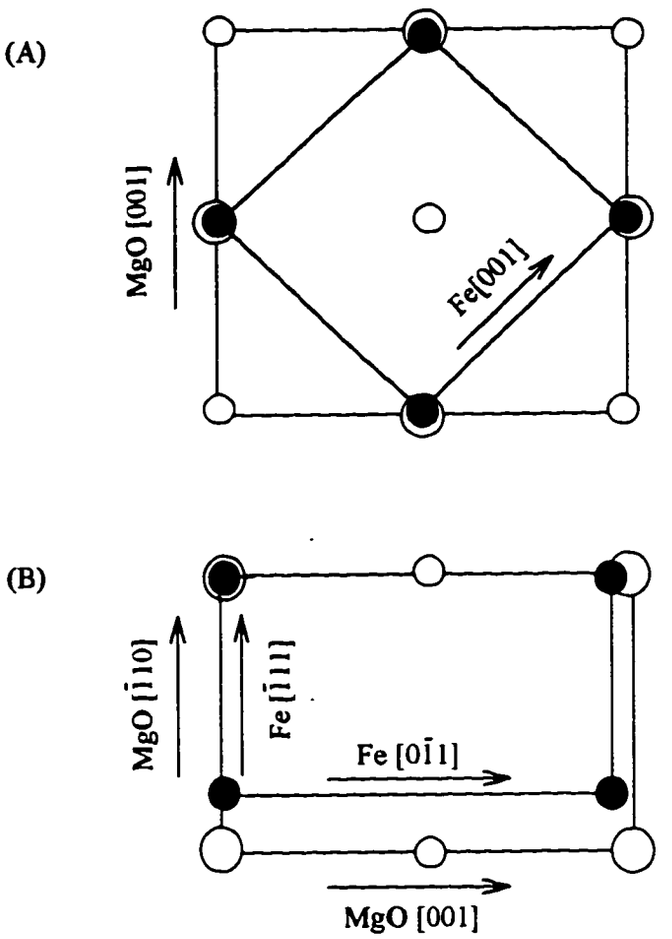

Fig. 5.1 The epitaxial relation of Fe/Cr superlattice (solid circles) with respect to the MgO substrate (open circles). (A) Fe/Cr(100) on MgO(100). (B) Fe/Cr(211) on MgO(110).

Resonant Reflectivity Measurements

The reflectivity measurements were conducted on beam line X-6B at the National Synchrotron Light Source at BNL. The experimental setup and the alignment procedure have been described in Chapter 3. Because of the small size of the samples (6.5mm×12.5mm), special attention has to be paid on the procedure of alignment to ensure the best illumination of x-ray beam on the samples at small angles. The experimental x-ray energies were 5.8, 6.1, 6.94, 7.16, 7.3 and 8.0 keV. The Fe and Cr K-edge energies are 7.112 and 5.989 keV, respectively. In Fig. 5.2 we plot the linear absorption (LA) and effective electron density (EED) for Fe and Cr as function of x-ray energy. For x-ray energy of 5.8 keV (marked by line a), we can get the largest contrast in EED but very small Contrast in LA between Fe and Cr components. At E = 6.1 (line b), the contrasts in both EED and LA are maximized. At E = 6.94 keV (line c), the contrast in EED is almost zero but remains large in the LA. At E = 7.16 (line d) the contrast in EED between Fe and Cr is inverted. For x-ray energies of 7.3 keV and 8.0 keV (line e and f) and above, the contrast in both EED and LA are small.

Fig. 5.3 and Fig. 5.4 show the reflectivity measurements for Fe/Cr(100) and Fe/Cr(211) superlattices, respectively, as function of x-ray momentum transfer Q_z. Two superlattices Bragg peaks are included in the measured reflectivity curves. The oscillations of small periods are due to the interference between the waves reflected from the top surface and the Cr-

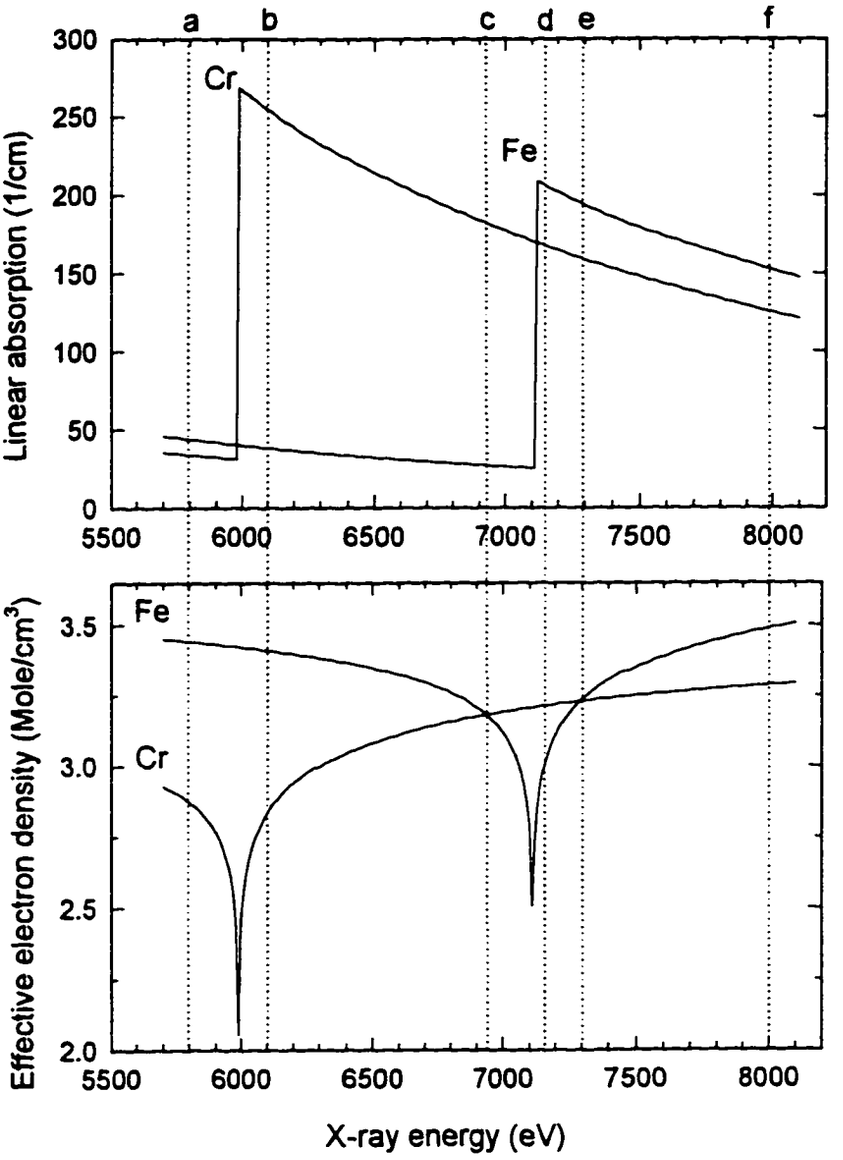

Fig. 5.2 The linear absorption and effective electron density of Cr and Fe. The energies used for resonant reflectivity measurements are indicated by the dot lines marked from a to f, corresponding to E = 5.8, 6.1, 6.94, 7.16, 7.3 and 8.0 keV, respectively.

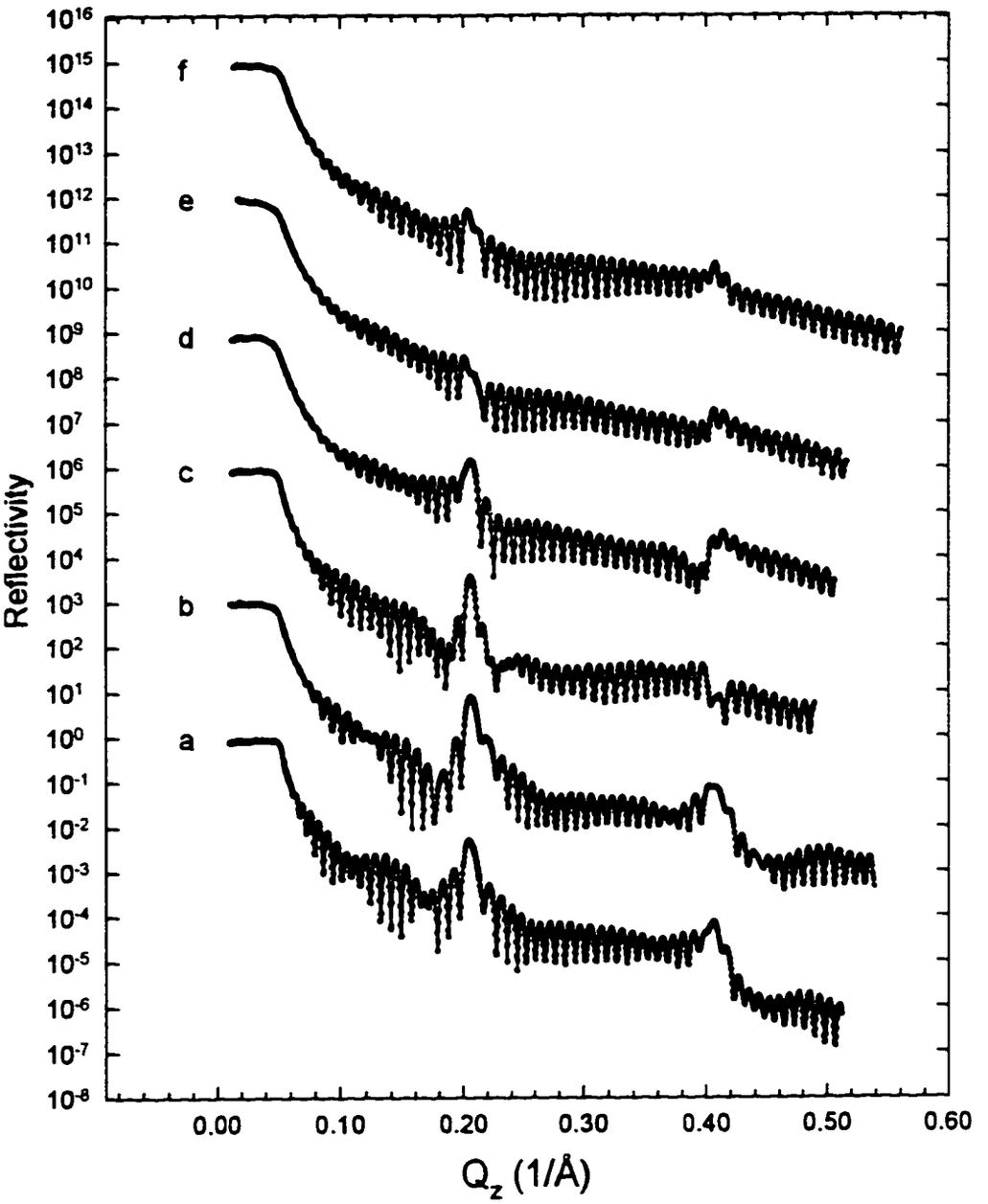

Fig. 5.3 Resonant reflectivity measurements for sample Fe/Cr(100). The solid lines are eye guides only. The x-ray energies used for these measurements are 5.8 keV (a), 6.1 keV (b), 6.94 keV (c), 7.16 keV (d), 7.3 keV (e) and 8.0 keV (f).

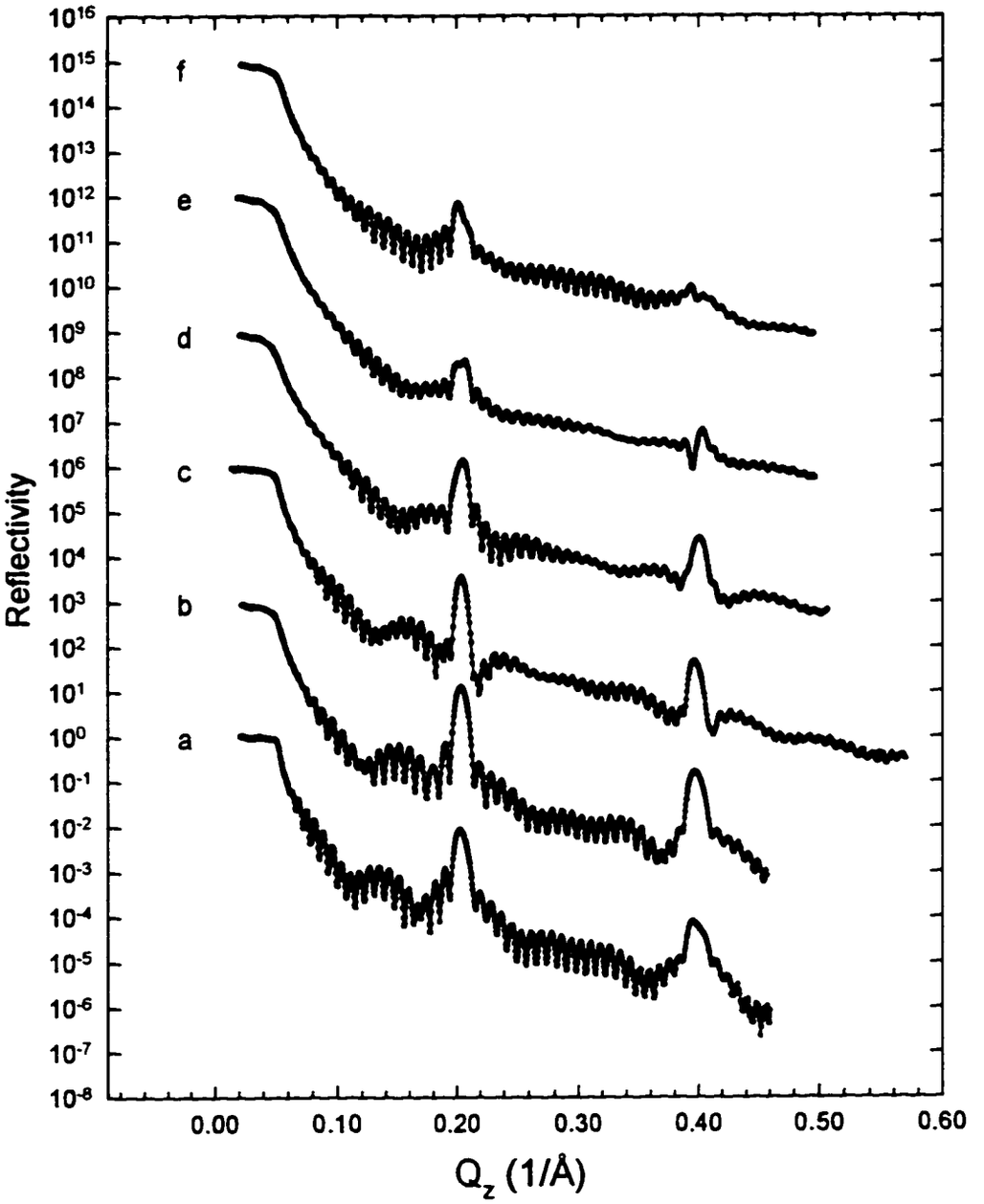

Fig. 5.4 Resonant reflectivity measurements for sample Fe/Cr(211). The solid lines are guides only. The x-ray energies used for these measurements are 5.8 keV (a), 6.1 keV (b), 6.94 keV (c), 7.16 keV (d), 7.3 keV (e) and 8.0 keV (f).

buffer/substrate interface. There is another larger oscillation period (about 0.05 1/Å) which is due to the 100 Å Cr buffer layer. The dependence of x-ray reflectivity on the beam energy is dramatic. The reflectivity curves of large EED contrast (curve a and b) show prominent Bragg peaks, as expected. On the other hand, in reflectivity curves of small EED Contrast (curve e and f), the Bragg peaks are relatively weak, especially for the Fe/Cr(100) curves, where the Bragg peaks are almost buried in the rapid oscillations resulting from the interference between the wave reflected from the top surface and the substrate interface. The reflectivity curves of inverted EED contrast (curve d) have asymmetric Bragg peaks which lean to the opposite direction to those of curve e and f. It is interesting to note the special line shapes for the curves with large LA Contrast but almost zero EED contrast (curve c), while the Bragg peaks are as prominent as those of curve a and b, there are slow varying dips around them. Fig. 5.5 and 5.6 show the model calculations of the reflectivity from a Fe/Cr superlattices with and without absorption. For reflectivity curves with zero EED contrast but large LA contrast (curve c in fig. 5.5) the Bragg peaks are prominent. In contrast, if the absorption is turned off in the calculation, the Bragg peaks simply disappear (curve c and e in Fig. 5.6). This suggests that the Bragg peaks in the reflectivity curves with zero EED contrast are purely due to the LA contrast.

The reflectivity curves show obvious difference between the two substrates too. The amplitudes of the top-substrate interference oscillations

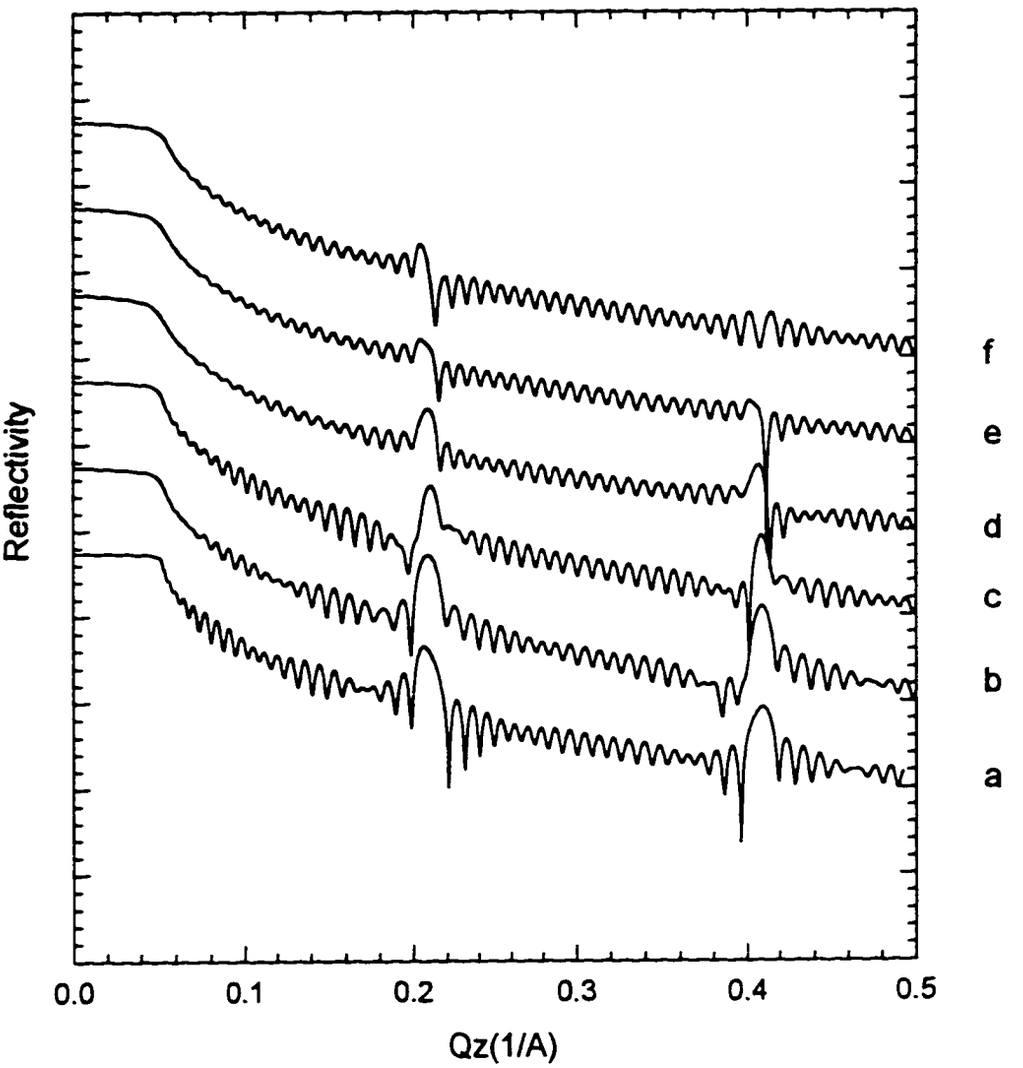

Fig. 5.5 Model calculations of the reflectivity curves from a Fe/Cr superlattices. The x-ray energies used in these calculations are 5.8 keV (a), 6.1 keV (b), 6.94 keV (c), 7.16 keV (d), 7.3 keV (e) and 8.0 keV (f). Zero EED contrast is assumed for curve (c) and (e).

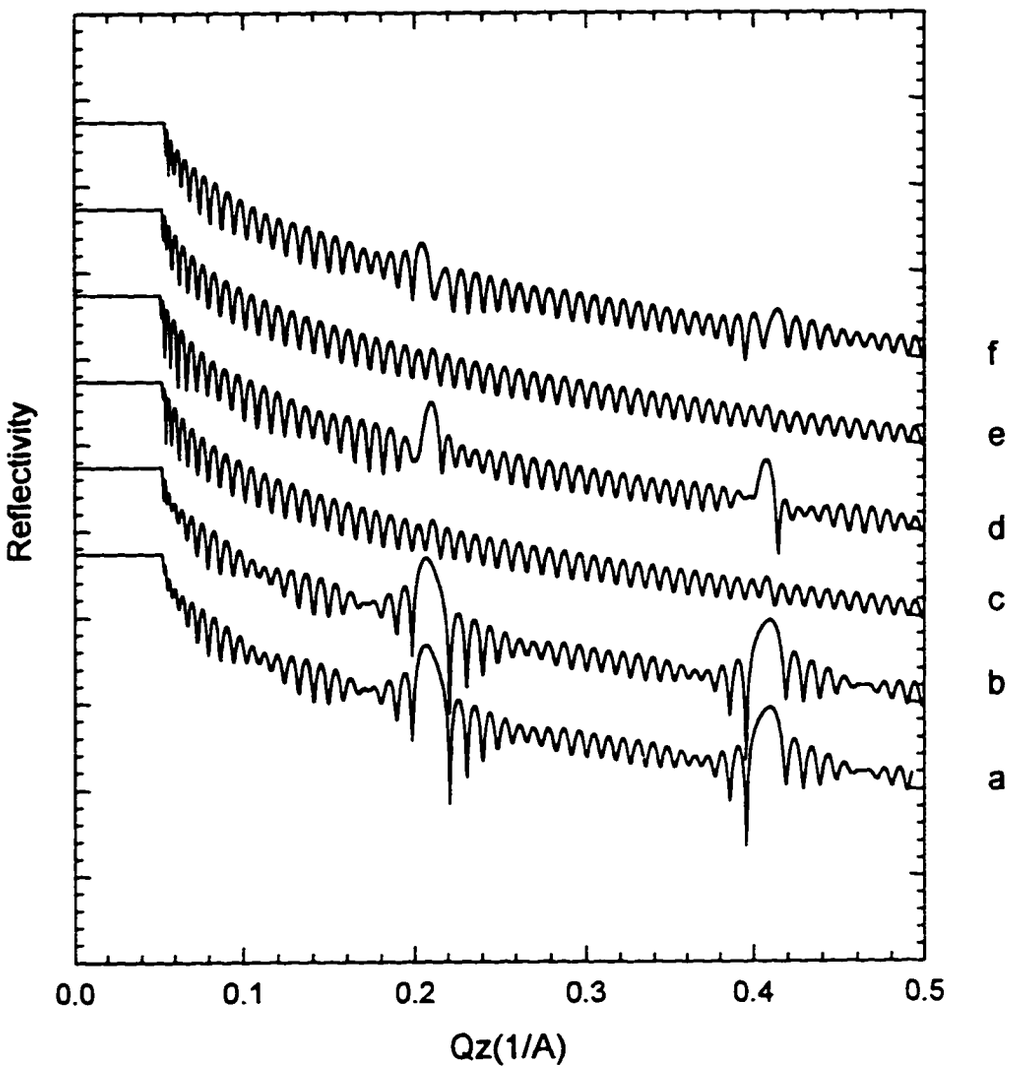

Fig. 5.6 Model calculations of the reflectivity curves from a Fe/Cr superlattices assuming zero linear absorption. The x-ray energies used in these calculations are 5.8 keV (a), 6.1 keV (b), 6.94 keV (c), 7.16 keV (d), 7.3 keV (e) and 8.0 keV (f).

are much bigger for sample Fe/Cr(100) than sample Fe/Cr(211). This reflects different structural parameters for the two samples.

5.3 Data Analysis and Discussion

The matrix formalism described in Chapter 2 is used for analysis of the reflectivity data. Height distribution functions of Gaussian type are used to characterize the Cr/Fe interfaces. The interfacial roughness or the width of the interface is represented by rms roughness σ's (cf. Eq. (2.10) to (2.21)). We assumed oxide mixing in the top two layers (Cr and Fe) to account for the increase of the layer thickness and total mass of the two top layers over the inner layers. As mentioned in Chapter 2 (cf. Eq. (2.9)), the effective electron density and linear absorption of each layer are calculated with the theoretical values for the constituent elements and are fixed in the fitting.

Fig. 5.7 to 5.12 show the model fitting to the reflectivity data taken with the six different x-ray energies for the Fe/Cr(100) sample and Fig. 5.13 to 5.18 for the Fe/Cr(211) sample, respectively. Given the complexity of the line shape of the data curves, the model calculation fits the six data curves quite well with very close parameters. Table 5.1 shows the structural parameters obtained from the fitting. The values are averaged over the six fits and the variances are given in the parentheses. The fitting is a little bit off around the second Bragg peak. The reason of this misfit may be due to the fluctuation of the layer thickness which makes the Bragg peaks wider, especially for the higher order peaks. In the fitting process we found that

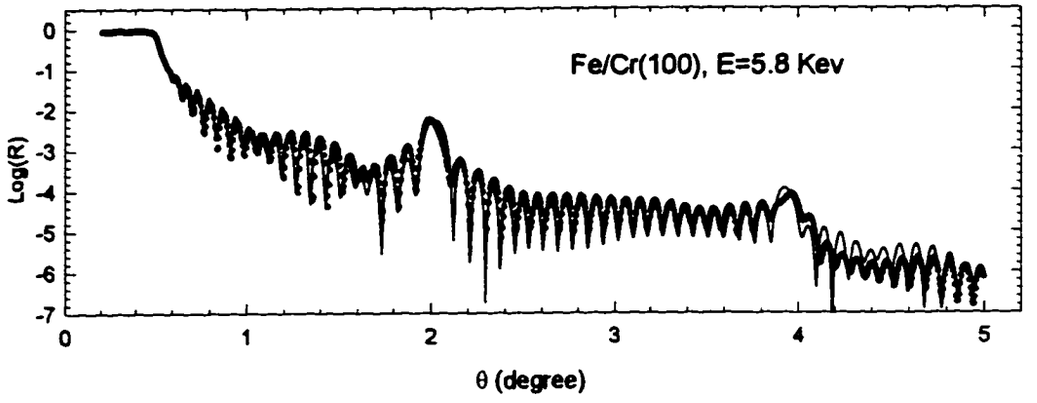

Fig. 5.7 The reflectivity measurements (circles) and fitting (line) curves for Fe/Cr(100) superlattices at 5.8 keV.

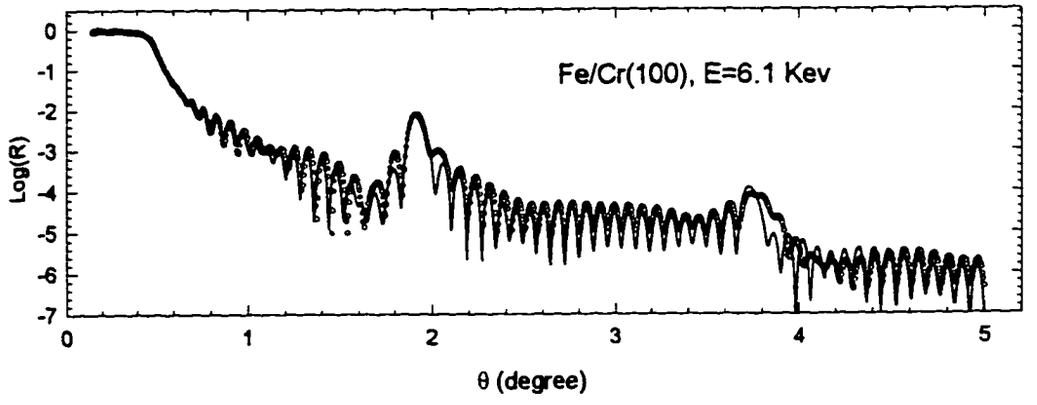

Fig. 5.8 The reflectivity measurements (circles) and fitting (line) curves for Fe/Cr(100) superlattices at 6.1 keV.

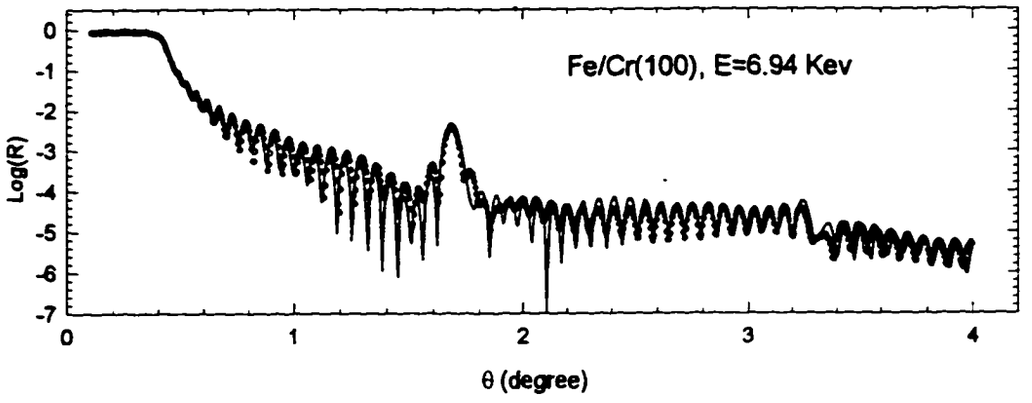

Fig. 5.9 The reflectivity measurements (circles) and fitting (line) curves for Fe/Cr(100) superlattices at 6.94 keV.

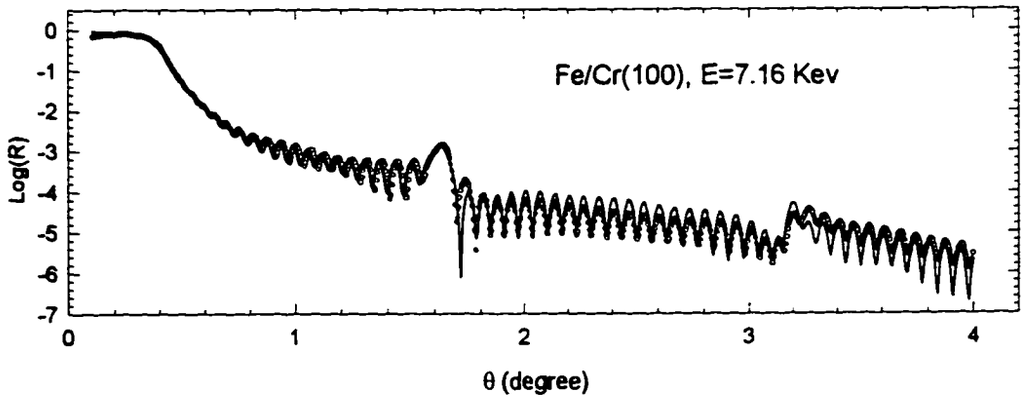

Fig. 5.10 The reflectivity measurements (circles) and fitting (line) curves for Fe/Cr(100) superlattices at 7.16 keV.

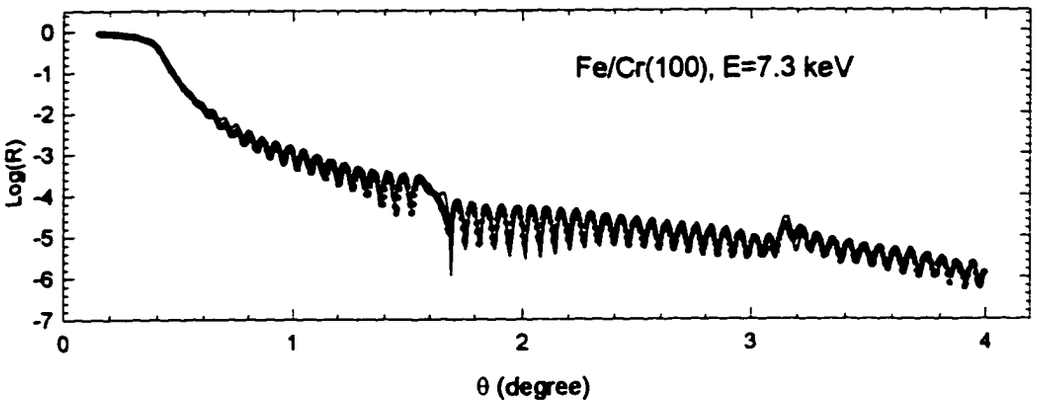

Fig. 5.11 The reflectivity measurements (circles) and fitting (line) curves for Fe/Cr(100) superlattices at 7.3 keV.

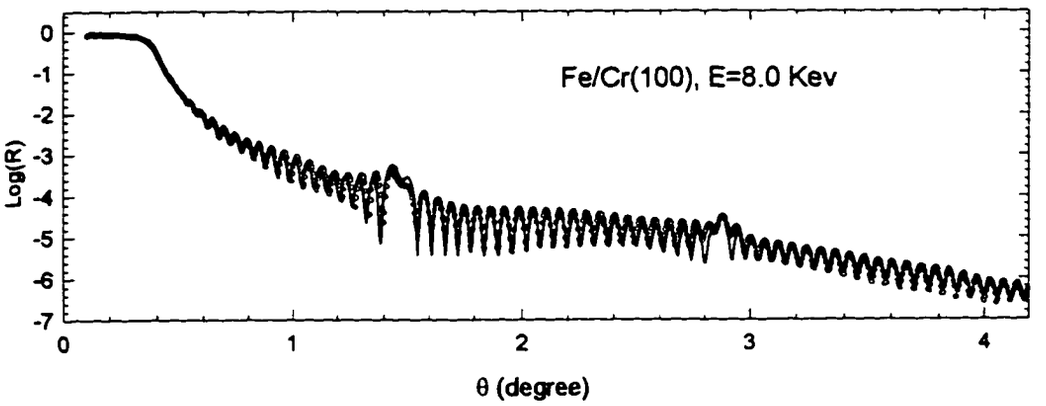

Fig. 5.12 The reflectivity measurements (circles) and fitting (line) curves for Fe/Cr(100) superlattices at 8.0 keV.

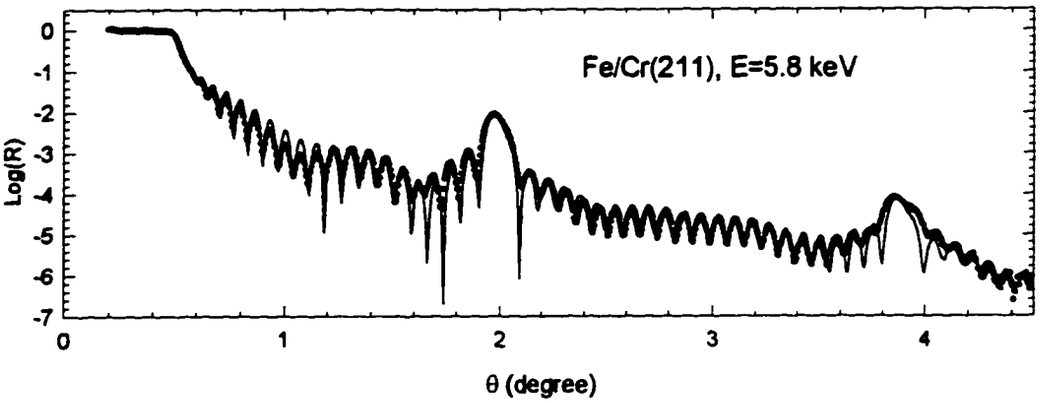

Fig. 5.13 The reflectivity measurements (circles) and fitting (line) curves for Fe/Cr(211) superlattices at 5.8 keV.

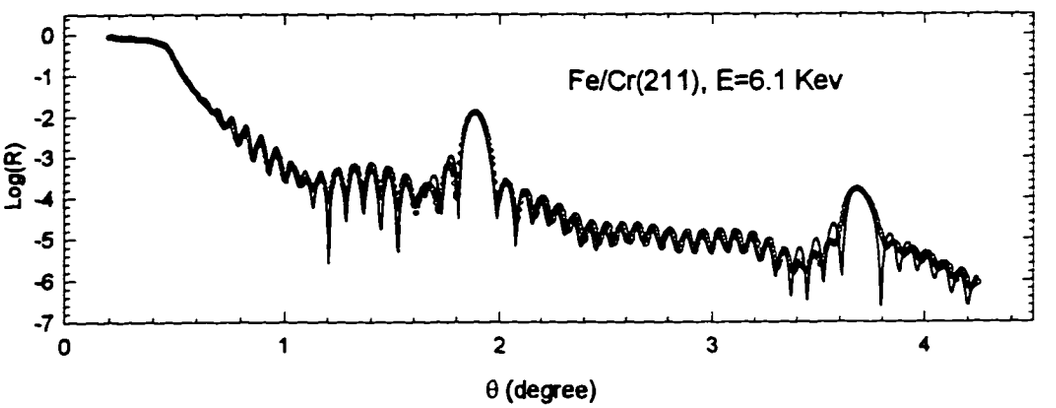

Fig. 5.14 The reflectivity measurements (circles) and fitting (line) curves for Fe/Cr(211) superlattices at 6.1 keV.

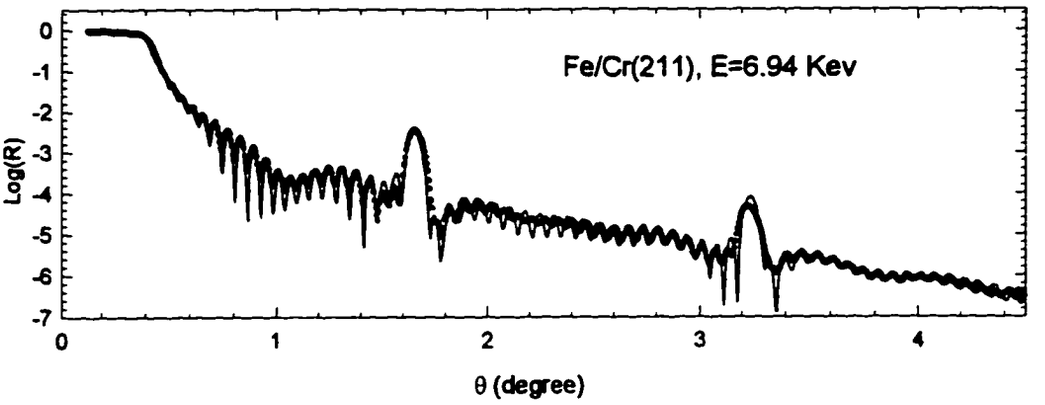

Fig. 5.15 The reflectivity measurements (circles) and fitting (line) curves for Fe/Cr(211) superlattices at 6.94 keV.

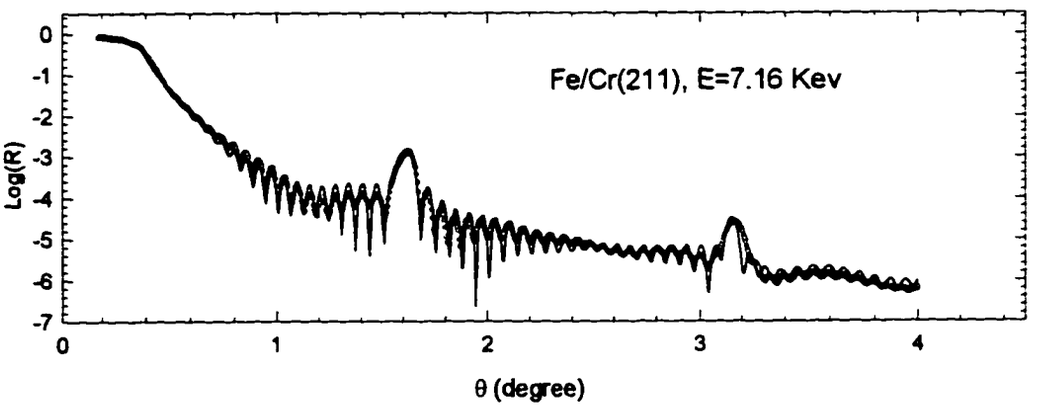

Fig. 5.16 The reflectivity measurements (circles) and fitting (line) curves for Fe/Cr(211) superlattices at 7.16 keV.

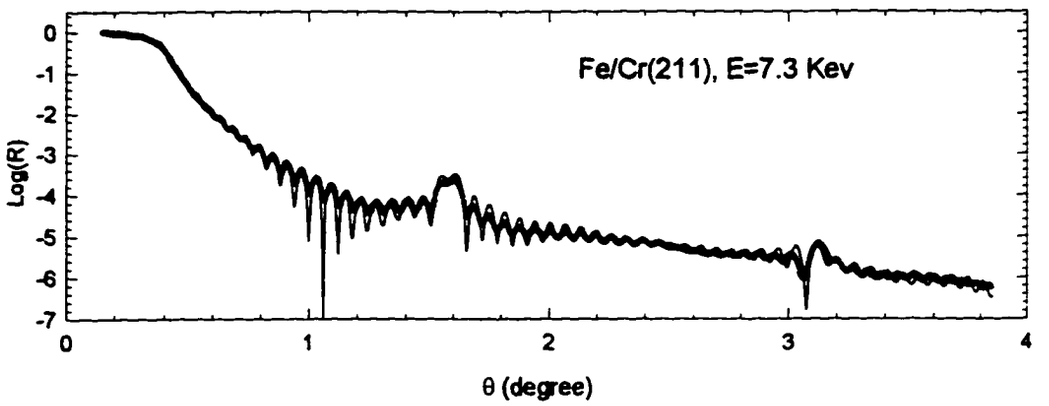

Fig. 5.17 The reflectivity measurements (circles) and fitting (line) curves for Fe/Cr(211) superlattices at 7.3 keV.

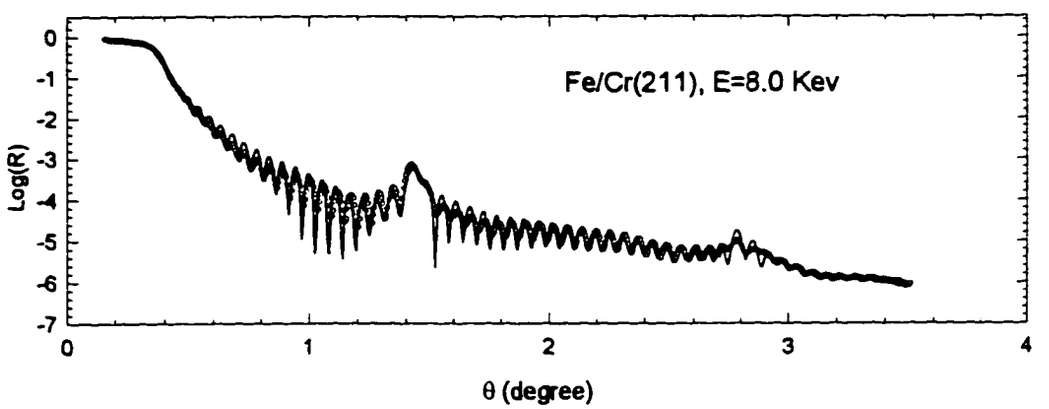

Fig. 5.18 The reflectivity measurements (circles) and fitting (line) curves for Fe/Cr(211) superlattices at 8.0 keV.

Table 5.1 List of parameters obtained from the analysis of the measurements (uncertaintes are given in parenthesis)

Parameter description		Sample Fe/Cr(100)	Sample Fe/Cr(211)
Layer thickness (Å)			
Cr buffer	d1	105.0 (1.0)	103.7 (1.0)
Cr/Fe bi-layers	d2	31.34 (0.05)	31.82 (0.04)
Cr layers	d3	11.1 (0.1)	11.3 (0.1)
Top Fe layer	d4	22.3 (0.8)	21.8 (1.0)
Top Cr layer	d5	15.9 (0.8)	21.5 (1.6)
Mass density (g/cm^3)			
Cr Buffer (Cr only)	M0	7.2 (fixed)	7.2 (fixed)
Inner Fe layers (Fe only)	M1	7.82 (0.03)	7.72 (0.03)
Inner Cr layers (Cr only)	M2	7.17 (0.06)	7.05 (0.07)
Top Fe layer (Fe and O)	M3	7.21 (0.08)	7.59 (0.07)
Top Cr layer (Cr and O)	M4	5.2 (0.3)	4.4 (0.3)
Interface width/roughness (Å)			
MgO/Cr buffer	$\sigma 1$	3.5 (0.3)	2.9 (0.2)
Cr buffer/Fe	$\sigma 2$	3.7 (0.3)	3.3 (0.5)
Fe/Cr	$\sigma 3$	2.8 (0.2)	2.7 (0.2)
Cr/Fe	$\sigma 4$	2.8 (0.2)	2.7 (0.2)
Top Fe / Top Cr	$\sigma 5$	3.0 (0.3)	4.7 (0.7)
Top Cr / Air	$\sigma 6$	2.5 (0.5)	7.3 (0.9)
Mole percent Oxygen in top layers*			
Top Fe layer		5	13
Top Cr layer		12	38

* The parameters for oxygen percent in the top Cr and Fe layers are estimated according to the mass increase compared to the inner layers and are fixed during the fitting.

the structure of the top layers controls the overall line shape of the curves while the inner layer structure controls the position and intensity of the Bragg peaks. To show the dependence of the intensity of the Bragg peak to the Cr/Fe and Fe/Cr interfacial roughness, we plot curves calculated with three different interfacial roughness values and the first Bragg peak data taken from Fe/Cr(211) sample with x-ray energy of 6.1 keV in Fig. 5.19. This plot can be considered as an estimate of the accuracy of the interfacial roughness. The sensitivity of the structural parameters to the data line shape is different for different energies. Generally speaking, the data curves with bigger EED contrast between Cr and Fe layers (i.e. E=5.8, 6.1keV) are more sensitive to the interfacial roughness than those with smaller EED contrast (i.e. E=7.3, 8.0 keV). The latter curves are useful in determining the interface structure at substrate and top surface since these parameters are less correlated to those of inner interfacial structures.

Because of the small weight percent of oxygen mixed in the top layers, The oxygen percentages are not sensitive parameters in the curve fitting. Therefore, the mole oxygen percentages given in Table 5.1 are calculated with the thickness and mass density of the top layers. For example, the thickness of the top Cr layer of the Fe/Cr(211) is 21.5 Å, the corresponding mass density is 4.4 g/cm^3, this gives a total layer density 94.6 gÅ/cm^3. The corresponding value for Cr in inner Cr layers is 11.3× 7.05=79.7 gÅ/cm^3. Thus the oxygen contribution to the top Cr layer density is 94.6-79.7 = 14.9 gÅ/cm^3, assuming there are same amount of Cr in both

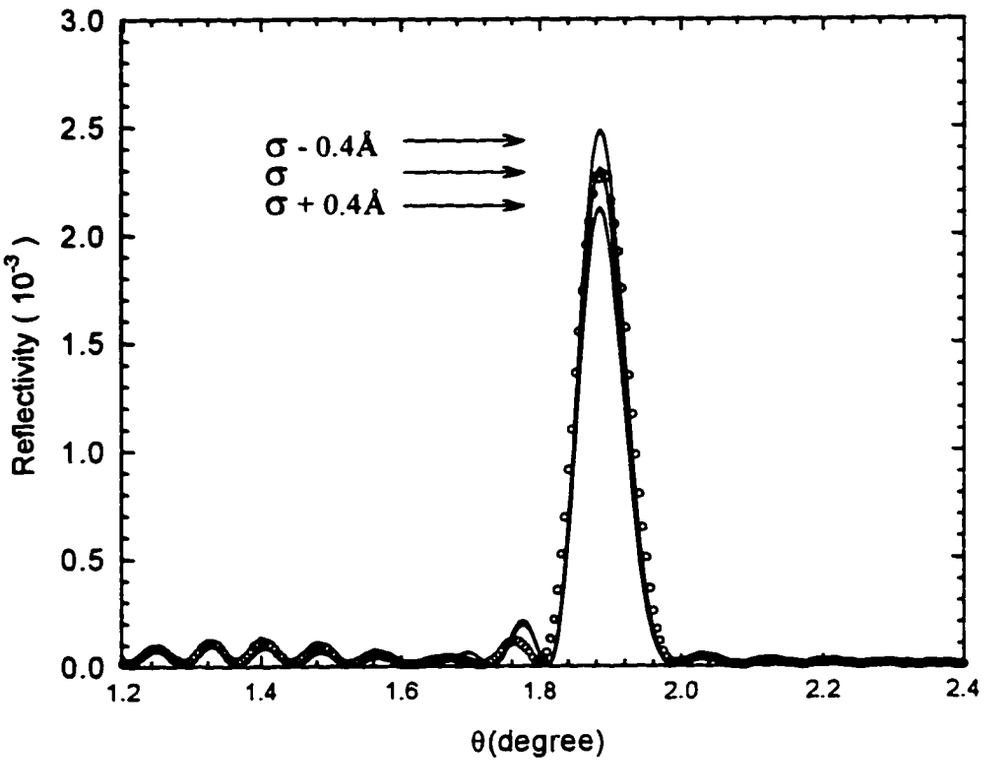

Fig. 5.19 The interfacial roughness dependence of the Bragg peak intensity. The data Curve (circles) is measured from Fe/Cr(211) around the first Bragg peak. The x-ray energy is 6.1 keV. The rms roughness σ (for both Cr/Fe and Fe/Cr interfaces) for the best fit is 2.7 Å.

top and inner Cr layers. This corresponds to 14.9/94.6 = 16% of oxygen in weight or 38% in mole.

Fig. 5.20 and 5.21 show the composition profile for Fe/Cr(100) and Fe/Cr(211), calculated with the structural parameters. In our fitting model, we assume pure Cr or Fe mass density values in the Cr and Fe layers. The interfacial mixture of the two elements is represented by the Gaussian distribution function. This will lead to an interfacial composition profile in the form of an error function. At the center of the Cr layer, the tails of the error function from both side meet and give a Fe mixture about 5 percent.

By examining the structural parameters given in table 5.1, we get the following inferences between the Fe/Cr(100) and Fe/Cr(211) superlattices. First, The rms roughness at Cr/Fe (Cr on top of Fe) and Fe/Cr (Fe on top of Cr) are about equal. They are 2.8 ±0.2Å for Fe/Cr(100) (about 2 ML) and 2.7±0.2Å for Fe/Cr(211) (about 2.3 ML). So the large difference in the giant magneticresistance between the two structures can not be attributed to the interfacial roughness. Second, The bilayer thickness is 31.34±0.05Å for Fe/Cr(100) and 31.82±0.04Å for Fe/Cr(211). This two parameters are very accurate because they are determined by the position of the Bragg peaks. The 0.5 Å difference in the bilayer thickness suggests that the Fe/Cr(211) superlattice may be a little bit more loosely packed than Fe/Cr(100) structure. Finally, There are more Cr and Fe oxidized in the top layers of Fe/Cr(211) than that of Fe/Cr(100). This may be another evidence that Fe/Cr(100) has better crystalline quality than Fe/Cr(211).

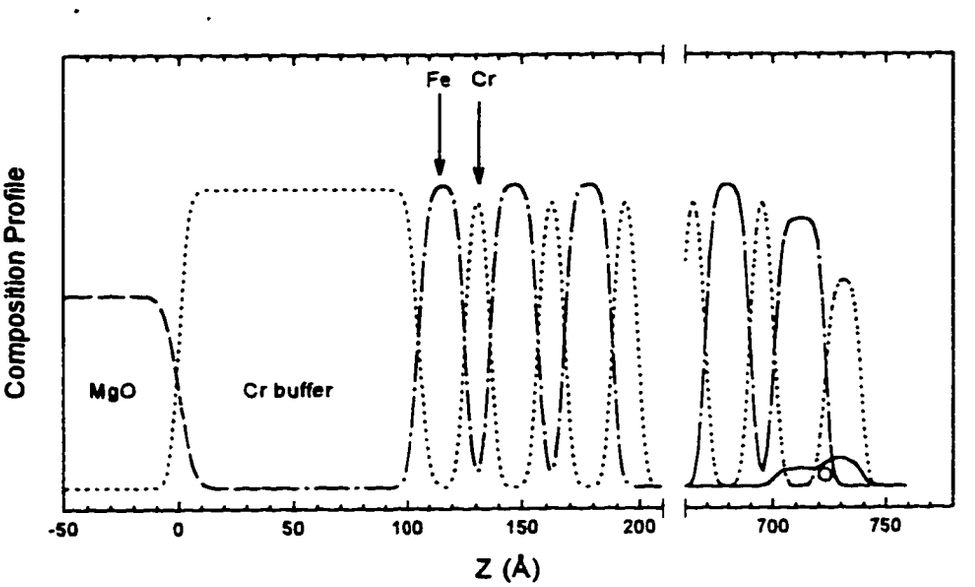

Fig. 5.20 Composition Profile of Fe/Cr(100) superlattices.

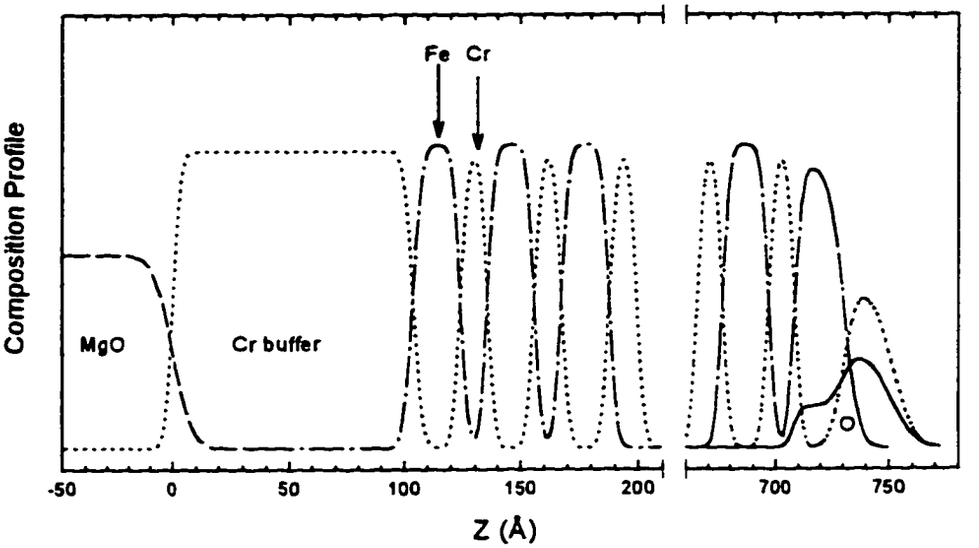

Fig. 5.21 Composition Profile of Fe/Cr(211) superlattices.

In conclusion, the resonant reflectivity measurement is an element sensitive method. It allows a more unequivocal structure analysis for Fe/Cr superlattices than the commonly used regular reflectivity method. With this method, we measured the interfacial roughness of Fe/Cr superlattices which, as far as we know, is the most accurate result up to now.

CHAPTER 6 CONCLUSION

The x-ray reflectivity has been widely used in studies of nanometric structures such as thin film and multilayers. The specular reflectivity data is related to the effective electron density distribution and can provide structural information about the interfaces. However, the current exploitation of reflectivity tools is limited by two major problems. First, regular reflectivity is not a element sensitive technique and can not provide information about the composition distribution. Secondly, due to the lack of phase information of the scattered waves it is difficult to determine the structural parameters uniquely. Even for a simple two-layer system, a single reflectivity data curve may correspond to different density profiles.[30]

Resonant x-ray reflectivity (RXR) method developed in this thesis can help to solve both problems. By using x-rays of different x-ray energies around the absorption edge of the elements, one can measure the reflectivity spectrums showing energy dependent features which are related to the composition structure of the sample. The contrast in the effective electron density and the linear absorption between the chemical components in the layered structures varies as the energy of the incident x-ray changes. This in turn changes the amplitude and phase of x-ray waves scattered from different interfaces of the sample and the interference patterns between them. The dispersion behaviors of the interference patterns contain more phase information than a single energy reflectivity

curve, thus make the determination of the structural parameters more unique and reliable.

The two examples of resonant x-ray reflectivity study on nanometric structures serve well as illustration for the merit of this new method. We demonstrated the possibility of using the RXR as a non-destructive method in composition depth analysis by measuring the composition profile of a Ni/Fe permalloy thin film. We also measured the interfacial roughness of Fe/Cr superlattices which is by now the most accurate result in quantitative determination of the interfacial structure of this system.

In conclusion, the resonant x-ray reflectivity is a promising non-destructive method in the analysis of nanometric structure. It provides more complete and unambiguous information about the interfaces and composition profile of thin film and multilayers.

APPENDIX A SURFACE XAFS MEASUREMENTS OF NI/FE ALLOY THIN FILM

The X-ray Absorption Fine Structure (XAFS) spectroscopy refers to the measurement of the x-ray absorption coefficient μ as a function of photon energy E across and above the threshold of an absorption edge. It is apparent that the probability of exciting an electron from an atomic energy level, that is, the absorption coefficient, is equal to the probability of creating a core hole in that level. Therefore, any process whose statistical average is proportional to the annihilation of the core hole is also proportional to the absorption coefficient and can be used as a measure of XAFS. In this thesis work, the x-ray fluorescence was used to measure the XAFS. The XAFS spectrum can be analyzed in two different regions: the near-edge region, which is from 20 eV below the absorption edge to about 50 eV above the absorption edge and the region of extended x-ray absorption fine structure (EXAFS), which may extend up to 1000 eV above the absorption edge.

The spectrum of near-edge region is called x-ray absorption near-edge structure (XANES). It contains information about the binding energies, quantum numbers and the low-lying unoccupied bound states of the absorbing atom. The position of the edge and the qualitative features of the absorption peak in the near-edge region are sensitive to the chemical valency of the absorbing atom, and to the symmetry of the surrounding near-neighbor atoms. [58]

The EXAFS arises through interference between the primary photoelectron wave and the backscattered electron wave from neighboring atoms. It is this interference that gives rise to the sinusoidal modulation of μ vs E in the EXAFS spectrum. The analysis of the spectrum gives local information about the crystal structure, atomic coordination and inter atomic distances. The EXAFS function χ is defined as the modulation of the absorption rate, normalized to the "background" absorption μ_0: [92]

$$\chi(E) = \frac{\mu(E) - \mu_0(E)}{\mu_0(E)} \tag{A1}$$

We measured the XAFS at both the Ni and Fe K-edges by measuring the fluorescence spectra induced by synchrotron x-ray with glancing incident angles. The experiments were conducted at beamline X6B and X18B of NSLS in Brookhaven National Laboratory. The optical and electronic setup of fluorescence surface XAFS are shown in Fig.3.4 and Fig.3.5. The EXAFS spectrums show that both Ni and Fe in the alloy sample see an fcc environment. The near edge structures indicate that there are both Ni and Fe oxide on the Ni/Fe thin film surface.

Ni K-edge XAFS

The Ni K-edge XAFS data were collected with the angle of the x-ray incidence set to 0.213° and 0.426°. At Ni K-edge (8.333 keV), they correspond to Q_z values of 0.03 1/Å (below the critical angle of total reflection) and 0.06 1/Å (above the critical angle, cf. Fig.4.1). Fig.A1

shows the electric field intensity distribution at the Ni/Fe thin film surface for the two incident angles. The Ni K-edge fluorescence radiation is proportional to the product of the Ni density and the electric field intensity. As one can see from Fig.A1, the electric field E_1 ($\theta = 0.213°$) decays rapidly in the thin film and the fluorescence is mainly emitted by Ni metal and Ni oxides at the top surface. On the other hand, the electric field E_2 is almost uniformly distributed through out the thin film and the main contribution to the fluorescence signals is from the bulk Ni atoms. Fig.A2 shows the X-ray Absorption Near Edge Structure (XANES) data. The pronounced peak at about 16 eV above the edge in the NiO standard spectra is due to dipole-allowed transitions of 1s electron to levels with substantial p-orbital character.[93,94] It is a characteristic feature of the Ni-O bond. The Ni K-edge XANES spectra of the Ni/Fe thin film with $\theta = 0.213°$ shows a near peak which is similar to that of NiO standard, while the spectra at $\theta = 0.426°$ is basically the same as the Ni metal standard. This suggests Ni oxide form on the top surface of the Ni/Fe thin film. Fig. A3 shows the k^3 weighted Fourier transforms of the Ni K-edge EXAFS spectra. $k = [2m(E - E_o)/\hbar^2]^{1/2}$ is the electron wave number. In a spectrum of Fourier transform of the EXAFS, the contributions to the EXAFS spectrum from different coordination shells are isolated. For example, the strong peak centered around 2.1 Å in the Ni/Fe spectra corresponds to the first nearest neighbors of the central Ni atom. The position of the peak is related but not equal to the inter-atomic distance because of the k dependent electronic phase shift. The spectra of Ni/Fe thin film at the two incident angles are

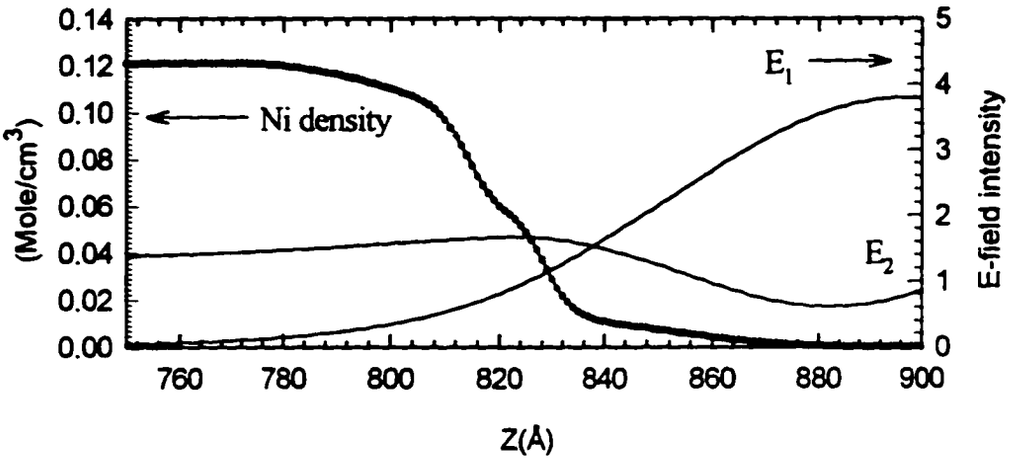

Fig. A1 The electric field intensity distribution in Ni/Fe alloy thin film at Ni K-edge. E_1 is the electric field for $\theta = 0.213°$ and E2 for $\theta = 0.426°$. The circles are for Ni mole density.

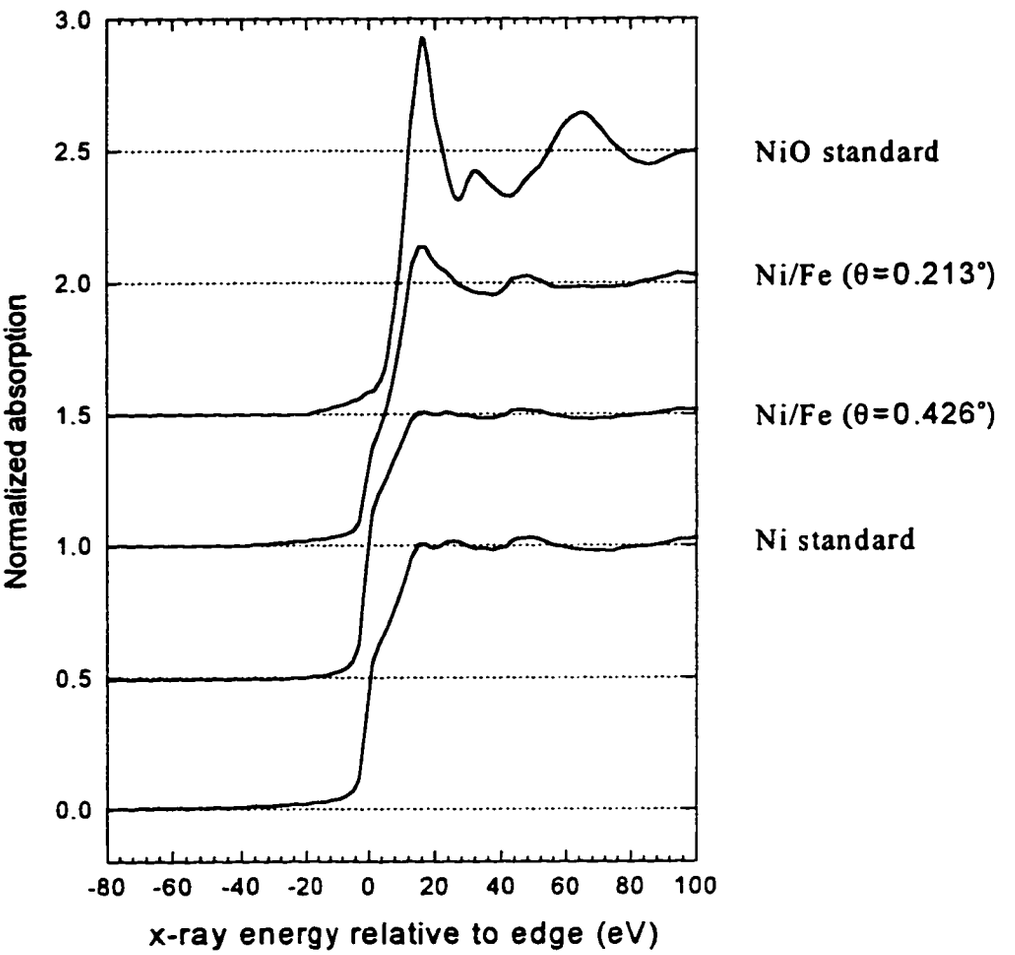

Fig. A2 The X-ray Absorption Near Edge Structure of Ni/Fe thin film at Ni K-edge.

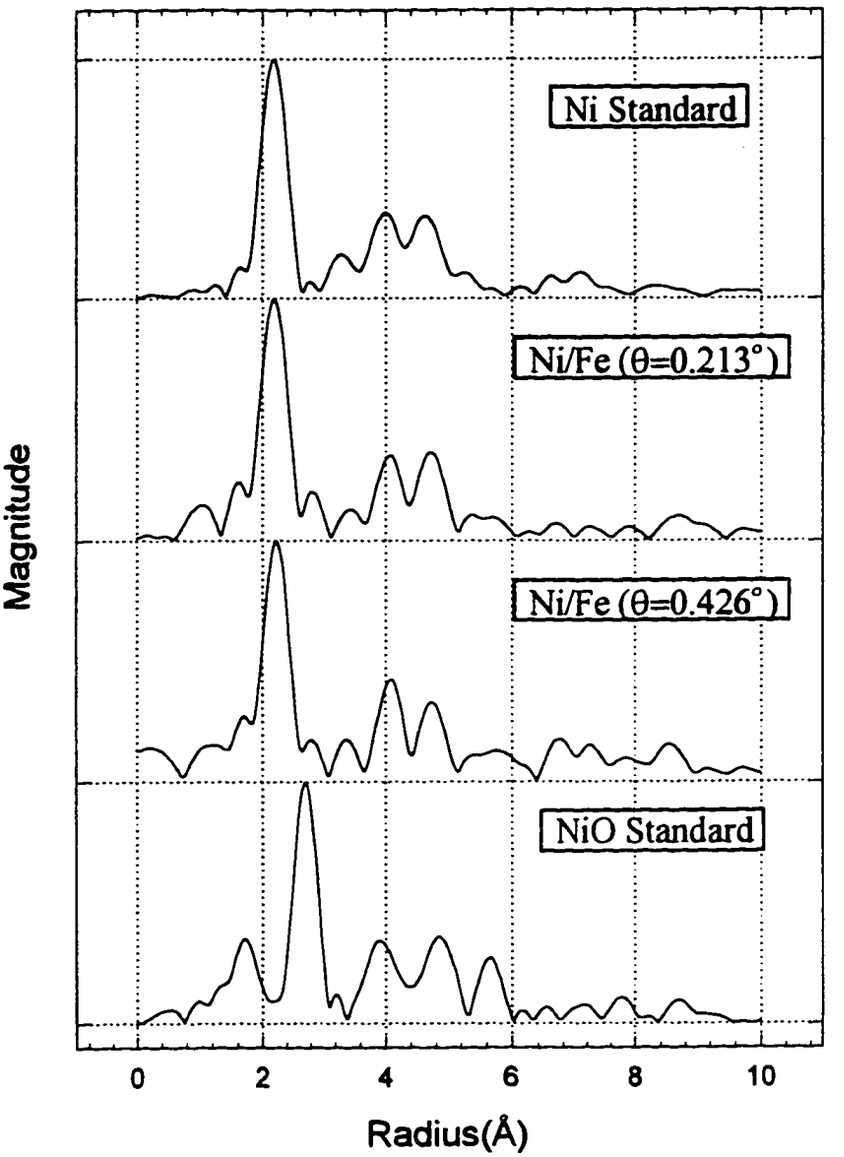

Fig. A3 The k^3 weighted Fourier transforms of the Ni K-edge EXAFS spectra of the Ni/Fe thin film.

similar and resemble that of Ni standard. This means that the Ni/Fe alloy has an fcc structure as pure Ni. Also shown in Fig.A3 is the Fourier transform of the EXAFS for the NiO standard which has a cubic close-packed structure.[91] The difference between the Ni/Fe spectra and NiO spectra suggests that the surface oxidation does not change the fcc structure of the bulk Ni/Fe alloy, as expected.

Fe K-edge XAFS

The Fe K-edge XAFS data were collected with the angle incidence set to 0.25° and 0.5°. At Fe K-edge (7.112 keV), they correspond to Q_z values of 0.03 1/Å and 0.06 1/Å, respectively. Fig.A4 shows the electric field intensity distribution at the Ni/Fe thin film surface for the two incident angles. Fig.A5 shows the Fe K-edge XANES spectra. The spectra at θ = 0.25° (below the critical angle) shows an oxidation peak resembling that of the Fe_2O_3 standard, while the spectra at θ = 0.5° does not. The spectra at θ = 0.5° does not looks like that of the bcc Fe standard either since the Fe in the Ni/Fe alloy thin film has the fcc structure. This can be seen more clearly in Fig.A6, where the Fourier transforms of the Fe K-edge EXAFS of the Ni/Fe thin film sample at the two angles are shown, together with the those of K-edge EXAFS of Ni metal standard (fcc structure) and Fe metal standard (bcc structure).

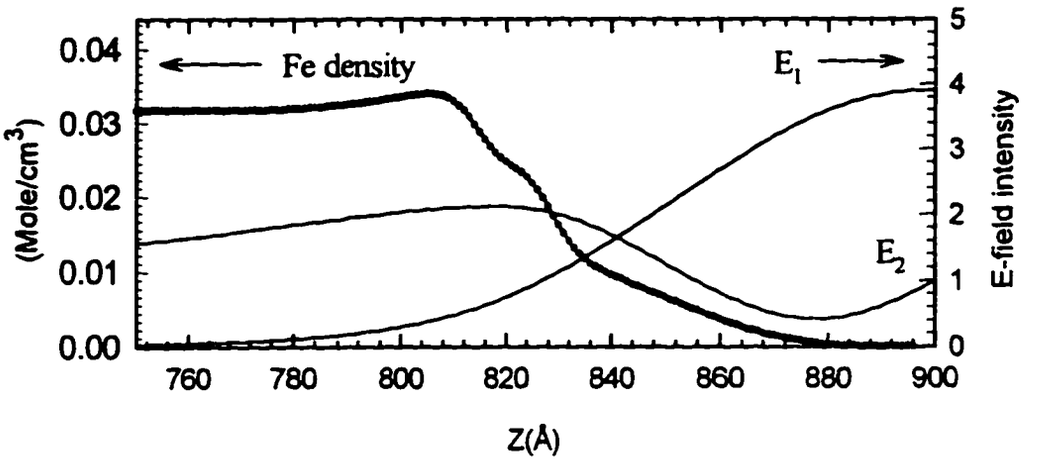

Fig. A4 The electric field intensity distribution in Ni/Fe alloy thin film at Fe K-edge. E_1 is the electric field for $\theta = 0.25°$ and E2 for $\theta = 0.5°$. The circles are for Fe mole density.

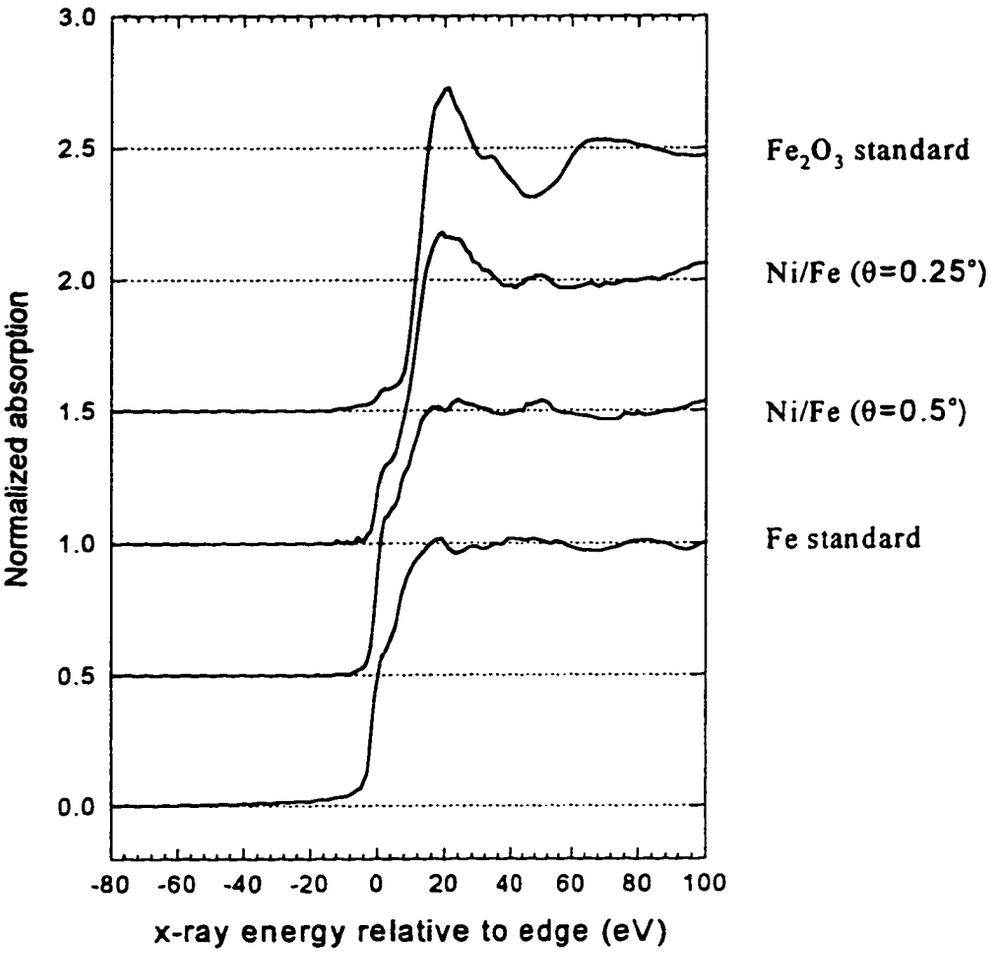

Fig. A5 The X-ray Absorption Near Edge Structure of Ni/Fe thin film at Fe K-edge.

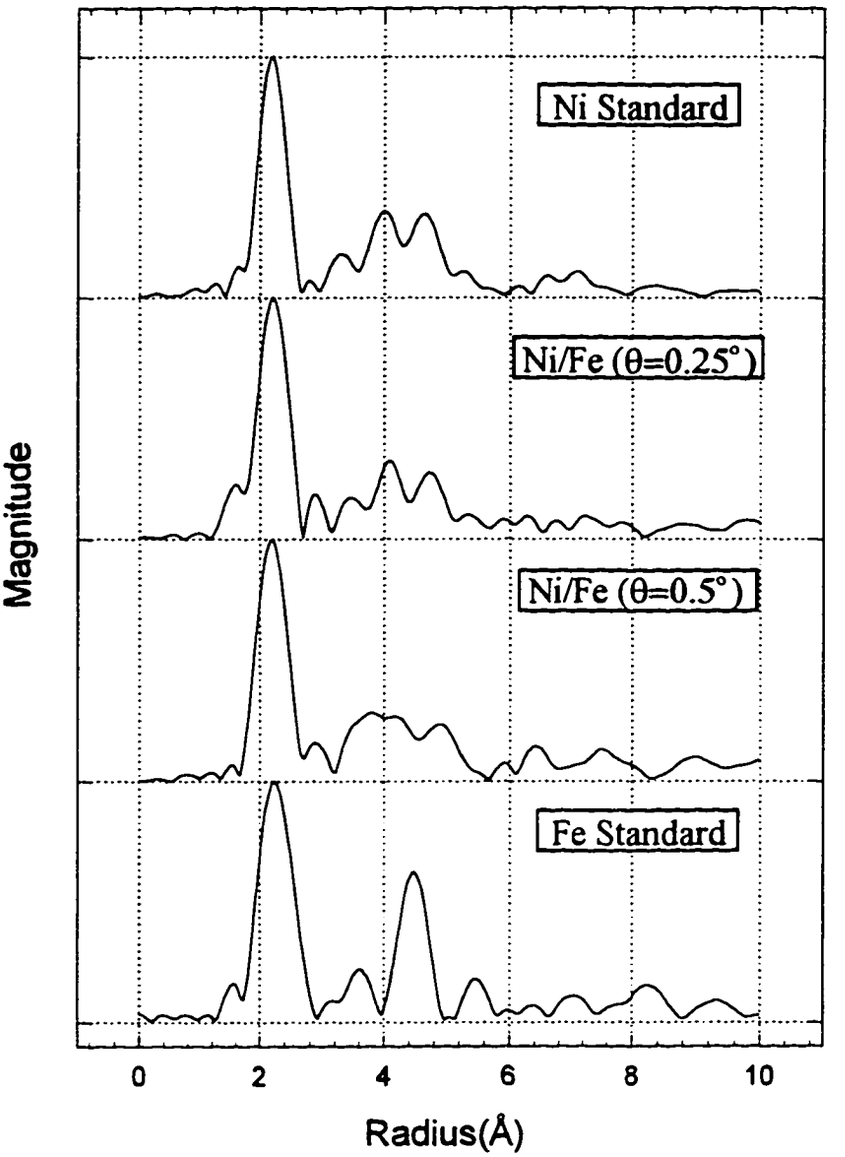

Fig. A6 The k^3 weighted Fourier transforms of the Fe K-edge EXAFS spectra of Ni/Fe thin film.

APPENDIX B THE COEFFICIENT OF CORRELATION BETWEEN THE UNCERTAINTIES OF THE PARAMETERS IN THE NONLINEAR LEAST-SQUARE FITTING

The nonlinear least-square fitting procedure[95] involves solving a set of linear equations:

$$\sum_{l=1}^{M} \alpha_{kl} \delta a_l = \beta_k \tag{B1}$$

Where α_{kl}'s are components of the curvature matrix which is defined as the matrix of the second order partial derivatives of the merit function χ^2 with respect to parameters a_l's:

$$\beta_k \equiv -\frac{1}{2}\frac{\partial \chi^2}{\partial a_k} \qquad \alpha_{kl} \equiv \frac{1}{2}\frac{\partial^2 \chi^2}{\partial a_k \partial a_l} \tag{B2}$$

and the χ^2 merit function is:

$$\chi^2(\mathbf{a}) = \sum_{i=1}^{N} \left[\frac{y_i - y(x_i;\mathbf{a})}{\sigma_i} \right]^2 \tag{B3}$$

Where x_i and y_i are data points, σ_i the standard deviation and $y(x_i;a)$ the model calculation based on the parameter vector **a**.

Once the acceptable minimum has been found, the estimated covariance matrix **C** of the standard errors in the fitted parameter **a** can be computed:

$$[C] \equiv [\alpha]^{-1} \tag{B4}$$

The coefficient of correlation between parameter a_i and a_j is then defined as:

$$r(a_i,a_j)=\frac{C_{ij}}{\sqrt{C_{ii}C_{jj}}} \tag{B5}$$

This is a number between -1 and 1. A positive value of $r(a_i,a_j)$ indicates that the errors in a_i and a_j are likely to have the same sign, while a negative value indicate the errors are anticorrelated, likely to have opposite signs.

Table B1 shows the coefficient of correlation between the uncertainties of the parameters in our resonant reflectivity analysis for Fe/Cr(211) superlattices. The first two columns list the parameter pairs a_i and a_j. (refer Table 5.1 for the parameter definition). Column 3 to column 8 show the correlation calculations based on the fits of reflectivity curves at difference x-ray energies. The last column shows the correlations obtained from the simultaneous fitting of all six x-ray energies.

The coefficients of correlation presented in Table B1 show strong energy dependent. This is an advantage of resonant reflectivity since by careful selecting the x-ray energy, one can find the best way to break the correlation between certain parameters. For example, the correlations between mass density of Fe and Cr embeded layers (M1 and M2) are about 0.6 for x-ray energies around and above Fe K-edge, but only -0.01 and -0.2 for the two energies around Cr K-edge, where the contrast in EED between Fe and Cr layer is maximized. It is also interesting to compare the correlation between some parameters for x-ray energy of 6.1 keV (positive Fe/Cr EED contrast) and 7.16 keV (negative Fe/Cr EED contrast). For example, the correlations between the mass density and layer thickness of Cr layers, r(M2,d3) and r(M4,d5), and also the correlations between the

Cr/Fe interfacial roughness and mass density of Cr layers, $r(\sigma 3,M2)$ and $r(\sigma 4,M2)$, have opposite signs for the two energies, and are significantly reduced in the fitting combining all six curves.

The absolute values of the correlation coefficients in Table 5 are found to be less than 0.6 in at least one column, and most of them are less than 0.2. The parameter pair which is mostly correlated is ($\sigma 6$,M4), the mass density of top Cr layer and the roughness of Air/Cr interface. The uncertainty in these two parameters might be larger than estimated in table 5.1 due to this correlation.

In summary, it is evident that the resonant reflectivity method helps in reducing the correlation between fitting parameters in x-ray reflectivity analysis.

Table B1 The coefficient of correlation between the uncertainties of the parameters in Fe/Cr(211) reflectivity fits.

Parameter a_i	a_j	5.8 keV	6.1 keV	6.94 keV	7.16 keV	7.3 keV	8.0 keV	all 6 curves
d2	d1	-0.26	-0.19	-0.08	-0.20	-0.18	-0.46	-0.26
d3	d1	0.62	0.59	0.03	0.56	0.11	0.76	0.36
d4	d1	-0.53	-0.64	-0.58	-0.60	-0.63	-0.38	-0.20
d5	d1	0.17	0.30	-0.17	0.33	-0.23	-0.17	-0.07
M1	d1	-0.12	-0.12	-0.55	0.44	-0.09	-0.17	0.01
M2	d1	0.62	0.38	0.02	-0.03	-0.30	0.29	0.06
M3	d1	0.18	0.21	-0.25	0.43	-0.32	-0.06	0.04
M4	d1	0.03	0.15	-0.15	0.22	0.24	0.01	0.05
σ1	d1	-0.13	-0.23	0.12	-0.04	-0.12	0.18	0.00
σ2	d1	-0.36	0.21	-0.05	-0.32	0.33	-0.16	0.06
σ3	d1	-0.62	-0.78	-0.33	-0.67	-0.16	-0.66	0.07
σ4	d1	-0.60	-0.02	-0.50	-0.32	0.33	-0.18	-0.01
σ5	d1	-0.01	-0.20	-0.07	0.10	-0.32	0.01	-0.09
σ6	d1	-0.01	0.03	-0.14	0.11	0.31	0.04	0.06
d3	d2	-0.01	-0.20	-0.14	-0.07	-0.40	-0.25	-0.13
d4	d2	-0.09	0.11	0.02	0.04	-0.36	0.18	-0.24
d5	d2	-0.04	-0.32	-0.01	-0.10	-0.23	-0.06	0.14
M1	d2	0.20	0.21	0.19	0.14	0.07	0.25	0.06
M2	d2	-0.01	-0.06	0.32	0.12	-0.27	-0.05	0.07
M3	d2	0.21	0.10	0.12	-0.04	-0.19	-0.04	0.04
M4	d2	0.02	0.17	0.33	0.02	0.14	-0.24	0.14
σ1	d2	0.00	-0.07	0.03	-0.01	0.01	-0.14	0.00
σ2	d2	0.18	0.09	-0.08	-0.05	0.02	0.20	-0.08
σ3	d2	0.06	-0.04	-0.34	0.05	0.02	0.18	-0.20
σ4	d2	-0.06	0.10	-0.30	-0.03	0.39	0.18	-0.21
σ5	d2	-0.15	-0.24	-0.48	-0.26	-0.32	0.12	-0.32
σ6	d2	-0.19	0.19	0.25	-0.02	0.06	-0.38	0.07

Table B1 (Continued)

Parameter a_i	a_j	5.8 keV	6.1 keV	6.94 keV	7.16 keV	7.3 keV	8.0 keV	all 6 curves
d4	d3	-0.51	-0.74	-0.06	-0.18	0.37	-0.14	-0.11
d5	d3	0.17	0.49	-0.02	-0.02	0.18	-0.07	-0.12
M1	d3	0.10	-0.29	-0.13	-0.05	0.09	-0.14	-0.20
M2	d3	0.83	0.28	-0.39	-0.27	0.63	0.44	-0.19
M3	d3	0.33	-0.14	-0.17	0.17	0.61	0.11	-0.15
M4	d3	0.31	-0.22	-0.29	-0.08	-0.08	-0.16	-0.16
σ1	d3	-0.10	-0.13	0.34	0.11	0.11	0.14	0.12
σ2	d3	-0.26	-0.16	0.00	-0.24	-0.05	-0.06	0.00
σ3	d3	-0.60	-0.60	0.04	-0.85	-0.46	-0.68	-0.18
σ4	d3	-0.87	-0.61	0.00	-0.63	-0.71	-0.48	0.03
σ5	d3	0.01	0.12	0.18	0.18	0.36	0.16	0.08
σ6	d3	0.03	-0.38	-0.28	0.07	-0.02	-0.19	-0.11
d5	d4	-0.44	-0.43	0.12	-0.85	0.23	-0.43	-0.20
M1	d4	0.24	0.53	0.73	-0.26	0.13	-0.02	0.34
M2	d4	-0.35	-0.24	0.28	0.02	0.61	-0.05	0.24
M3	d4	-0.11	0.25	0.51	-0.25	0.53	-0.14	0.09
M4	d4	0.01	0.31	0.35	-0.63	-0.53	-0.78	-0.28
σ1	d4	0.09	0.22	-0.08	0.06	0.15	-0.02	-0.06
σ2	d4	0.23	0.00	-0.09	0.19	-0.28	0.08	0.02
σ3	d4	0.43	0.71	0.16	0.29	-0.16	0.13	0.26
σ4	d4	0.47	0.39	0.17	0.13	-0.63	-0.09	0.30
σ5	d4	0.04	-0.14	0.06	0.29	0.67	0.76	0.32
σ6	d4	0.13	0.34	0.20	-0.40	-0.45	-0.78	-0.30
M1	d5	0.09	-0.46	0.42	0.35	0.11	0.41	0.38
M2	d5	-0.04	-0.13	0.27	0.19	0.16	0.27	0.33
M3	d5	0.23	0.01	0.57	0.36	0.44	0.68	0.58
M4	d5	0.13	-0.28	0.22	0.66	0.06	0.64	0.28
σ1	d5	-0.05	-0.10	-0.02	-0.11	0.00	-0.11	-0.05
σ2	d5	-0.08	-0.13	0.01	-0.17	-0.11	0.18	-0.01

Table B1 (Continued)

Parameter a_i	a_j	5.8 keV	6.1 keV	6.94 keV	7.16 keV	7.3 keV	8.0 keV	all 6 curves
σ3	d5	0.10	-0.26	-0.18	-0.06	0.22	0.18	0.05
σ4	d5	-0.01	-0.30	-0.16	-0.01	-0.30	-0.06	-0.01
σ5	d5	0.10	0.25	0.09	-0.15	0.06	-0.58	-0.09
σ6	d5	-0.13	-0.38	0.24	0.42	-0.15	0.55	0.17
M2	M1	-0.01	-0.20	0.68	0.69	0.56	0.65	0.88
M3	M1	0.54	0.47	0.72	0.64	0.31	0.53	0.60
M4	M1	0.46	0.41	0.61	0.21	0.08	0.37	0.36
σ1	M1	0.03	0.04	-0.04	-0.22	-0.06	-0.30	-0.08
σ2	M1	0.35	0.36	-0.04	-0.28	-0.10	0.56	0.05
σ3	M1	0.36	0.40	-0.16	-0.09	0.06	0.09	0.21
σ4	M1	0.20	0.56	-0.13	0.04	0.25	0.37	0.13
σ5	M1	0.07	-0.31	-0.25	0.09	0.03	-0.37	-0.12
σ6	M1	0.06	0.38	0.50	0.07	-0.13	0.19	0.17
M3	M2	0.37	0.19	0.64	0.40	0.67	0.54	0.61
M4	M2	0.45	0.35	0.71	0.22	-0.13	0.24	0.42
σ1	M2	-0.12	-0.12	-0.03	-0.21	0.08	-0.16	-0.09
σ2	M2	-0.22	-0.02	0.07	-0.09	-0.18	0.43	0.06
σ3	M2	-0.82	-0.54	-0.43	0.38	-0.48	-0.62	0.05
σ4	M2	-0.92	-0.44	-0.42	0.51	-0.42	-0.02	-0.06
σ5	M2	-0.19	-0.20	-0.47	-0.09	0.39	-0.20	-0.12
σ6	M2	0.24	0.15	0.56	0.24	-0.15	0.07	0.19
M4	M3	0.55	0.84	0.74	0.34	0.07	0.41	0.60
σ1	M3	-0.06	-0.11	-0.07	-0.12	0.07	-0.12	-0.10
σ2	M3	0.11	0.36	-0.04	-0.28	-0.19	0.25	0.00
σ3	M3	-0.09	-0.06	-0.24	-0.20	-0.20	-0.01	0.15
σ4	M3	-0.23	0.35	-0.24	-0.20	-0.63	-0.24	0.01
σ5	M3	0.14	-0.57	-0.16	0.25	0.33	-0.26	-0.11
σ6	M3	0.09	0.61	0.59	0.13	-0.07	0.31	0.36
σ1	M4	-0.03	-0.06	-0.08	-0.10	-0.15	-0.12	-0.04

Table B1 (Continued)

Parameter a_i	a_j	5.8 keV	6.1 keV	6.94 keV	7.16 keV	7.3 keV	8.0 keV	all 6 curves
σ2	M4	0.16	0.32	-0.05	-0.08	0.11	0.13	0.01
σ3	M4	-0.23	-0.12	-0.27	0.07	0.17	0.06	-0.08
σ4	M4	-0.26	0.32	-0.27	0.09	0.25	0.22	-0.19
σ5	M4	-0.39	-0.77	-0.66	-0.58	-0.74	-0.95	-0.61
σ6	M4	0.60	0.83	0.85	0.65	0.75	0.94	0.88
σ2	σ1	0.00	-0.42	0.07	0.25	-0.05	-0.30	-0.14
σ3	σ1	0.13	0.22	0.09	-0.08	-0.12	-0.08	0.04
σ4	σ1	0.12	0.01	0.02	-0.05	-0.16	-0.23	0.07
σ5	σ1	0.03	-0.05	0.04	0.07	0.16	0.12	0.00
σ6	σ1	0.01	-0.03	-0.07	-0.01	-0.10	-0.06	-0.01
σ3	σ2	0.24	-0.03	0.27	0.25	-0.10	-0.05	0.23
σ4	σ2	0.33	0.52	0.24	0.25	0.16	0.31	0.21
σ5	σ2	-0.09	-0.30	0.14	-0.10	-0.19	-0.16	0.03
σ6	σ2	0.06	0.35	-0.05	-0.06	0.14	0.00	0.03
σ4	σ3	0.77	0.25	0.90	0.63	0.23	0.12	0.31
σ5	σ3	0.38	0.30	0.25	-0.24	-0.20	-0.07	0.20
σ6	σ3	-0.30	-0.02	-0.18	0.01	-0.04	0.13	-0.10
σ5	σ4	0.10	-0.34	0.27	-0.22	-0.51	-0.30	0.26
σ6	σ4	-0.06	0.47	-0.18	0.09	0.17	0.17	-0.16
σ6	σ5	-0.42	-0.68	-0.61	-0.33	-0.40	-0.85	-0.52

REFERENCES

[1] G. B. Stringfellow, Rep. Prog. Phys. 45 (1982) 469

[2] J. G. Wright in *Epitaxial Growth*, Part A (ed. by J. EW. Matthews), Academic Press, New York, (1975)

[3] R. F. Bunshah, Deposition Technologies for Films and Coatings , Noyes, New Jersey, 1982

[4] J. L. Vossen, W. Kern (ed.) Thin Film Process, Academic Press, New York (1978).

[5] J. Musil, J. Vyskocil and S. Kadlec, in *Physics of Thin Films*, 17, (ed. by M. H. Francombe and J. L. Vossen), Academic Press, New York, (1993).

[6] E. E. Fullerton, M. J. Conover, J. E. Mattson, C. H. Sowers, and S. D. Bader, Phys. Rev. B 48, 15755 (1993)

[7] L. H. Bennett, R. E. Watson (ed.), *Magnetic Multilayers*, World Scientific, Singapore,(1994).

[8] T. W. Barbee, in *Proceedings, Topical conference on Low Energy X-ray Diagnostics* (AIP, New York, 1980)

[9] J. P. Henry, E. Spiller, and M. Weisskopf, Proc. Soc. Photo-Opt. Instrum. Eng. 316,166 (1981)

[10] C. D. Mee and E. D. Daniel (ed.), *Magnetic Recording*, (McGraw-Hill Book Company, New York, 1987)

[11] M. N. Baibich, J. M. Broto, A. Fert, F. Nguyen Van Dau, F. Petroff, P. Etienne, B. Greuzet, A.Friederich, and J. Chazelas, Phys. Rev. Lett. 61,2472 (1988)

[12] C. J. Robinson, T. Suzuki, C. M. Falco (ed.) , *Mat. Res. Soc. Symp. Proc.* 150, Mat. Res. Soc., Pittsburgh, 1989.

13 R. L. White, *IEEE trans. Magn.* 28 (1992)

14 J. M. Block, M. Sansone, F. Rondelez, D. G. Peiffer, P. Pincus, M. W. Kim, and P. M. Eisenberger, Phys. Rev. Lett. 54, 1039 (1985)

15 A. Iida, K. Sakurai, A. Yoshinaga and Y. Gohshi, Nucl. Instr. and Meth. A246, 736 (1986)

16 A. Krol, C. J. Sher and Y. H. Kao, Phys. Rev. B, 38, 8579 (1988)

17 D. K. G. de Boer, Phys. Rev. B, 44, 498 (1991)

18 H. Schwenke, R. Gutschke, J. Knoth and M. Kock, Appl. Phys. A, 54, 460 (1992)

19 A. H. Compton, bull, Natl. Res. Counc. (U. S.) 20, 48 (1922)

20 L. G. Parratt, Phys. Rev. 95, 359, (1954)

21 L. Boiso, R. Cortes, A. Defrain, and M. Oumezine, J. Non-Cryst. Solid 61&62, 697 (1984)

22 R. A. Cowley and T. W. Ryan, J. Phys. D 20, 61 (1987)

23 R. Rohlsberger, M. Grote, U. Bergmann, E. Gerdau, R. Hollatz, R. Ruffer, H. D. Ruter, W. Sturhahn, *SPIE* Vol. 1160 X-ray/EUV Optics for Astronomy and Microscopy (1989)

24 T. C. Huang, J. P. Nozieres, V. S. Speriosu, H. Lefakis, and B. A. Gurney, Appl. Phys. Lett. 60 (13), 30 (1992)

25 I. M. Tidswell, B. M. Ocko, P. S. Pershan, S. R. Wasserman and G. M. Whitesides and J. D. Axe, Phys. Rev. B, 41, 1111 (1990)

26 Z. H. Ming, A. Krol, Y. L. Soo, Y. H. Kap, J. S. Park, and K. L. Wang, Phys. Rev. B, 47, 16373 (1993)

27 Zhong-hou Cai, Kegang Huang, P. A. Montano, T. P. Russel, J. M. Bai, G. W. Zajac, J. Chem. Phys. 98 (3), 2376 (1993)

[28] D. Bahr, W. Press, R. Jebasinski and S. Mantl, Phys., Rev. B, 47, 4385 (1993)

[29] J. S. Pederson (J. Appl. Cryst. 25, 129-145 , 1992) has suggested A formalism in attempt to solve the inverse problem by using a Fourier transform of the reflectivity data to obtain the autocorrelation function, or Patterson function, of the density profile, and a square-root deconvolution procedure to get the density. However, This method is limited by the general applicability of the kinematical theory (Born Approximation).

[30] D. S. Sivia, W. A. Hamilton, G. S. Smith, T. P. Rieker, and R. Pynn, J. Appl. Phys. 70 (2), (1991)

[31] J. C. Phillips and K. O. Hodgson, in *Synchrotron Radiation Research*, ed. by H. Winick ands S. Doniach, Plenum Press, New York, 1980.

[32] A good account of the fundamentals of atomic scattering factor can be found in: R. W. James, *The Optical Principals of the Diffraction of X-rays*, Chap. 8, cornell University Press , ithaca, New York (1948) or J. C. Phillips and K. O. Hodgson, *Single_Crystal X-ray Diffraction and Anomalous Scattering Using Synchrotron Radiation* in *Synchrotron Radiation Research* (Ed. by H. Winick and S. Doniach), Chap. 17, Plenum Press, New York (1980)

[33] D. T. Cromer and D. A. Liberman, Acta Crystallogr., A37, 267-268, (1981)

[34] The programm is provided by Peter Lee of Materials Science Division, Argonne National Lab.. Satoshi Sasaki published a numerical table of anomalous scattering factors for atoms Li through Bi, plus U, based on the same method. (KEK Report 88-44, 1989)

[35] J. C. Phillips, L. K. Templeton, and K. O. Hodgson, Science 201, 257-259 (1978)

[36] J. D. Jackson, *Classical Electrodynamics*, 2nd ed., John Wiley & Sons, Inc., New York, 284, (1975)

[37] See, e. g. L. V. Azaroff, *Elements of X-ray Crystallography*, McCRAW-Hill Book Company, New York, P. 166 (1968)

[38] B. Vidal and P. Vincent, Applied Optics, 23,1794 (1984)

[39] P. S. Pershan and J. Als-Nielsen, Phys. Rev. Lett., 52, 759 (1984)

[40] I. W. Hamley and J. S. Pedersen, J. Appl. Cryst., 27, 29-35 (1994)

[41] B. W. Batterman and H. Cole, Reviews of Modern Physics, 36, 681-717 (1964)

[42] J. H. Underwood and T. W. Barbee, Jr., Applied Optics, 20, 3027 (1981)

[43] A. Braslau, P. S. Pershan, G. Swislow, B. M. Ocko, J. Als-Nielsen, Phys. Rev. A, 38, 2457 (1988)

[44] N. Singh, M. Tirrell and F. S. Bates, J. Appl. Cryst., 26, 650-659 (1993)

[45] I. W. Hamley and J. S. Pedersen, J. Appl. Cryst., 27, 29-35 (1994)

[46] L. Nevol, P. Croce, Rev. Phys. Appl. 15, 761 (1980)

[47] Participating Institutions of X6B: Argonne national Laboratory, Brooklyn College of CUNY, Northwestern University, Temple University, BP America and Eastman Kodak Corporation.

[48] Herman Winick and S. Doniach, *Synchrotron Radiation Research*, Plenum Press, New York, P. 1, (1980)

[49] Same as above, p. 15. Some authors, including Jackson (cf. ref. 35, p.675) define it to be half of that given by (3.1).

[50] Susan White-DePace et al. (ed.) *NSLS Experimenter's Handbook* , Brookhaven National Laboratory (1988)

[51] Ref. 47, P. 11

52 I. H. Munro and A. Sabersky, in *Synchrotron Radiation Research*, H. Winick and S. Doniach (Eds.), Plenum, New York, p. 323 (1980)

53 K. G. Huang, M. Ramanathan and P. A. Montano, Rev. Sci. Instrum. 66 (2), 1688 (1995)

54 Mohan Ramanathan and Pedro A. Montano, Rev. Sci. Instrum. 66(2), 1754 (1995)

55 Developed by M. Engbretson, MSD, ANL, Argonne, IL 60439.

56 Developed by G. Swislow, Certified Scientific Software, P.O.Box 3245, Church Street Station, New York, NY 10008

57 Jacob Fraden, *AIP Handbook of Modern Sensors*, AIP, New York, p.474 (1993)

58 G. S. Brown and S. Doniach, in *Synchrotron Radiation Research*, H. Winick and S. Doniach (Eds.), Plenum, New York, 1980, p. 353.

59 A. Gibaud, G. Vignaud and S. K.Sinha, Acta Cryst., A49, 642-648, (1993)

60 The content of this chapter has been published on Zeitschrift Für Physik B 97, 465-472 (1995) by J. Bai, M. Tomkiewicz and P.A. Montano.

61 S. Iwasaki, IEEE trans. Magn. 16, 71 (1980)

62M. Cohen, in: Passivity of metals. R. P. Frankental, J. Kruger (Eds.), P. 521. The Electrochemical Society, Princeton, NJ (1978)

63J. Kruger, in: Proceeding of the 9th International Congress on Metallic Corrosion, vol.1,p. 79. National counsil of Canada. ottawa, ontario, canada (1984)

64 N. Cabrera, N. F. Mott, Rep. Prog. Phys. 12, 163 (1948)

65 N. Sato, K. Kudo, Electrochem. Acta. 19, 461 (1974)

66 J. L. Ord, J. C. Clayton, D. J. DeSmet, J. Electrochem. Soc, 124, 1714 (1977)

67 N. Sato, M. Cohen, J. Electrochem. Soc. 111, 512 (1964); N. Sato, M. Cohen, M. ibid, 519 (1964)

68 G. Economy, R. Speiser, F. H. Beck, M. G. Fontana, Electrochem. Soc. 108, 337 (1961)

69 G. Dagan, M. Tomkiewicz, J. Electrochem. Soc. 139, 461-6 (1992)

70 P. Marcus, I. Olefjord, corrosion-Nace 42, 91 (1986)

71 W.Y. Lee, G. Scherer, C. R. Guarnieri, J. electrochem. Soc. 126, 1533 (1979)

72 J.H. Underwood, T.W. Barbee, AIP conf. Proc. 75, AIP, New York, p.170 (1981)

73 P. A. Montano and G. P. Felcher, Private communication.

74 The content of this chapter has been published on Physica B, 221, 411-415 (1996) by J. Bai, E.E. Fullerton and P.A. Montano.

75 P. Grunberg, R. Schreiber, Y. Peng, M. B. Brodsky, and C. H. Sowers, Phys. Rev. Lett. 57,2442 (1986)

76 M. N. Baibich, J. M. Broto, A. Fert, F. Nguyen Van Dau, F. Petroff, P. Etienne, B.greuzet, a. Friederrich, and J. Chazelas, Phys. Rev. Lett. 61, 2472 (1988)

77 S. S. P. Parkin, N. More, and K. P. Roche, Phys. Rev. Lett. 64, 2304 (1990)

78 J. Unguris, R. J. Celotta, and D. T. Pierce, Phys. Rev. Lett. 67, 140 (1991)

79 Y. Yafet in *Magnetic Multilayers* (ed. by L. H. Bennet and R. E. Watson) World Scientific, P. 19 (1994)

[80] M. D. Stiles, Phys. Rev. B48, 7238 (1993)

[81] Martha Pardavi-Horvath in *Magnetic Multilayers* (ed. by L. H. Bennet and R. E. Watson) World Scientific, P. 355 (1994)

[82] R. E. Camley and J. Barnas, Phys. Rev. Lett. 63,664 (1989)

[83] Y. Wang, P. M. Levy, and J. L. Fry, Phys. Rev. Lett. 65, 2732 (1990)

[84] D. T. Pierce, J. A. Stroscio, J. Unguris, and R. J. Celotta, Phys. Rev. B 49, 14564 (1994)

[85] E. E. Fullerton, D. M. Kelly, J. Guimpel. I. Schuller and Y. bruynseraede, Phys. Rev. lett., 68, 859 (1992)

[86] H. Kanai and R. L. white, Digests INTERMAG 93, Stockholm, paper DB-08 (1993)

[87] A. Kamijo and H. Igarashi, J. Appl. Phys. 75 (5), 2455 (1992)

[88] W. Hahn , M. Loewenhaupt, G. P. Felcher, Y. Y. Huang and S. S. P. Parkin, J. Appl. Phys. 75 (7), 3564 (1994)

[89] D. L. Williamson, B. M. Lairson, A. P. Payne, N. M. Rensing and B. M. Clemens, Hyperfine Interactions, 92 , 1271 (1994)

[90] S. S. P. Parkin, B. R. York, Appl. Phys. Lett. 62, 1842 (1993)

[91] Samples were prepared by Eric. E. Fullerton. The procedure has been discussed in a paper by J. Bai, Eric Fullerton and Pedro A. Montano, to appear in Physica B (1996)

[92] Boon K. Teo, *EXAFS: Basic Principles and Data Analysis*, Springer-Verlag, New York, P. 26 (1986)

[93] I.J. Pickering, G.N. George, J.T. Lewandowski and A.J. Jacobson, J. Am. Chem. Soc. 115,4137-4144 (1993)

94 K.I. Pandya, R.W. Hoffman, J. McBreen and W.E. O'Grady, J. Electrochem. Soc., vol.137, 383-388 (1990)

95 W. H. Press et al. Numerical Recipes in FORTRAN, P. 650, Cambridge University Press (1992)